MULTICOMPONENT DISTRIBUTED ACOUSTIC SENSING: CONCEPT, THEORY, AND APPLICATIONS

by

Ivan Lim Chen Ning

© Copyright by Ivan Lim Chen Ning, 2019

All Rights Reserved

A thesis submitted to the Faculty and the Board of Trustees of the Colorado School of Mines in partial fulfillment of the requirements for the degree of Doctor of Philosophy (Geophysics).

Golden, Colorado

Date _____

Signed: _____
Ivan Lim Chen Ning

Signed: _____
Dr. Paul C. Sava
Thesis Advisor

Golden, Colorado

Date _____

Signed: _____
Dr. John H. Bradford
Professor and Head
Department of Geophysics

ABSTRACT

Conventionally, ground motion due to seismic waves is monitored using seismometers either as single point measurements or as arrays. Such acquisition systems are used both in exploration seismology and in seismic monitoring. In recent years, the use of optical fiber sensing has been steadily on the rise especially in the borehole environment for information, including, but not limited to, temperature, pressure, and strain. Optical fibers are enticing because of their dense spatial sampling and their low operation cost, given that the optical fiber is readily available at the time boreholes are constructed. In exploration seismology, distributed acoustic sensing (DAS) provides the means to record seismic strain projections along the optical fiber. Although this empowers us to perform dense spatial sampling measurements along the optical fiber, the single component data are a poor approximation to the total strain tensor. In my thesis, I propose solutions to obtain the full strain tensor at any location along the purposefully designed optical fiber through geometrical concepts and inversion theory. I also present a mechanism to recover multicomponent DAS data using only a single optical fiber in an averaging sense suitable for long wavelength applications.

The ability to obtain multicomponent DAS data paves the way to better representation of the elastic wavefield leading to better tomography, imaging, and ultimately reservoir characterization. Given the capacity to record multicomponent DAS data, I introduce an imaging method for seismic source mechanism that takes advantage of conventional displacement vector and the novel strain tensor measurements. The technique makes it possible to estimate source parameters in near real-time with approximate subsurface models that adequately describe the direct P- and S-waves kinematics. According to wave propagation theory, accurate seismic wavefield extrapolation requires both the seismic stress tensor and displacement data. Typical practice using only displacement data introduces nonphysical wave modes during wavefield extrapolation resulting in elastic seismic images contaminated by artifacts.

The availability of multicomponent strain data makes stress observations possible given that the material properties in the vicinity of the recording array are known to facilitate accurate wavefield reconstruction based on multicomponent DAS data. I demonstrate accurate elastic seismic wavefield extrapolation, leading to seismic image improvements that better represent the subsurface. Using the same general wavefield reconstruction theory, I also propose to accurately reconstruct wavefields from a single layer boundary on the computation domain to reduce memory and computational requirements for seismic applications that require wavefield storage, especially for large-scale 3D experiments.

I validate all proposed techniques with realistic numerical experiments using models with arbitrary anisotropy and heterogeneity. I test my methods using field datasets such as a DAS vertical seismic profile (VSP) data from the Eagle Ford shale formation. The thought-provoking development of multicomponent DAS acquisition, which is not possible with currently available technology, has the potential to revolutionize imaging and inversion using elastic wavefields. The work in this thesis can inspire new applications outside of seismic exploration challenges, including, but not limited to structural health monitoring and seismological investigation at global or regional scales.

TABLE OF CONTENTS

ABSTRACT iii

LIST OF FIGURES AND TABLES viii

LIST OF ABBREVIATIONS xiv

ACKNOWLEDGMENTS xv

DEDICATION xvii

CHAPTER 1 INTRODUCTION 1

CHAPTER 2 MULTICOMPONENT DISTRIBUTED ACOUSTIC SENSING: CONCEPT AND THEORY 8

2.1 Introduction 9

2.2 Theory 11

2.3 Numerical examples 19

2.4 Discussion 23

2.5 Conclusions 27

2.6 Acknowledgments 27

CHAPTER 3 HIGH-RESOLUTION MULTICOMPONENT DISTRIBUTED ACOUSTIC SENSING 29

3.1 Introduction 30

3.2 Theory 32

3.3 Numerical examples 41

3.4 Discussion 45

3.5 Conclusions 48

3.6 Acknowledgments 48
3.7 Appendix 49
3.7.1 Strain Projection 49
CHAPTER 4 SEISMIC SOURCE MECHANISM IMAGING 51
4.1 Introduction 51
4.2 Theory 53
4.3 Numerical examples 57
4.4 Discussion 62
4.5 Conclusions 66
4.6 Acknowledgments 67
CHAPTER 5 OPTIMAL ELASTIC SOURCE WAVEFIELD RECONSTRUCTION . 68
5.1 Introduction 69
5.2 Theory 71
5.3 Source reconstruction example 74
5.4 RTM example 75
5.5 Marmousi II example 81
5.6 Eagle Ford Shale example 84
5.7 Discussion 93
5.8 Conclusions 96
5.9 Acknowledgments 96
5.10 Appendix 96
5.10.1 Energy norm modeling and migration operators 97
5.10.2 Linearized elastic wave modeling operator 98

CHAPTER 6 CONCLUSIONS 101

6.1 Limitations and opportunities 103

REFERENCES CITED 108

APPENDIX PERMISSIONS FOR CHAPTERS 118

A.1 Permission from publisher 118

A.2 Permission for field datasets 120

LIST OF FIGURES AND TABLES

Figure 2.2 Examples of optical fiber configurations with (a) two helical optical fiber with pitch angle of 20° and 60° and a single straight optical fiber, (b) one helical optical fiber with pitch angle of 20° and a single straight optical fiber. (c) A simplified example of the chirping helix configuration for plotting purposes. The helixes are constructed with a diameter of 0.0244 m (about 1 in). (d), (e), and (f) are the singular value decomposition (SVD) of the Gram matrix in equation 3.4 for the corresponding configurations. The Gram matrix uses measurements in a window of 5 m. 16

Figure 2.3 Condition number of the Gram matrix using a fixed diameter at 0.0244 m (about 1 in) with the dual optical fibers configuration at gauge lengths of (a) 0.2 m and (b) 1.0 m for window from 3 to 7 m and pitch angle from 10° to 30°. Similarly, the condition number with the chirping helical optical fiber configuration at gauge lengths of (c) 0.2 m and (d) 1.0 m for window from 3 to 7 m and number of turns within a window from 10 to 210 turns. 18

Figure 2.4 (a) Schematic representation of a DAS experiment depicting the source (dot) and receiver (line) locations. (b) The ideal strain tensor that we would like to reconstruct from DAS measurements. (c) The P-wave velocity model containing a low velocity Gaussian anomaly designed to produce wavefield triplications. The S-wave velocity is half of the P-wave velocity. (d) A snapshot of the vertical displacement wavefield. . . 21

Figure 2.5 Strain tensor reconstructed using the dual optical fibers configuration with one helical and one straight optical fiber shown in Figure 2.2(b) using a gauge length and channel spacing of (a) 0.2 m and (c) 1.0 m. (b) and (d) are the difference between the ideal strain tensor in Figure 2.4(b) and the respective reconstructed tensor in (a) and (c) magnified 10 times. 22

Figure 2.6 Strain tensor reconstructed from data containing random noise with 5% of the maximum data amplitude and band-limited to the data band using the dual optical fibers configuration with one helical optical fiber and one straight optical fiber shown in Figure 2.2(b) using a gauge length and channel spacing of (a) 0.2 m and (c) 1.0 m. (b) and (d) are the difference between the ideal strain tensor in Figure 2.4(b) and the respective reconstructed tensor in (a) and (c). 24

Figure 2.7 Strain tensor reconstructed using the chirping helical optical fiber configuration using a gauge length and channel spacing of 0.2 m is shown in panel (a) and panel (c) shows the reconstruction under the influence of random noise with 5% of the maximum data amplitude and band-limited to the data band. The difference between the ideal strain tensor in Figure 2.4(b) and the respective reconstructed tensor in (a) and (c) are shown in panels (b) magnified 10 times and (d). 25

Figure 3.1 Optical fiber geometry with (a) six equally spaced vectors of six pitch angles (20°, 30°, 40°, 50°, 60°, and 70°), and (b) five equally spaced vectors of pitch angle of 20° with a straight vector in the middle. Panels (c) and (d) depict tetrahedra and right pentagonal pyramid respectively using the corresponding vectors in (a) and (b) sharing the same origin. The plots in (e) and (f) show singular values of the respective Gram matrices. 36

Figure 3.4 Two-pentagonal pyramid using five vectors with pitch angles of (a) **5°**, (b) **20°**, and (c) **50°**. The three pyramids show the visual relationship between the enclosed surface area and volume. 39

Figure 3.6 (a) The plot shows a 1D parameter scan for the intersection between diameter of 2.44 cm (about 1 inch) and 20° pitch angle of Figure 3.5. The stars mark the condition number for gauge lengths of 0.1, 0.5, and 1.0 m. (b) The plot shows diameter parameter scan by the fixing pitch angle at 20° and the gauge length at 0.1 m. The star marks the location at diameter of 2.44 cm (about 1 inch). The star with circle indicates the same combinations of parameters for both panels. 42

Figure 3.7 (a) Schematic representation of a DAS experiment depicting the source (dot) and receiver (line) locations. (b) The ideal strain tensor that we would like to reconstruct from DAS measurements. (c) The P-wave velocity model containing a low velocity Gaussian anomaly designed to produce wavefield triplications. The S-wave velocity is half of the P-wave velocity. (d) A snapshot of the vertical displacement wavefield. . . 44

Figure 3.8 Strain tensor reconstructed with five equally spaced helical optical fibers and a straight optical fiber using a gauge length of (a) 0.1 m, (c) 0.5 m, and (e)1.0 m. (b), (d), and (f) are the difference between the ideal strain tensor in Figure 3.7(b) and the respective reconstructed tensor in (a), (c), and (e) magnified 10 times. 46

Figure 3.9 Strain tensor reconstructed from data containing random noise with 30% of the maximum data amplitude and band-limited to the data band with five equally spaced helical optical fibers and a straight optical fiber using a gauge length of (a) 0.1 m, (c) 0.5 m, and (e) 1.0 m. (b), (d), and (f) are the difference between the ideal strain tensor in Figure 3.7(b) and the respective reconstructed tensor in (a), (c) and (e). . . 47

Figure 4.1 3D microseismic experiment setup with receivers providing (a) ideal spherical coverage and (b) surface seismic acquisition. The red dot represents the source location. 59

Figure 5.1 Schematic diagram to illustrate the elements of the representation theorem. The black circle denotes the surface $\partial\Omega$ enclosing a volume Ω with the corresponding normal vector $\mathbf{n}$ pointing outwards. The red circles denote the locations of sources/receivers. 72

Figure 5.2 An example for computational (in white) and boundary domain (in green) set up. (a) Our method to reconstruct the source wavefield only require storage at a single boundary layer (black dots). (b) Conventional methods require storage at half the finite-difference stencil either in the computational (in gray) or in the boundary (in blue) domain. Our method in (a) shows significant reduction for storage requirement compared to conventional methods in (b). 73

Figure 5.3 (a) The P-wave velocity model with an overlay of a 2D experiment depicting the source (white dots) and receiver (black line) locations. (b) The corresponding smooth P-wave velocity for reverse time migration. . . 76

Figure 5.4 Snapshots of the reference source wavefield for time-step at (a) 200, (b) 300, and (c) 400. In all panels, the vertical axes represent depth, whereas the horizontal axes denote horizontal position. The panels consist of the stress $(\mathrm{t}_{xx}, \mathrm{t}_{zz}, \mathrm{t}_{xz})$ tensor and particle displacement $(\mathrm{u}_x, \mathrm{u}_z)$ vector field in the tensor-vector matrix layout. 77

Figure 5.5 Snapshots of the reconstructed source wavefield from a single boundary layer for time-step at (a) 200, (b) 300, and (c) 400. In all panels, the vertical axes represent depth, whereas the horizontal axes denote horizontal position. The panels consist of the stress $(\mathrm{t}_{xx}, \mathrm{t}_{zz}, \mathrm{t}_{xz})$ tensor and particle displacement $(\mathrm{u}_x, \mathrm{u}_z)$ vector field in the tensor-vector matrix layout. 78

Figure 5.6 Snapshots of the difference between the forward source wavefield (Figure 5.4) extrapolation and the reconstructed source wavefield (Figure 5.5) from the single boundary layer for time-step at (a) 200, (b) 300, and (c) 400. In all the panels, the vertical axes represent depth whereas the horizontal axes denote horizontal position. 79

Figure 5.7 Graph along depth $z = 0.025$ km for the reference source wavefield (in blue) and the reconstructed source wavefield (in red) at time-steps of (a) 200, (b) 300, and (c) 400. The vertical axis of the individual panels represents the amplitude whereas the horizontal axis denotes the horizontal position. The panels consist of the stress $(\mathrm{t}_{xx}, \mathrm{t}_{zz}, \mathrm{t}_{xz})$ tensor and particle displacement $(\mathrm{u}_x, \mathrm{u}_z)$ vector field in the tensor-vector matrix layout. 80

Figure 5.8 Single shot energy norm elastic reverse time migration using (a) forward source wavefield extrapolation and (b) reconstructed source wavefield. (c) The corresponding difference plot between (a) and (b). The graphs at the bottom of (a), (b), and (c) denote amplitude profile along the horizontal direction (horizontal dotted line) at the reflection depth while the graphs on the right show the amplitude profile along the depth direction (vertical dotted line) at the shot location. The blue amplitude profile corresponds to (a), red from (b), and black from (c). . . 82

Figure 5.9 Energy norm elastic reverse time migration from all the available shots using (a) forward source wavefield extrapolation and (b) reconstructed source wavefield. (c) The corresponding difference plot between (a) and (b). The graphs at the bottom of (a), (b), and (c) denotes amplitude profile along the x-axis (horizontal dotted line) at the reflection depth while the graphs on the right show the amplitude profile along the z-axis (vertical dotted line) at the shot location. The blue amplitude profile corresponds to (a), red from (b), and black from (c). 83

Figure 5.10 Vertical transverse isotropic Marmousi II model with the vertical (a) P ($\mathrm{V_{P0}}$) and (b) S ($\mathrm{V_{S0}}$) velocities. The dimensionless anisotropic Thomsen parameters (c) ε and (d) δ are derived from (e) the density model. The overlay white dots and red line in (e) depict the source and receiver locations, respectively. 85

Figure 5.11 A wavefield snapshot in the anisotropic elastic Marmousi II model shown in Figure 5.10 for the (a) reference and (b) reconstructed source wavefields. (c) The corresponding difference between (a) and (b). The vertical and horizontal axes of the panels represent depth and horizontal position. The panels consist of the stress $(\mathrm{t}_{xx}, \mathrm{t}_{zz}, \mathrm{t}_{xz})$ tensor and particle displacement $(\mathrm{u}_x, \mathrm{u}_z)$ vector in the tensor-vector matrix layout. . 86

Figure 5.12 Energy norm elastic reverse time migration for the anisotropic Marmousi II model in Figure 5.10 using the reconstructed source wavefields for (a) a single shot and (b) all 17 shots. 87

Figure 5.13 Panel (a) shows the P-wave velocity obtained through first-break picking, while panel (b) shows the S-wave velocity obtained from the well logs. Both panels show the acquisition geometry with the receivers in black and sources in white. 88

Figure 5.14 Single shot reverse time migration (RTM) image using (a) reference and (b) reconstructed source wavefield. (c) The difference between (a) and (b). (d)-(e) The equivalent images of (a)-(c) after dip filtering. 90

Figure 5.15 Single shot least-squares reverse time migration (LSRTM) image using (a) reference and (b) reconstructed source wavefield. (c) The difference between (a) and (b). (d)-(e) The equivalent images of (a)-(c) after dip filtering. 91

Figure 5.16 Initial data residuals for single shot least-squares reverse time migration (LSRTM) image using (a) reference and (b) reconstructed source wavefield. The final data residuals for the corresponding methods in (c) and (d). The least-squares solution modeled DAS response using (e) reference and (f) reconstructed source wavefield. 92

Figure 5.17 All 16 shots reverse time migration (RTM) image using (a) reference and (b) reconstructed source wavefield. (c) The difference between (a) and (b). (d)-(e) The equivalent images of (a)-(c) after dip filtering and poststack amplitude gain with one power of depth. 94

Figure 5.18 All 16 shots least-squares reverse time migration (LSRTM) image using (a) reference and (b) reconstructed source wavefield. (c) The difference between (a) and (b). (d)-(e) The equivalent images of (a)-(c) after dip filtering and poststack amplitude gain with one power of depth. 95

Figure 6.1 (a) The top panel shows a helical optical fiber wrapped along a straight axis, where the bottom panel shows the wrapping angle as a function of the axial distance. (b) The analogous figure for a helical optical fiber wrapped along a curved axis. 105

Figure 6.2 The Southern California model for the (a) P- and (b) S-wave velocities, and the (c) density from the CVM-S4.26 model . (d) The surface elevation together with white lines representing potential deployment of multicomponent DAS along the interstate and state highway system of Southern California. The 1991 Sierra Madre earthquake location shown in red. 106

Figure 6.3 (a) A simulation snapshot of the seismic wavefield due to the 1991 Sierra Madre earthquake. (b) The total strain energy (bright colors denote high intensity) obtained using multicomponent DAS overlaid on the Southern California map (U.S. Geological Survey, National Geospatial Program). 107

Table 4.1 Summary of all the 3D source mechanism experiment. 58

Table 4.2 xz-plane double-couple source mechanism and image symmetry comparison. 60

LIST OF ABBREVIATIONS

Coherent Optical Time-Domain Reflectometry . . . . . COTDR

Distributed Acoustic Sensing . . . . . DAS

Distributed Temperature Sensing . . . . . DTS

Full Waveform Inversion . . . . . FWI

Input/Output . . . . . I/O

Interrogator Unit . . . . . IU

Least-Squares Reverse Time Migration . . . . . LSRTM

Point Spread Function . . . . . PSF

Residual Sum of Squares . . . . . RSS

Reverse Time Migration . . . . . RTM

Surface-Area-to-Volume ratio . . . . . SA:V

Signal-to-Noise Ratio . . . . . SNR

Singular Value Decomposition . . . . . SVD

Southern California . . . . . SoCal

Southern California Earthquake Center . . . . . SCEC

Unified Community Velocity Model . . . . . UCVM

Vertical Seismic Profile . . . . . VSP

Vertically Transverse Isotropy . . . . . VTI

ACKNOWLEDGMENTS

Approximately four years ago, I took the decision onto myself to leave my job at went back to school again. The irony after I've told myself that I would never do a Ph.D. after I've completed my masters. It was never an easy decision to make and a somewhat selfish one admittedly because decisions like this are never about myself. However, through this experience at Mines, I have not only expanded my knowledge, but I have also grown as an individual. I am forever in debt to all that has been a part of this memorable journey.

I want to express my multitudinous gratitude to Dr. Paul Sava for his boundless patience in helping me to develop as an individual and as a researcher. He helped kick-start my research odyssey on the most significant challenge in DAS and having my back during a watershed moment in my first-ever attempt on peer-reviewed publishing. Learning from him is like his Hawaiian shirt day (either snow or rain or shine) as I learn about extraterrestrial seismology. I would like to thank the times when he said "you are welcome" as I enter his office for he gracefully volunteered me for opportunities which I have learned a considerable amount.

My great DAS odyssey won't be complete without Dr. Martin Karrenbach, who has helped me to understand and better my research. I am incredibly grateful to my fellow committee members, Dr. Roel Snieder, Dr. Whitney Trainor-Guitton, Dr. Michael Wakin, and Dr. Mahadevan Ganesh who I have learned a great deal with through discussion and classes. I thank Dr. Jim Simmons for the enormous amount of lunch conversations we had and also initiating the intradepartmental collaboration, which provided me the opportunity to express my work on field applications. My heartfelt thanks to Diane Witters for helping me to be a better writer and ever so warm welcoming gatherings. Thank you, Dr. Ken Larner, for I have learned from you to be a better presenter. I also want to thank Dr. Helmut Jakubowicz for without his initial encouragement, I would have never embarked on

my geophysical adventure.

I would also like to thank the administrative support from Pamela Ehrlich Kraus, Shingo Ishida, Dawn Umpleby, Joana E. Perez, Gina Schwieger, Michelle Szobody, Debra Marrufo, and Emilia Clayton. I can say with certainty that it would be impossible to concentrate on research without their continuous assistance. I am honored to share great memories with fellow friends whom I am fortunate to overlap with Hui Wang, (uncle) Nishant Kamath, Yuting Duan, Esteban Díaz, Xun Li, Samir Jreij, Lucas Andrade, Daniel Rocha Jr, Alicia Arias, Tong Bai, Oscar Jarillo Michel, Odette Aragão, Tuğrul Konuk, Ufuk Durmuş, Azar Hasanov, Samuel Courville, Thomas Rapstine, Colton Kohnke, Iga Pawalec, Hayden Powers, Zhuo Liu, Qifan Liu, Youfang Liu, Whitney Schultz, and Adam Tuppen. Special thanks are given to fellow B-team members for provoking Friday midnight debates on Geophysics and life in general.

In my heart of hearts, I want to thank my family for supporting my decision, for being a tower of strength in my life, and for making my absence felt close. To my fiancée, Monika, thank you for making my Ph.D. journey a tad less consuming and for understanding without speech for all that glitters isn't gold.

"I can no other answer make, but, thanks, and thanks."

— William Shakespeare

To my late great-grandfather, for he who never give up on me.

"You'll never find a rainbow *if you're looking down."*

— Charlie Chaplin

CHAPTER 1

INTRODUCTION

Advancements in seismic acquisition have been catalysts for developments of new seismic techniques. In exploration geophysics, we recover higher quality representations of the subsurface by acquiring data of higher spatial dimension, i.e., from 2D to 3D. When we gather multiple vintages of 3D data, we begin to understand the subsurface structure and its evolution over time. Although seismic techniques can effortlessly detect subsurface features, the seismic resolution dictates their ability to differentiate between small scale features. The higher the resolution, the better the distinguishability of the seismic features for an accurate representation of the subsurface.

In the marine setting, the seismic image resolution is often limited by the reflections due to the sea surface, known as ghosts, which arise both on the source and the receiver side of the submerged acquisition hardware. These ghost reflections may interfere constructively or destructively with subsurface reflection data, i.e., the signal of interest. Such interference not only increases the difficulty to process and interpret the data but also introduces data frequency notches, thus limiting their usable frequency range. One possibility to overcome the marine seismic resolution problem is to improve the acquisition design, such as by deploying dual-sensor systems to record additional vector data complementing conventional pressure data, by deploying variable-depth receivers, or by deploying multiple streamers at different constant-depths (Carlson et al., 2007; Moldoveanu et al., 2007; Soubaras and Dowle, 2010; Soubaras and Lafet, 2013). The successful implementation of better acquisition becomes instrumental to new technologies for wavefield separation and interpolation (Robertsson et al., 2008; Özbek et al., 2010; Day et al., 2013; van Borselen et al., 2013).

On land, seismometers used individually or as an array are irreplaceable. Such instruments obtain information to characterize and monitor in detail the complex subsurface

structures. Various technological developments are based on multicomponent vector measurements by seismometers and more recently, recordings of rotational sensors (Barak et al., 2014; Igel et al., 2015; Schmelzbach et al., 2018; Barak et al., 2018). The rotational and strain tensor measurements allow us to obtain information about the wavefield gradients for applications like full elastic wavefield decomposition and accurate elastic wavefield extrapolation following the representation theorem (Aki and Richards, 2002; Wapenaar, 2014). Although rotation sensors are available, despite their limited portability, the full strain tensor is not an easily accessible measurement. To obtain the principal strain components, we calculate the spatial gradients of densely sampled vector measurements recorded at the free surface (Cochard et al., 2006; Langston et al., 2006; Langston, 2007). The vertical derivatives require buried receiver arrays rendering this method impractical for widespread applications. Robertsson and Curtis (2002) show that the vertical derivatives could be approximated using horizontal derivatives at the free surface as stresses vanish vertically in media of isotropic and homogeneous. An alternative to obtaining the full wavefield spatial gradient is to deploy known receiver geometries such as tetrahedra under the assumption of a homogeneous isotropic medium (Robertsson and Muyzert, 1999; Schmelzbach et al., 2016). Furthermore, the simultaneous deployment of multiple receivers to maintain an ideal tetrahedron shape can be arduous and time-consuming.

In light of the limitations of strain data acquisition, my research addresses two main themes in designing seismic acquisition systems and developing applications using such new measurements. I investigate the use of novel, low-cost technology such as distributed acoustic sensing (DAS) which uses optical fiber tightly coupled to the ground as a strain measuring tool. A typical DAS system utilizes an interrogator unit to send laser pulses into an optical fiber while observing back-scattered light caused by impurities (unavoidable manufacturing defects) in the optical fiber. DAS operating on Coherent Optical Time-Domain Reflectometry (COTDR) analyzes the back-scattered signal between pairs of points along the optical fiber, separated by a distance known as gauge length, to obtain the average axial strain

measurement within that particular interval. Conventional DAS configuration requires a gauge length of around 1 m to maintain an acceptable signal-to-noise ratio (SNR) of the measurements. Optical fiber acquisition is a rapidly evolving technology, and recent literature suggests that recordings of satisfactory SNR can be obtained even with 5 cm gauge length using specially-engineered optical fibers (Farhadiroushan et al., 2016).

Despite the increasing efforts of applying DAS for geophysical applications in both surface (Lumens et al., 2013; Hornman, 2017; Dou et al., 2016; Jreij et al., 2017) and borehole environments (Mestayer et al., 2011; Mateeva et al., 2012, 2013; Wu et al., 2015; Zhan et al., 2015; Hornman et al., 2015; Jiang et al., 2016; Chalenski et al., 2016), DAS is limited by the inherent single component measurement i.e., strain measurement along the optical fiber. Multicomponent optical fiber data, i.e., the complete strain tensor, is the missing piece of the puzzle. In **Chapter 2**, I address the essential challenge of DAS measurement by developing the capability to acquire multicomponent DAS data, which is not possible with currently available DAS technology. A conventional DAS system records a single component projection of the surrounding strain tensor along the direction of the optical fiber. In my thesis, I develop the theory and concept for multicomponent acquisition based on multiple strain projections. This can be accomplished with a combination of helical and straight optical fibers or with a single chirping (variable wrapping angle) helical optical fiber to reconstruct the entire strain tensor, a technique which I refer to as *multicomponent optical fiber acquisition*. This method exploits consecutive measurements within a given spatial window which I assume to represent the same strain tensor. The chirping helix enables the reconstruction of the entire strain tensor with the use of only one optical fiber which makes it potentially cheap to deploy. Although this method is promising, it suffers from reduced spatial resolution associated with the underlying assumption of a large spatial reconstruction window. Increasing the window improves the reconstruction SNR, but implies that the seismic wavelength of interest is substantially larger. In support of this theoretical development, I perform numerical simulations using wavefields of arbitrary complexity and demonstrate the feasibility of

reconstructing the entire strain tensor. This work has already been published in the journal *Geophysics* (Lim Chen Ning and Sava, 2018b), and as an expanded abstract at the 2016 Society of Exploration Geophysicists Annual Convention (Lim Chen Ning and Sava, 2016).

The assumption that the seismic wavelength of interest is greater than the window used for reconstruction limits the application of the proposed single fiber method to long seismic wavelengths. This constraint reduces the resolution of the reconstructed strain tensor, thus directly affecting the derived seismic image. In **Chapter 3**, I proposed to use a collection of optical fibers to achieve high-resolution multicomponent optical fiber acquisition and overcome the resolution deficiency. Multiple optical fibers provide a plurality of projections for strain tensor reconstruction thus giving information about the entire tensor. The configuration requires a minimum of six optical fibers to reconstruct all components of the strain tensor. This requirement is similar to the method detailed in **Chapter 2** which involves grouping of at least six successive strain measurements. However, measurements from individual optical fibers remove the need to group consecutive projections and thence achieves high-resolution strain tensor reconstruction. My proposed setup consists of five equally spaced constant pitch angle helical optical fibers and a straight optical fiber to obtain the multiple strain projections that sufficiently describe the surrounding strain tensor. As for the preceding method, I perform numerical simulations using complex elastic seismic wavefields to demonstrate that the proposed configuration not only successfully reconstructs the strain tensor, but also accomplishes this with increased robustness, accuracy, and resolution. This technical advancement has been published in *Geophysical Prospecting* (Lim Chen Ning and Sava, 2018a), and has been presented at the 2017 Society of Exploration Geophysicists Annual Convention (Lim Chen Ning and Sava, 2017).

A potentially simpler alternative to my proposed technique would use measurements taken under special boundary conditions. For example, at the Earth's free surface, we would need to solve for three strain components instead of the six components of the full strain tensor due to vanishing tractions along the direction normal to the surface (Aki and Richards,

2002). This measurement could be done with a tedious deployment of conventional instruments. However, the near-surface instrumentation coupling is challenging even for buried optical fiber (Castongia et al., 2017; Jreij, 2018), although DAS is capable of measuring teleseismic events with a minimal coupling (Lindsey et al., 2017). Coupling problems also persist for common point measuring equipment such as strainmeters (Agnew, 1986). Nonetheless, the solutions I propose for full strain acquisition is applicable for general applications without special deployment considerations or the requirement to exploit the free surface.

In **Chapter 4**, I propose a new imaging formulation that incorporates the conventional displacement measurements and strain tensor data acquired with the technique detailed in the preceding chapters. Starting from the elastic wave equation, I develop an imaging condition generating images that provide information about the source mechanism characterizing the action of external force perturbations. This method leads to seismic images that correspond directly to the respective components of the source mechanism and reveal the source location through the focusing point. Like all wavefield based methods, the knowledge of the subsurface parameters is essential to ensure accurate backward wavefield extrapolation. However, my results show that the process is robust that it only requires a smooth background model which can sufficiently characterize the direct P- and S-waves kinematics. The robustness of this method makes it appropriate for applications such as hydraulic fracturing and can be used to obtain the fracture-related seismic source parameter in near real-time. I validate my approach using multiple 3D numerical examples of different source mechanisms to show our ability to image the source parameters accurately. Although the examples are limited to exploration seismology, the applicability of this method extends to earthquake monitoring in a global or regional setting. I have submitted this work for the 2019 Society of Exploration Geophysicists Annual Convention and the chapter for publication in a peer-reviewed journal.

Seismic wavefield imaging and tomography are commonly used to obtain a physical representation of the subsurface properties. However, these methods are often based on approx-

imate acoustic wave physics, even when we record elastic data. Consequently, the inferred physical properties of the subsurface may not reflect correct and plausible geologic structures, which prompts the need to obtain subsurface properties utilizing elastic wavefields. A fundamental step towards elastic wavefield tomography and imaging is to reconstruct the wavefields from the recorded data. The representation theorem states that to extrapolate the recorded seismic data accurately requires both stress and displacement data (Aki and Richards, 2002). However, conventional multicomponent technology is limited to recording only the vector components of the wavefields giving rise to approximate wavefield extrapolation that generates nonphysical waves, i.e., waves present in the simulation, but that have not propagated in the actual physical experiment (Yan, 2010; Ravasi and Curtis, 2013; Duan, 2016). Together with the acquisition technology discussed earlier, we can reach the full capabilities of elastic wavefield imaging. I illustrate the importance of removing the nonphysical waves with elastic seismic imaging using the Marmousi model (Bourgeois et al., 1991). This work has been presented at the 2018 Society of Exploration Geophysicists Annual Convention (Lim Chen Ning and Sava, 2018c).

In **chapter 5** of my thesis, I build on the representation theorem for accurate elastic wavefield extrapolation to significantly improve the storage and I/O requirements for elastic seismic wavefield-based migration. I demonstrate the effectiveness of this method on memory intensive applications such as reverse time migration (RTM) that requires the forward propagated wavefield to be readily available as the receiver-side wavefield is backward extrapolated for the imaging process. Instead of storing the entire source wavefield, I save the wavefield information on a single layer around the computational domain to accurately reconstruct the forward wavefield from the source concurrently with the backward wavefield from the receiver. I show using numerical examples that iterative schemes such as least-squares RTM produce accurate representations of the elastic subsurface for arbitrary anisotropy and heterogeneity without any negative impact from the boundary reconstruction, and without slow disk access. I also test my method using DAS vertical seismic profile (VSP) data from the

Eagle Ford shale formation in Texas, USA. I have submitted my work for the 2019 Society of Exploration Geophysicists Annual Convention and this chapter to a peer-reviewed journal.

CHAPTER 2

MULTICOMPONENT DISTRIBUTED ACOUSTIC SENSING: CONCEPT AND THEORY

A paper published* in *Geophysics*

Ivan Lim Chen Ning[1,2,3] and Paul Sava[1]

Distributed Acoustic Sensing (DAS) data are increasingly used in geophysics. Lower in cost and higher in spatial resolution, DAS data are appealing especially in boreholes where optical fibers are readily available. DAS has the potential to become a permanent reservoir monitoring tool with a reduced sensing time interval. In order to accomplish this goal, it is critical that DAS can record all wave modes to fully characterize reservoir properties. This goal can be achieved by recording the complete strain tensor consisting of six-components. Conventional DAS provides projections of these components along the optical fiber by observing deformation along the fiber. To obtain the entire six-component strain tensor, we propose an approach using multiple strain projections measured along optical fibers with judiciously chosen geometry specifically. We propose designs combining multiple helical configurations or a single helical configuration together with a straight optical fiber that allow access to multiple strain projection. We group multiple strain projections in a given spatial window to perform reconstruction of the entire strain tensor in a least-squares sense under the assumption that the seismic wavelength is larger than the analysis window size. We demonstrate how optimal optical fiber parameters can be selected using a scan of the entire

*Reprinted with permission of *Geophysics*, Vol. 83, No. 2 (March-April 2018), pp. P1-P8

[1]Graduate student and Professor, respectively, Center for Wave Phenomena, Colorado School of Mines, 1500 Illinois St., Golden, CO 80401, USA

[2]Primary researcher and author

[3]Author for correspondence

configuration space, and analyzing the condition number associated with the geometry of the optical fibers. We illustrate our method through synthetic experiments using realistic fiber geometry and wavefields of arbitrary complexity.

2.1 Introduction

Distributed Acoustic Sensing (DAS) is rapidly gaining popularity in the oil and gas industry, especially for Vertical Seismic Profile (VSP) imaging and for reservoir monitoring (Mestayer et al., 2011; Cox et al., 2012; Mateeva et al., 2012, 2013; Daley et al., 2013; Madsen et al., 2013). The advantages of DAS for borehole applications in terms of cost, the deployment mechanism, and spatial resolution make its use more attractive than conventional geophone acquisition (Lumens et al., 2013; Mateeva et al., 2013). The application of optical fiber in wells is not an unfamiliar method as optical fiber has long been used for temperature measurement known as Distributed Temperature Sensing (DTS) (Hartog, 2000; Karaman et al., 1996).

DAS transforms an optical fiber into a distributed array of strain measuring tools. The acquisition requires an interrogator unit (IU) to send laser pulses into the optical fiber and detect back-scattered light from inhomogeneities along the fiber. These inhomogeneities are impurities caused either deliberately during manufacturing with the use of dopants or by manufacturing defects (Uzunoglu, 1981; Tsujikawa et al., 2005). The back-scattering generated by these inhomogeneities is called Rayleigh scattering. Analyzing the changes in phase of the back-scattered light gives access to information such as strain as a function of distance from the IU through Coherent Optical Time-Domain Reflectometry (COTDR).

The underlying principle behind CODTR is to analyze the phase difference between the back-scattered signal from two points along an optical fiber (Bakku, 2015). The distance separating the two points is known as gauge length. Introducing disturbance to the optical fiber generates perturbation to the otherwise constant phase difference between the two measurement points. This additional phase difference is quasi-linearly proportional to the average axial strain between the two points. Legacy DAS systems that analyze back-scatters

require a gauge length of around 1 m to achieve acceptable signal-to-noise ratio (SNR) measurements. However, recent hardware uses specially designed optical fibers and the gauge length can be reduced to 0.05 m while maintaining acceptable SNR (Farhadiroushan et al., 2016). In this paper, we focus on a range of gauge lengths and emphasize smaller sizes that characterize instrumentation currently being deployed or which is expected to come online shortly.

As indicated by Lumens (2014) and Bakku (2015), the DAS system is more sensitive in the axial direction compared to the radial direction, thus reducing the DAS measurable data to the axial strain, which can be measured with acceptable signal-to-noise ratio. Most of the DAS deployments are focused on borehole applications and multicomponent seismic data are desirable for use in seismic characterization and monitoring (Davis et al., 2003; Stewart et al., 2003). Several publications suggest that three-component (3C) sensing using DAS is possible (den Boer et al., 2012, 2013; Kragh et al., 2014; Hartog et al., 2014; Crickmore and Hill, 2014; Farhadiroushan et al., 2015); however, no published work details mechanisms for extracting the six-component (6C) strain tensor from axial strain measurement using DAS. Geophones can record multicomponent data; however, they are costly and do not provide the dense spatial sampling of DAS. In this paper we investigate possibilities for using different optical fiber configurations in order to gain access to multicomponent information.

We propose an approach for acquiring multicomponent data with the use of multiple strain projection measurements. In order to achieve these measurements, we use various helical fiber configurations. Existing helical optical fiber configurations for DAS (den Boer et al., 2013; Kuvshinov, 2016; Hornman, 2017) are designed to detect broadside acoustic signals, i.e. waves that arrive at large angles relative to the axis of the optical fiber. However, here we are interested in using the projections of the strain tensor along the optical fiber in order to reconstruct the full six-dimensional strain tensor at points along the optical fiber. Using the characteristics of the helix and the axial strain measurement of the optical fiber, we can evaluate the entire strain tensor at every measuring location under the assumption

that the seismic wavelength is significantly longer than the helix period. We show the theoretical relationship between the measured axial strain in the optical fiber and the full strain tensor in the surrounding area, and demonstrate the applicability of this strategy using 3D synthetic examples of complex seismic wavefields. Our method accounts for the gauge length characterizing the DAS measurements.

In this paper, we assume a DAS system that can acquire data using gauge lengths of 0.2 m and 1.0 m with realistic lengths of optical fiber cable. The gauge length of 1.0 m has been reported in the literature by Daley et al. (2013). Using this gauge length, we consider a cable that can typically be deployed for reservoir monitoring in a borehole environment; a helically-wound cable (Kuvshinov, 2016; Hornman, 2017) increases the overall length of the optical fiber. If we assume the seismic bandwidth of 10 to 100 Hz, the current DAS systems can provide a dynamic range 80 dB or higher. If we deploy an optical fiber cable with improved reflective properties as suggested by Farhadiroushan et al. (2016), we may further increase the dynamic range. We thus assume a system comparable to currently available acquisition systems which might improve in the future. The other gauge length we consider is 0.2 m which would be beneficial for engineering applications using shorter cables, which is capable of acquiring higher frequencies.

We begin by reviewing the theoretical aspects of the proposed approach, followed by 3D synthetic examples. While discussing the results, we also review the associated assumptions and limitations to this approach. We then propose a feasible configuration that allows our method to be practically implemented using current optical fiber technology.

2.2 Theory

The axial strain measurement by DAS is a projection of the strain tensor from the surrounding area as a function of the optical fiber position. We use the intrinsic coordinate system of a curve as the local coordinate system for the optical fiber with respect to the global coordinate system (Lin and Pisano, 1988). Since DAS measures axial strain, it suffices to use the tangent vector along the optical fiber to perform strain tensor projection. We

exploit the helical geometry as a tool to measure different projections of the strain field onto the optical fiber, i.e we measure the projection of the surrounding strain tensor along the optical fiber as a function of the pitch angle and azimuth angles. We adopt the definition of Lin and Pisano (1988) on pitch angle as the complement of the angle between the tangent vector and the axial direction of the DAS cable.

The relationship between the axial strain measured by the optical fiber and the strain tensor of the surrounding area can be expressed through the strain tensor coordinate transformation relationship as (Young and Budynas, 2002)

$$\bar{\boldsymbol{\varepsilon}} = \mathbf{R}\boldsymbol{\varepsilon}\mathbf{R}^{\mathbf{T}} \,, \tag{2.1}$$

where the $\bar{\boldsymbol{\varepsilon}}$ and $\mathbf{R}$ denote the transformed strain tensor and the transformation (also known as rotation) matrix respectively. We rearrange equation 3.3 as

$$\mathbf{b} = \mathbf{G}\mathbf{m} \,, \tag{2.2}$$

where $\mathbf{b}$ and $\mathbf{m}$ are the vectorized transformed and original strain tensors respectively. The matrix $\mathbf{G}$ is the expansion of equation 3.3 using the transformation matrix $\mathbf{R}$. The axial strain measurement reduces $\mathbf{b}$ and $\mathbf{G}$ to single row matrices. Figure 2.1 illustrates strain tensor projections onto a vector together with the $\mathbf{G}$ matrix representation.

In equation 3.2, the projection $\mathbf{b}$ refers to a point along the optical fiber. As DAS measures an average strain within a gauge length, we introduce an averaging operator $\mathbf{A}$ to account for this effect. The gauge length averaging is as following

$$\begin{matrix}\mathbf{d}\\ \end{matrix} \quad \begin{matrix}\\ \end{matrix} \quad \begin{matrix}\\ \end{matrix} \quad \begin{matrix}\mathbf{A}\\ \end{matrix} \quad \begin{matrix}\\ \end{matrix} \quad \begin{matrix}\mathbf{b}\\ \end{matrix}$$
$$\begin{bmatrix} d_1 \\ \vdots \\ d_M \end{bmatrix} = \frac{1}{L} \begin{bmatrix} \Delta S & \Delta S & 0 & 0 & 0 \\ 0 & 0 & \ddots & 0 & 0 \\ 0 & 0 & 0 & \Delta S & \Delta S \end{bmatrix} \begin{bmatrix} b_1 \\ \vdots \\ b_N \end{bmatrix} \,, \tag{2.3}$$

where N and M is the number of measurements before and after performing gauge length averaging respectively. ΔS is the spacing between the strain measurements and L denotes the gauge length. To perform strain tensor reconstruction, we group consecutive strain measurements along the optical fiber within a defined window. These measurements represent

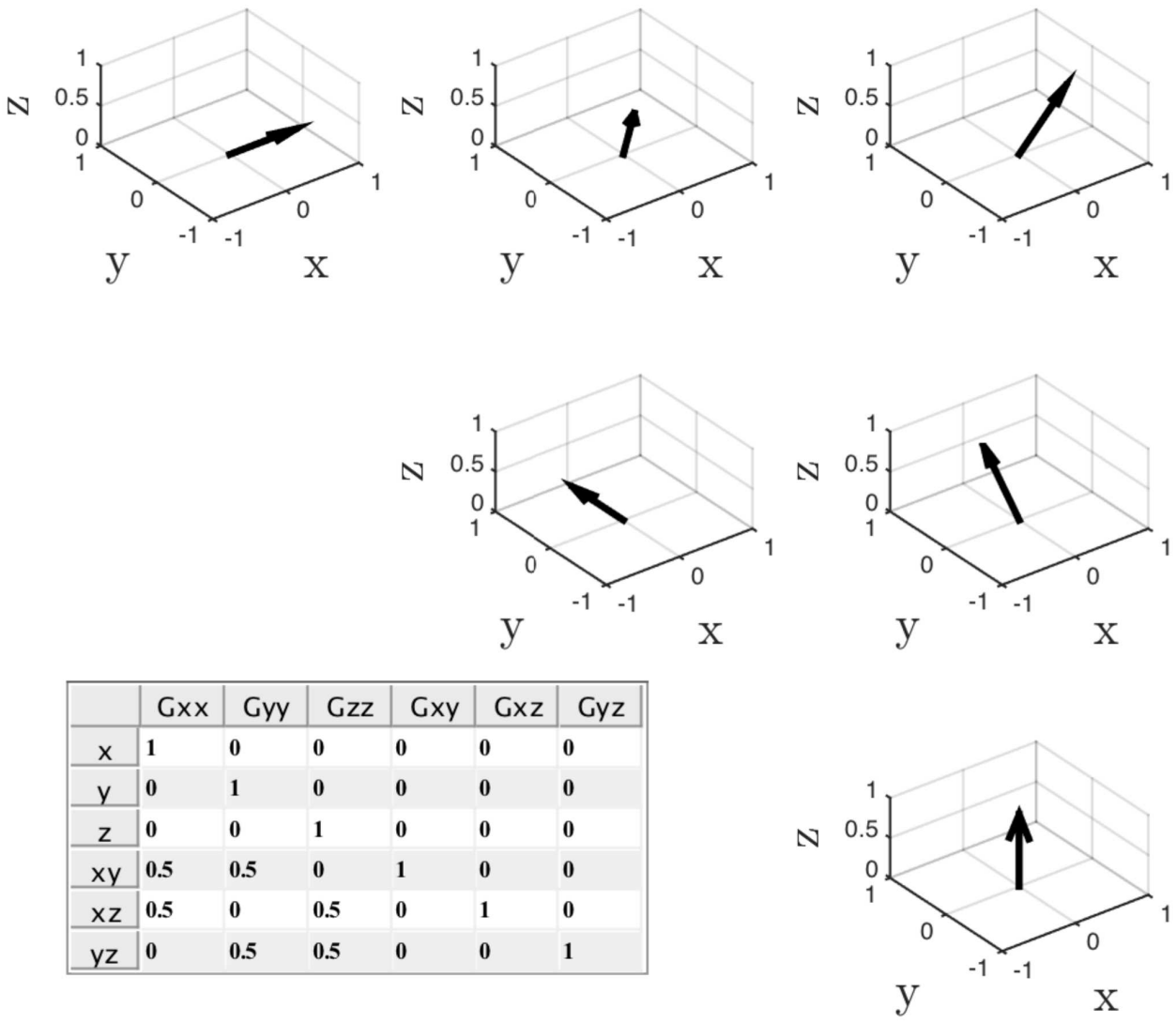

	Gxx	Gyy	Gzz	Gxy	Gxz	Gyz
x	**1**	**0**	**0**	**0**	**0**	**0**
y	**0**	**1**	**0**	**0**	**0**	**0**
z	**0**	**0**	**1**	**0**	**0**	**0**
xy	**0.5**	**0.5**	**0**	**1**	**0**	**0**
xz	**0.5**	**0**	**0.5**	**0**	**1**	**0**
yz	**0**	**0.5**	**0.5**	**0**	**0**	**1**

Figure 2.1: Examples of strain tensor projection onto the vectors pointing along and oblique relative to the directions of X-, Y-, and Z-axis. The columns of the bottom left table show contribution of strain elements in terms of the **G** matrix in equation 3.2 and the rows represent the different vectors respectively.

the data vector $\mathbf{d}$ and account for strain averaging within a gauge length. The reconstructed strain tensor refers to the middle of the window. Here, we make the assumption that the seismic wavelength is much greater than the length of the window. This assumption is important so that we can group multiple measurements within the window to refer to the same strain tensor field at a given location. A large seismic wavelength relative to the considered window along the fiber provides a slowly varying strain tensor field which we can assume to be invariant within the window used for its reconstruction.

We can solve for the strain components (the model $\mathbf{m}$ in equation 3.2) in a least-squares sense, based on the known kernel or forward operator $\mathbf{G}$ and averaging operator $\mathbf{A}$. The data $\mathbf{d}$ are consecutive axial strain measurements along the helical optical fiber within a window as indicated earlier (this implies that the strain tensor that we are reconstructing does not change within this window or segment along the optical fiber), and the model ($\mathbf{m}$) is the strain tensor at a given location. We reiterate that the measurements contained in vector $\mathbf{d}$ are subject to averaging within a gauge length; this effect is captured by the averaging matrix $\mathbf{A}$ of known size. We minimize the objective function

$$\mathcal{J} = \frac{1}{2}\|\mathbf{W}(\mathbf{AGm} - \mathbf{d})\|^{\mathbf{2}} \,, \tag{2.4}$$

where $\mathbf{W}$ is a weighting operator that represents the uncertainty of the projection matrix derived from the geometry of the optical fiber. For simplicity, the reconstructions in the following examples, we use identity as the weighting matrix. The model $\mathbf{m}$ can be expressed as

$$\mathbf{m} = (\mathbf{G^T A^T AG})^{-\mathbf{1}}\mathbf{G^T A^T d} \,. \tag{2.5}$$

To investigate the types of configurations that allow us to perform strain tensor reconstruction, we explore the configuration by den Boer et al. (2013) that uses two helical optical fiber and a single straight optical fiber in the middle. The total of three optical fibers in principle could provide three-component (3C) sensing. However, our target reconstruction is a six-component (6C) strain tensor. To analyze the suitability of this three optical fibers

configuration, we use two helical optical fibers with a diameter of 0.0244 m (about 1 in) together with the pitch angles of 20° and 60° respectively. Since DAS with a small gauge length is achievable (Farhadiroushan et al., 2016), we use a gauge length of 0.1 m. To accurately analyze the DAS acquisition that measures average strain within a gauge length, we use the averaging matrix $\mathbf{A}$ together with the projection matrix $\mathbf{G}$. Using these matrices, we calculate the singular value decomposition (SVD) of the Gram matrix $\mathbf{G^T A^T A G}$. The singular values from the SVD analysis of the Gram matrix provide insight into the suitability of a given configuration for strain tensor reconstruction using our approach. An example of this three optical fibers configuration is illustrated in Figure 2.2(a) together with the singular values after performing SVD in Figure 2.2(d). In the SVD analysis, the Gram matrix uses measurements in a window of 5 m assuming that the seismic wavelength is much greater than the window. Based on the SVD results, the singular values of the Gram matrix indicate that it is full rank and can be used for strain tensor reconstruction.

We further simplify the three optical fibers configuration by omitting the helical optical fiber with the pitch angle of 60°. This gives us a configuration using only two optical fibers. An example of this configuration is shown in Figure 2.2(b) and the corresponding singular values from SVD in Figure 2.2(e). Although there is some slight reduction in the singular values, this simplified configuration is still full rank and can be used for strain tensor reconstruction. In this paper, we show numerical examples using this simplified configuration of two optical fibers.

We also investigate a different configuration by introducing a varying pitch angle helical optical fiber (we refer to this configuration as a chirping helical optical fiber). An example of such configuration is shown in Figure 2.2(c) with a diameter of 0.0244 m (about 1 in) where we perform a pitch angle down-sweep and up-sweep within a window of 0.15 m giving a total of ten complete helix turns. The example configuration is not used for the SVD analysis as this is for plotting purposes only. The configuration we use that gives the singular values in Figure 2.2(f) is a pitch angle down-sweep and up-sweep within a window of 5 m giving a

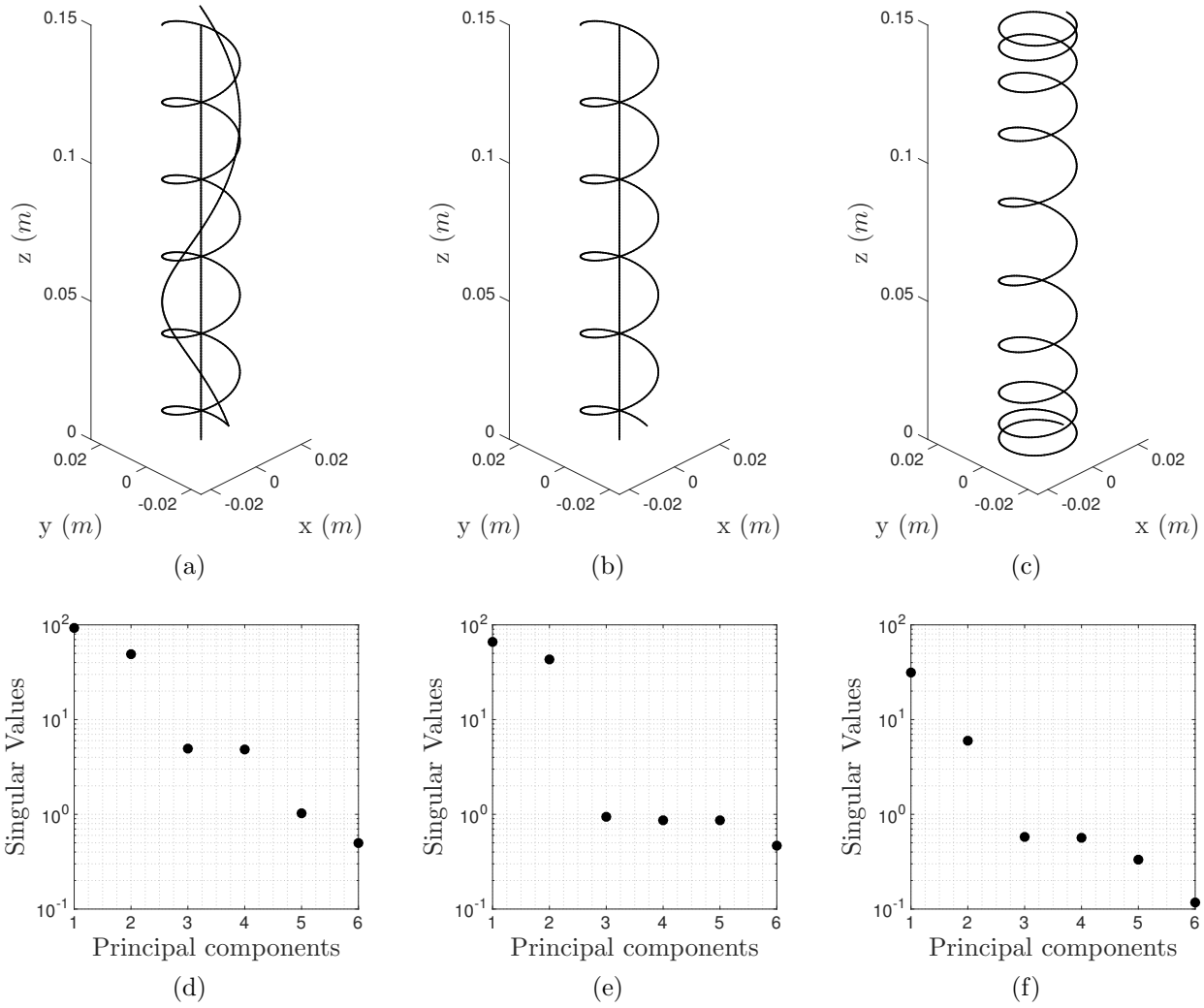

Figure 2.2: Examples of optical fiber configurations with (a) two helical optical fiber with pitch angle of 20° and 60° and a single straight optical fiber, (b) one helical optical fiber with pitch angle of 20° and a single straight optical fiber. (c) A simplified example of the chirping helix configuration for plotting purposes. The helixes are constructed with a diameter of 0.0244 m (about 1 in). (d), (e), and (f) are the singular value decomposition (SVD) of the Gram matrix in equation 3.4 for the corresponding configurations. The Gram matrix uses measurements in a window of 5 m.

total of 100 number of turns. We emphasize that, we assume the seismic wavelength is much greater than the window. The singular values are slightly lower than that of the previous configurations, but the chirping helix configuration is still full rank. A full rank Gram matrix indicates that we are able to reconstruct the strain tensor. It is worth noting that the chirping configuration only requires one optical fiber albeit with increased complexity that may be difficult to engineer using an optical fiber and may increase the complexity of deployment.

We further examine the effects of the helical optical fiber design parameters on the Gram matrix by performing a parameter scan as shown in Figure 2.3. We fix the diameter of the helical optical fiber at 0.0244 m (about 1 in) to restrict the parameter search space. For the dual optical fibers configuration, we find the optimum design parameters (i.e. window length for reconstruction and pitch angle of the helical optical fibers) associated with low condition numbers, as shown in Figures 2.3(a) and 2.3(b) for gauge lengths of 0.2 m and 1.0 m respectively. If a given reconstruction window captures sufficient strain projections that can fully characterize the surrounding strain tensor, further increasing the reconstruction window size does not improve the condition number, since it has already reached an optimum value, as shown in Figures 2.3(a) and 2.3(b). Nevertheless, the reconstruction window should be kept at a minimum to preserve spatial resolution. Similarly, using the chirping helical optical fiber configuration, we scan for the optimum design parameters (i.e. window length for reconstruction and the number of helical turns within a window) associated with low condition numbers, as shown in Figure 2.3(c) and 2.3(d) for gauge lengths of 0.2 m and 1.0 m respectively.

The strain measurement by the DAS system using a helical geometry undergoes strain averaging in the azimuthal direction along the optical fiber within a gauge length. When the gauge length is equal to a multiple of the helix lead (the axial advance of a helix for a complete 360° turn), the DAS measurement does not contain azimuthal information, which translates into a large high condition number. Using the dual optical fibers configuration with a cable diameter of 0.0244 m (about 1 in) and a gauge length of 0.2 m, as shown in

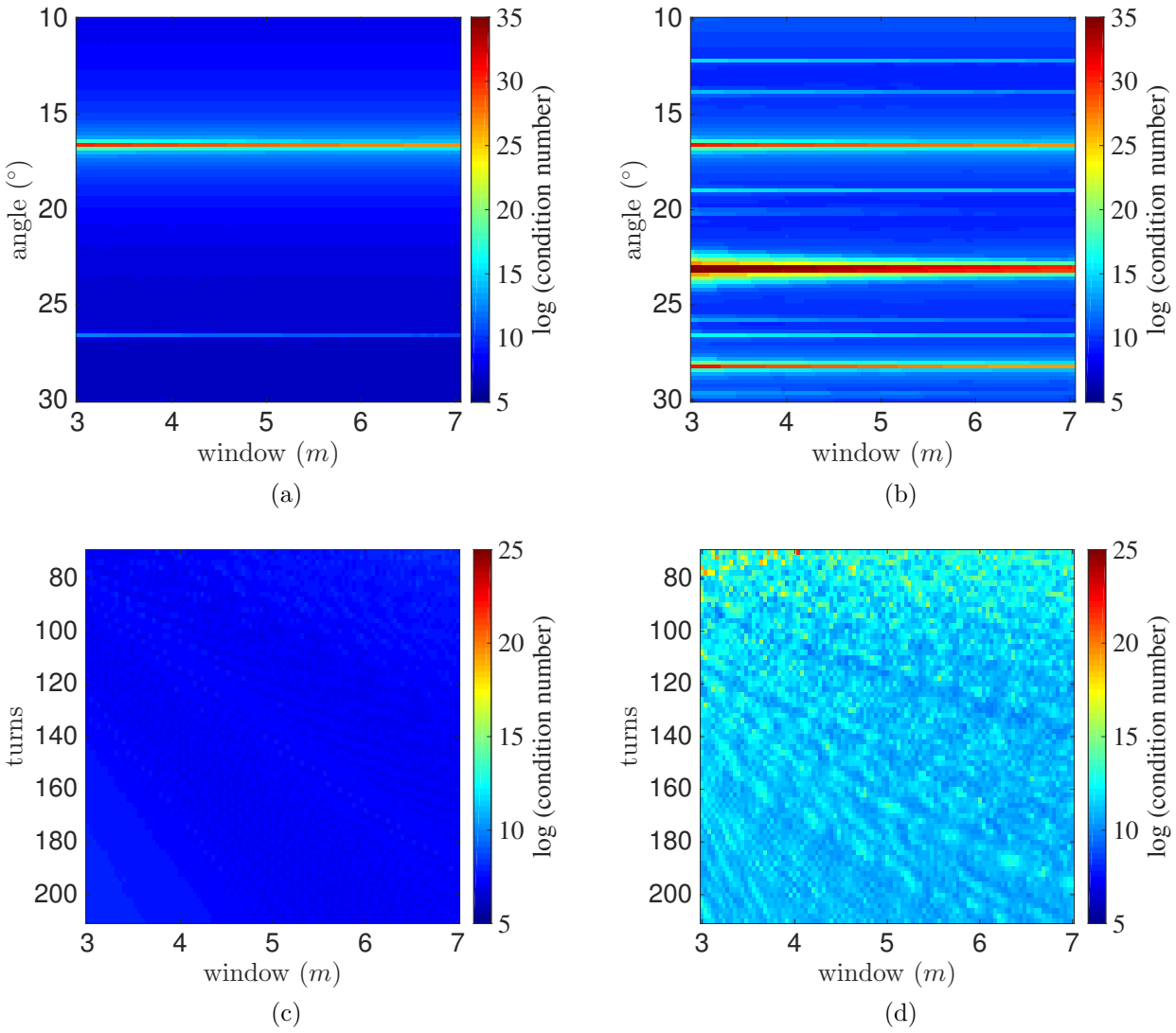

Figure 2.3: Condition number of the Gram matrix using a fixed diameter at 0.0244 m (about 1 in) with the **dual optical fibers** configuration at gauge lengths of (a) 0.2 m and (b) 1.0 m for window from 3 to 7 m and pitch angle from 10° to 30°. Similarly, the condition number with the **chirping helical optical fiber** configuration at gauge lengths of (c) 0.2 m and (d) 1.0 m for window from 3 to 7 m and number of turns within a window from 10 to 210 turns.

Figure 2.3(a), we observe a large condition number linear feature for pitch angles between 16° to 17°. As every single measurement within this pitch angle range contains little or no azimuthal information, the condition number remains high regardless of the window size. Increasing the gauge length to 1.0 m in Figure 2.3(b), we observe an increasing number of high condition number features. This increase in number is due to the higher azimuthal averaging along the helical fiber within a longer gauge length. However, the range for the condition number of both gauge lengths remains relatively consistent, suggesting that accurate reconstruction can be achieved with careful selection of design parameters.

In the case of a chirping helical optical fiber configuration with a gauge length of 0.2 m in Figure 2.3(c), we can see that the condition number range is significantly lower than the dual optical fibers of the same gauge length. The chirping helix provides a larger range of strain projections which improves the reconstruction results as demonstrated by the overall low condition numbers. However, the condition number range increases rapidly with a larger gauge length of 1.0 m, as shown in Figure 2.3(d). The condition number amplified more than 10 times suggests that the chirping helix configuration can only be deployed if a small gauge length is used.

2.3 Numerical examples

Using synthetic examples of complex seismic wavefields, we illustrate the reconstruction of the six-dimensional strain tensor from axial strain measurements along the proposed optical fiber geometries. In the reconstruction, we choose a window size of 5 m that is approximately 6 times smaller than the smallest seismic wavelength of 33.33 m. The following examples are simulated using elastic finite-difference modeling with a velocity model containing a low-velocity Gaussian anomaly to produce wavefield triplications as shown in Figure 2.4(c). A snapshot of the wavefield triplication is shown in the bottom right panel of Figure 2.4(d). We use a gauge length and a channel spacing of 0.2 m for our DAS data simulation. The channel spacing refers to the distance between consecutive average strain measurements within a gauge length. Although such small gauge length is possible, as indicated by Farhadiroushan

et al. (2016), we also perform simulations using a gauge length and channel spacing used in more conventional DAS acquisition systems at 1.0 m. Using such short gauge lengths, the effect of wavenumber filtering discussed by Dean et al. (2017) is negligible. In our setup, we assume perfect coupling between the optical fiber to the surrounding (i.e. cementing), which is a common assumption for DAS analysis of any geometry.

Figure 2.4(a) shows the experiment setup where the dot represents the source location, and the straight line with the coordinates (x_b, y_b) is a borehole segment in which the helical configurations are positioned. Figure 2.4(b) shows the observed strain tensor along the straight line at (x_b, y_b) in a strain tensor matrix layout which is the target for strain reconstruction. The horizontal axis of the individual panels represents the reconstructed measurements along the optical fiber and the vertical axis represents time. Figure 2.5(a) shows the reconstructed strain tensor using the dual optical fibers configuration with a helical optical fiber and a straight optical fiber in the middle using a gauge length and channel spacing of 0.2 m. The helical optical fiber has a diameter of 0.0244 m (about 1 in) and a pitch angle of 20°. Using this configuration, we are able to successfully reconstruct the strain tensor which is evident on the difference plot between the observed and reconstructed strain tensor amplified 10 times, as shown in Figure 2.5(b). We quantify the quality of strain reconstruction using

$$\eta = \frac{\left\|\mathbf{m^{obs}} - \mathbf{m^{rec}}\right\|^2}{\left\|\mathbf{m^{obs}}\right\|^2} 100 \ , \tag{2.6}$$

where $\mathbf{m^{obs}}$ represents the observed strain tensor and $\mathbf{m^{rec}}$ represents the reconstructed strain tensor. The scalar values for η in the case of the dual optical fibers configuration are less than 0.4%. Figure 2.5(c) shows the reconstructed strain tensor using the same configuration but with the gauge length and channel spacing at 1.0 m. The differences shown in Figure 2.5(d) (also amplified 10 times) suggest that the increase of gauge length has a negative impact on our reconstruction. Although the calculated values for η increase overall with the larger gauge length, the highest η is less than 4.5% which is a perfectly

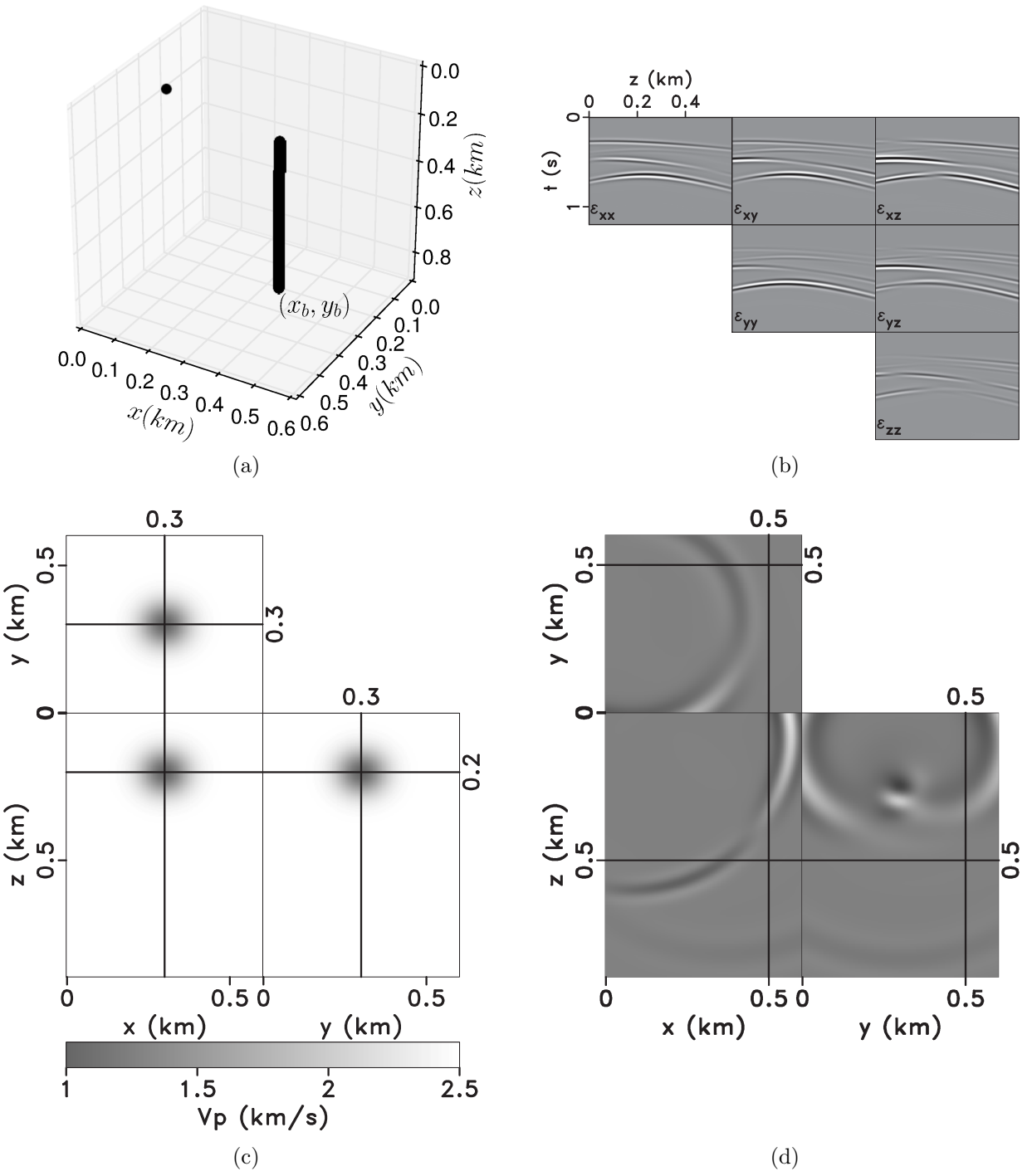

Figure 2.4: (a) Schematic representation of a DAS experiment depicting the source (dot) and receiver (line) locations. (b) The ideal strain tensor that we would like to reconstruct from DAS measurements. (c) The P-wave velocity model containing a low velocity Gaussian anomaly designed to produce wavefield triplications. The S-wave velocity is half of the P-wave velocity. (d) A snapshot of the vertical displacement wavefield.

acceptable accuracy level for practical applications.

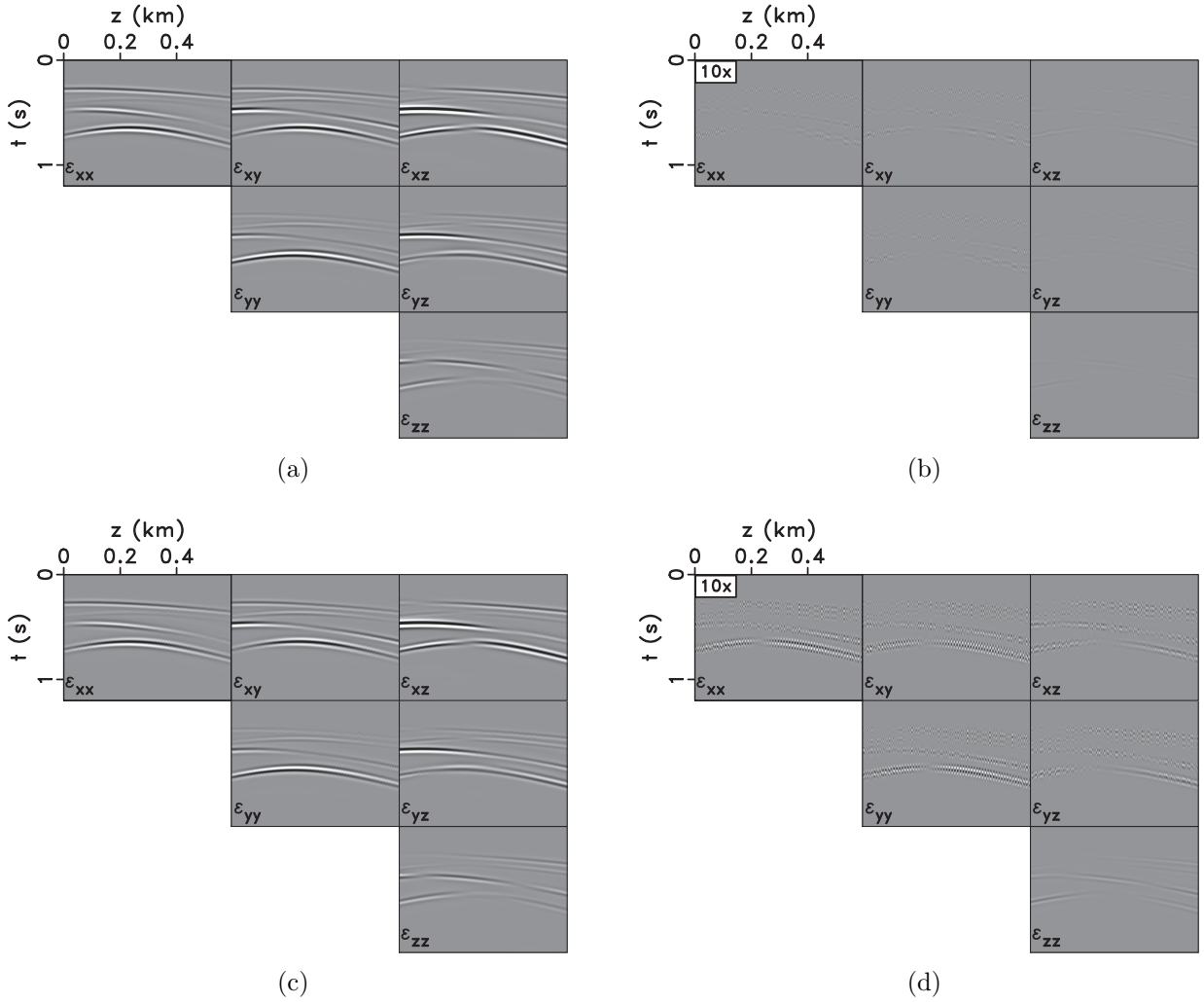

Figure 2.5: Strain tensor reconstructed using the **dual optical fibers** configuration with one helical and one straight optical fiber shown in Figure 2.2(b) using a gauge length and channel spacing of (a) 0.2 m and (c) 1.0 m. (b) and (d) are the difference between the ideal strain tensor in Figure 2.4(b) and the respective reconstructed tensor in (a) and (c) magnified 10 times.

We perform the same numerical analysis on the chirping helical optical fiber configuration with a diameter of 0.0244 m (about 1 in), where we perform a pitch angle down-sweep and up-sweep within a window of 5 m giving a total of 100 number of turns. Figure 2.7(a) shows the reconstructed strain tensor with a gauge length and channel spacing of 0.2 m. The results show that we are able to achieve comparable reconstruction quality to the dual optical fibers

configuration by observing the amplified 10 times difference plot in Figure 2.7(b). The η values for the chirping configuration are less than 0.3%. The reconstruction results using a gauge length of 1.0 m is not shown here due to the significant uncertainty associated with the massive condition number, as shown in Figure 2.3(d).

We also test the reconstruction process for both configurations by adding random noise with 5% of the maximum amplitude of the data and in the data frequency band. Therefore in places where the signals are weak, the noise overwhelms the signal. Using the dual optical fibers configuration with gauge length and channel spacing of 0.2 m, Figure 2.6(a) shows that we are able to reconstruct the strain tensor. The difference plot in Figure 2.6(b) shows primarily random noise. The strain tensor reconstruction with a larger gauge length and channel spacing at 1.0 m is shown in Figure 2.6(c). Although the reconstructed strain tensor is contaminated with noise, we can observe some of the stronger arrivals in all of the strain components. The difference plot shown in Figure 2.6(d) contains primarily noise.

We use the same noise characteristics for the chirping configuration. Figure 2.7(c) shows the reconstructed strain tensor using the chirping configuration with a gauge length and channel spacing of 0.2 m with added noise. We successfully reconstruct the strain tensor, although it contains slightly higher noise level than the dual optical fibers configuration. The difference plot in Figure 2.7(d) contains primarily noise. The reconstruction using a larger gauge length and channel spacing at 1.0 m is not shown here as the noise overwhelms the actual data due to the large condition number associated with this configuration.

2.4 Discussion

Our investigation shows that the full strain tensor can be reconstructed with a high level of accuracy either using two optical fibers (one helical optical fiber with a pitch angle of 20° and a straight optical fiber) or a single chirping helical optical fiber. However, a relatively small but achievable gauge length is required to ensure good (low η) reconstruction under the influence of noise for small diameter helical configurations. This is often restricted by the dimension of the borehole. If we consider applications such as surface seismic acquisition

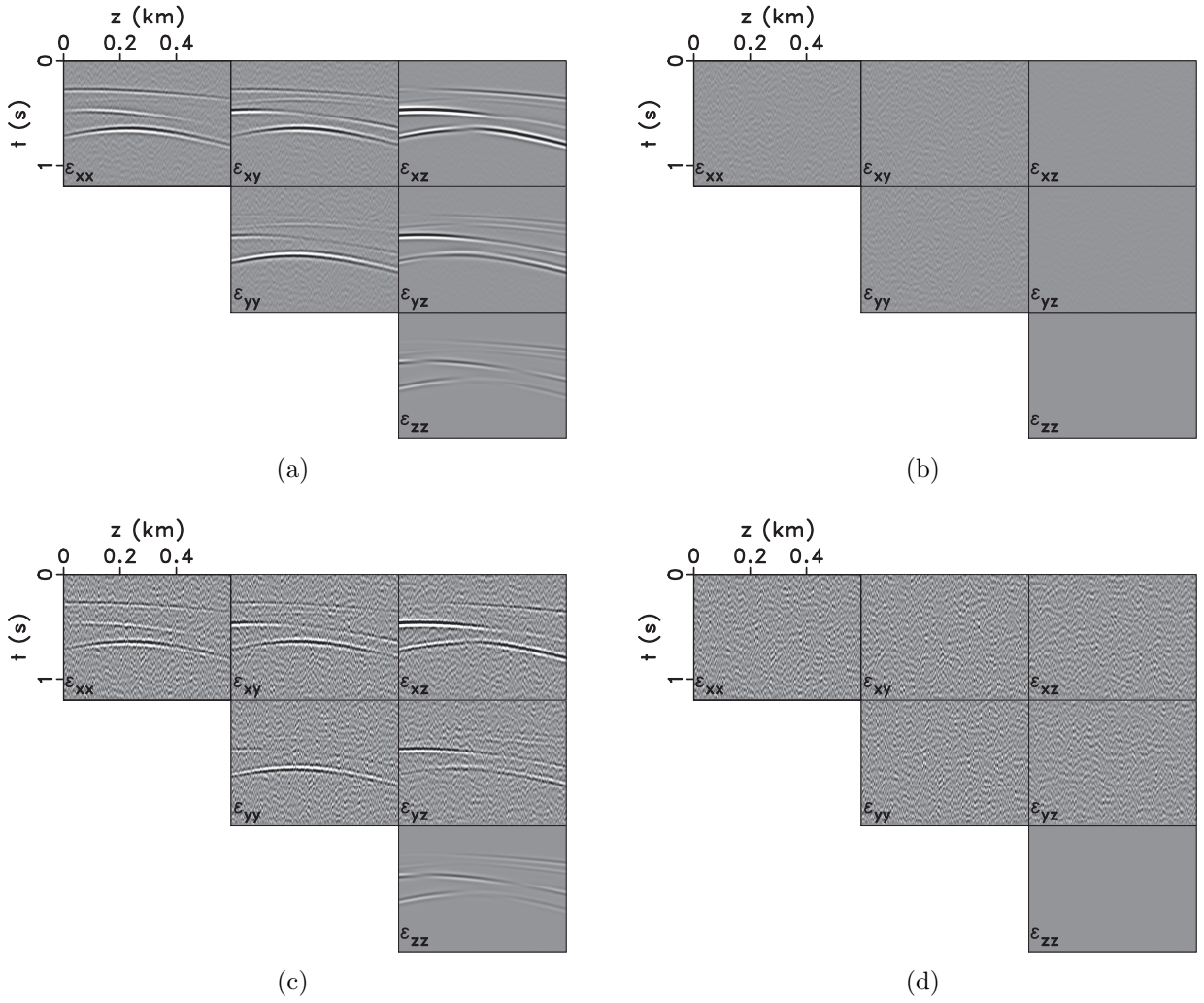

Figure 2.6: Strain tensor reconstructed from data containing random noise with 5% of the maximum data amplitude and band-limited to the data band using the **dual optical fibers** configuration with one helical optical fiber and one straight optical fiber shown in Figure 2.2(b) using a gauge length and channel spacing of (a) 0.2 m and (c) 1.0 m. (b) and (d) are the difference between the ideal strain tensor in Figure 2.4(b) and the respective reconstructed tensor in (a) and (c).

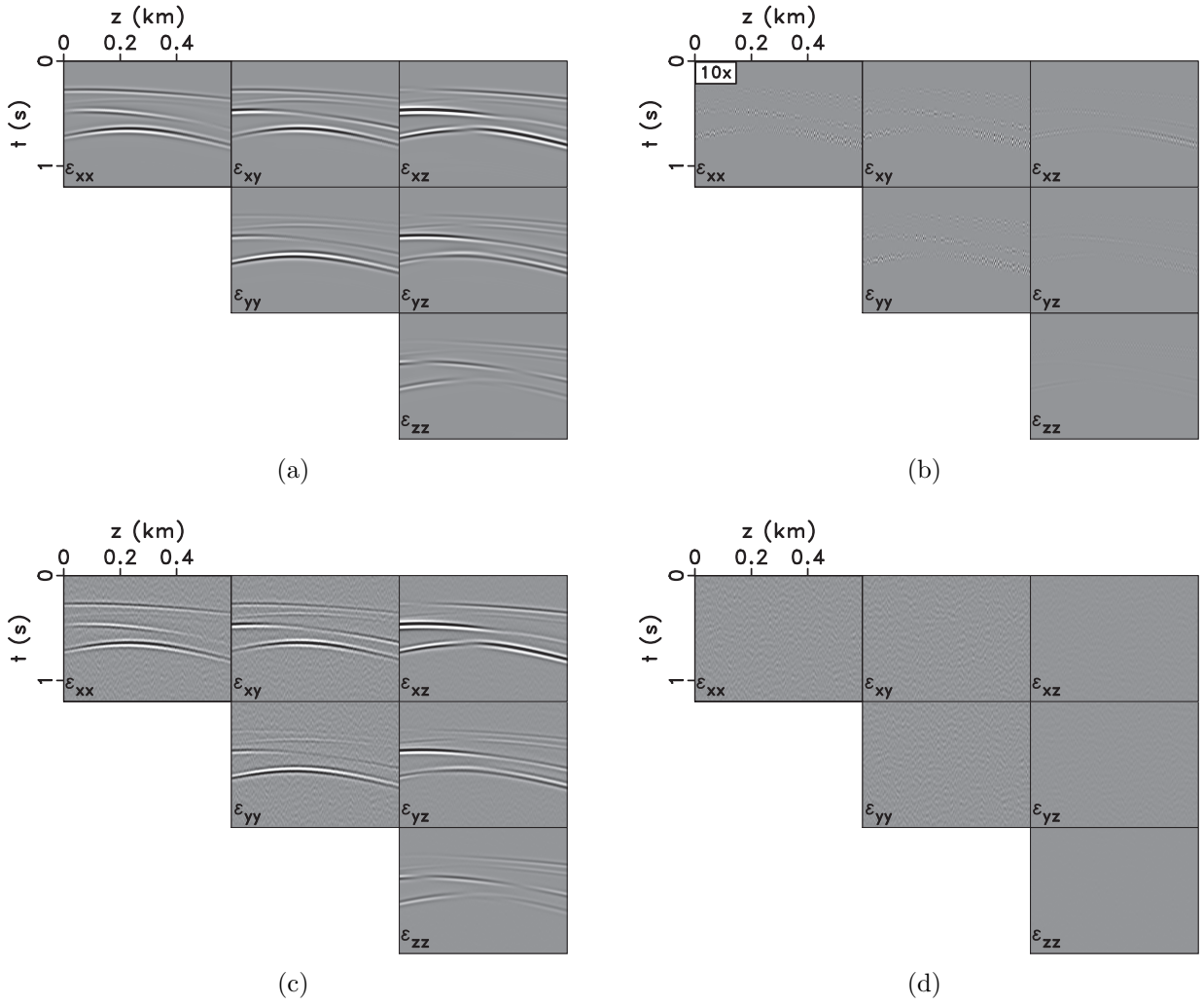

Figure 2.7: Strain tensor reconstructed using the **chirping helical optical fiber** configuration using a gauge length and channel spacing of 0.2 m is shown in panel (a) and panel (c) shows the reconstruction under the influence of random noise with 5% of the maximum data amplitude and band-limited to the data band. The difference between the ideal strain tensor in Figure 2.4(b) and the respective reconstructed tensor in (a) and (c) are shown in panels (b) magnified 10 times and (d).

where the dimensions are more relaxed, increasing the diameter of the helical configuration allows for a larger gauge length, which in turn enables strain tensor reconstruction in noisier environments.

As shown in the earlier sections, we can reconstruct the strain tensor using only a single chirping helical optical fiber. However, we also show that the reconstruction under the influence of noise is inferior to the two optical fiber configuration. Although we only need to deploy a single optical fiber, this comes at the expense of reconstruction quality. In addition, the engineering and deployment of such complex configuration are challenging. An alternative is to use two optical fiber with one helical optical fiber and one straight optical fiber. Besides being more robust in the presence of noise, the engineering and deployment are less challenging than the chirping helical optical fiber.

Overall, the dual optical fibers configuration has a lower condition number for the Gram matrix compared to the single chirping helical optical fiber. The condition number gives us a measure of how sensitive our reconstruction is under the presence of noise. A small condition number implies that we are able to reconstruct the strain tensor well under the influence of noise. In our examples, using a gauge length of 0.2 m allows us to reconstruct a good quality (low η) strain tensor for both configurations. However, increasing the gauge length to 1.0 m increases the condition number which is evident from the increased level of noise after reconstruction and especially in the chirping configuration where the results are overwhelmed by noise. However, the dual optical fibers configuration can be deployed with currently available DAS systems.

All the design parameters for the helical optical fiber affect one another and there is no one optimum set of parameters that may suit all situations. However, we may define some limiting parameters such as the diameter of the helix (in the case of a borehole) and then adjust the remaining parameters based on noise and accuracy requirements. In the end, the design goal is to obtain configuration(s) that have a full rank Gram matrix $\mathbf{G^T A^T A G}$ calculated from the averaging $\mathbf{A}$ and projection matrix $\mathbf{G}$. Such design parameter estimation

is shown in Figure 2.3 by evaluating the condition numbers for different geometries. The weighting operator shown in equation 2.4 can be used to reduce the reconstruction errors due to the uncertainty of the optical fiber geometry which translates into the uncertainty of the projection matrix $\mathbf{G}$. The shape-sensing method of Moore and Rogge (2012) is one mechanism to detect the actual shape of the deployed fibers, thus reducing the uncertainty in the geometry of the optical fiber.

2.5 Conclusions

We demonstrate that multicomponent distributed acoustic sensing is achievable using strain projection measured along optical fibers to reconstruct all components of the strain tensor. Several optical fiber configurations can be used to accomplish multiple strain projection measurements. The chirping helical optical fiber can reconstruct the strain tensor, but the manufacturing and deployment of such configuration may prove to be challenging. A more practical configuration uses a helical optical fiber and a straight optical fiber which is more robust in the presence of noise. As DAS is a rapidly evolving technology, DAS with smaller gauge length is imminent. Using conventional and smaller gauge lengths, we are able to accurately reconstruct the entire strain tensor, especially when the diameter of the helical optical fiber is small, as in the case of a borehole environment. Our numerical examples indicate that this type of acquisition can be used to reconstruct the full strain tensor for wavefields of arbitrary complexity and in the presence of noise in the band of the seismic data.

2.6 Acknowledgments

We would like to thank the sponsors of the Center for Wave Phenomena, whose support made this research possible and Martin Karrenbach of OptaSense for fruitful discussions. We are grateful to associate editor Guy Drijkoningen and the anonymous reviewers for their valuable comments that helped to improve the manuscript. The reproducible numeric examples in this paper use the Madagascar open-source software package (Fomel et al., 2013)

freely available from http://www.ahay.org.

CHAPTER 3

HIGH-RESOLUTION MULTICOMPONENT DISTRIBUTED ACOUSTIC SENSING

A paper published* in *Geophysical Prospecting*

Ivan Lim Chen Ning[1,2,3] and Paul Sava[1]

Distributed acoustic sensing (DAS) uses an optical fiber together with an interrogator unit to perform strain measurements. The usage of DAS in geophysics is attractive due to its dense spatial sampling and low operation cost if the optical fiber is freely accessible. In the borehole environment, optical fibers for DAS are often readily available as a part of other sensing tools, such as for temperature and pressure. Although the DAS system promises great potential for reservoir monitoring and surface seismic acquisition, the single axial strain measurement of DAS along the fiber is inadequate to fully characterize the different wave modes, thus making reservoir characterization challenging. We propose an acquisition system using five equally spaced helical optical fibers and a straight optical fiber to obtain six different strain projections. This system allows us to reconstruct all components of the 3D strain tensor at any location along the fiber. Analyzing the condition number associated with the geometry of the optical fiber, we can systematically search for the optimum design parameters for our configuration. Numerical examples demonstrate the effectiveness of our proposed method to successful reconstruction of the full strain tensor from elastic wavefields of arbitrary complexity.

*Reprinted with permission of *Geophysical Prospecting*, Vol. 66, No. 6 (2018), pp. 1111-1122

[1]Graduate student and Professor, respectively, Center for Wave Phenomena, Colorado School of Mines, 1500 Illinois St., Golden, CO 80401, USA

[2]Primary researcher and author

[3]Author for correspondence

3.1 Introduction

Distributed Acoustic Sensing (DAS) systems use an optical fiber as a distributed array of strain measuring tool. A typical DAS system employs an interrogator unit to send laser pulses into an optical fiber and detect back-scattered light along the fiber. DAS systems that operate on Coherent Optical Time-Domain Reflectometry (COTDR) provide average axial strain measurement through analyzing the perturbed phase difference between back-scattered light along the optical fiber from two points separated by a distance known as gauge length. Acceptable signal-to-noise ratio (SNR) measurements can be achieved using conventional DAS systems that require a gauge length of around 1 m. However, Farhadiroushan et al. (2016) show that the gauge length can be reduced to 5 cm, while maintaining satisfactory SNR using specially designed optical fibers.

Despite the recent technological advances in DAS, multicomponent DAS remains a missing piece of the puzzle to capture the full character of the seismic wavefield. In borehole application specifically, the usage of DAS focuses mainly on reservoir imaging (Mestayer et al., 2011; Mateeva et al., 2012, 2013; Wu et al., 2015; Zhan et al., 2015; Jiang et al., 2016) and velocity model updates (Wu et al., 2015; Li et al., 2015). Although, many examples show that DAS has the potential to provide low-cost reservoir monitoring (Hornman et al., 2015; Dou et al., 2016; Chalenski et al., 2016), the conventional single component DAS measurements makes reservoir characterization challenging. Since DAS acquires strain along the optical fiber, the measurement is a projection of the surrounding strain tensor as a function of the optical fiber position. As indicated by Lumens (2014) and Bakku (2015), the DAS system suffers from broadside sensitivity where the optical fiber is less sensitive to transversally impinging signals.

Although DAS measures axial strain, it is possible to obtain multicomponent data by reconstructing the entire strain tensor using multiple strain projections; manipulating the geometry of the optical fiber allows us to obtain various directions on which to project the strain field. Lim Chen Ning and Sava (2016) provide a basic workflow for recovering

multicomponent DAS data using strain projections acquired with dual optical fibers or with a single chirping (variable pitch angle) helical optical fiber. The pitch angle is the complement of the angle between the tangent vector and the axial direction of the DAS cable. The dual optical fibers configuration deploys two helical optical fiber of different constant pitch angle. This configuration is necessary to obtain sufficient projections for the strain tensor reconstruction. Similarly, Lim Chen Ning and Sava (2016) demonstrate the possibility of full strain tensor reconstruction using one optical fiber with a chirping helix geometry, which provides a broad range of strain projections, albeit at the expense of a complex design. The underlying principle of their method of strain tensor reconstruction is to group consecutive strain measurements along optical fiber(s) within a defined window larger than a gauge length. Despite successfully reconstructing the entire strain tensor, the drawback of this method is the assumption that the seismic wavelength is significantly larger than the defined analysis window. This assumption leads to a strain tensor which is assumed to be invariant within the window. Therefore, the method proposed by Lim Chen Ning and Sava (2016) could not be easily used for acquisition of short seismic wavelengths such as microseismic.

To overcome the limitation of the workflow introduced by Lim Chen Ning and Sava (2016), we propose a configuration with five equally spaced constant pitch angle helical optical fibers and a straight optical fiber. Although we use an increased number of optical fibers, we can obtain six different strain projections at every location and avoid the need to group consecutive strain measurements at different location along optical fiber(s) to get sufficient strain projections for the reconstruction. We thus obtain six different strain projections at every location and reconstruct the full strain tensor without the need to assume invariance in a wide window. The configuration reduces the engineering complexity required to build a multi-fiber cable, and also allows us to systematically analyze the effect of the associated design parameters (gauge length, diameter and pitch angle of the helical optical fibers) on the strain tensor reconstruction. We capture the gauge length in the reconstruction process, which allows us to remove its averaging effect and reconstruct strain data similar to multi-

component geophone point measurements. We note, however, that our method provides the entire strain tensor, in contrast to geophone measurements which provide the displacement vector.

We demonstrate a systematic way to choose the helical optical fiber design parameters (diameter and pitch angle) and the gauge length characterizing our system by analyzing the condition number associated with the geometry our configuration. Using the chosen parameters, we show the reconstruction of the full strain tensor through 3D synthetic examples of arbitrarily complex seismic wavefields.

3.2 Theory

The axial strain acquired by DAS captures different projections of the surrounding strain tensor as a function of the location and geometry of the optical fiber. We use the intrinsic coordinate system of a curve as described by Lin and Pisano (1988) to express the local coordinate system of the optical fiber with respect to a global coordinate system. We use the tangent vector along the optical fiber to relate the axial strain measurement with the surrounding strain tensor. The relationship between the axial strain and the surrounding strain tensor is given through the coordinate transformation relationship (Young and Budynas, 2002)

$$\bar{\boldsymbol{\varepsilon}} = \mathbf{R}\boldsymbol{\varepsilon}\mathbf{R}^T \,, \tag{3.1}$$

where $\bar{\boldsymbol{\varepsilon}}$ and $\mathbf{R}$ denote the transformed strain tensor and the transformation (also known as rotation) matrix, respectively. As derived in Appendix 3.7.1, we rearrange equation 3.1 as

$$\mathbf{p} = \mathbf{G}\mathbf{m} \,, \tag{3.2}$$

where $\mathbf{p}$ and $\mathbf{m}$ are the transformed and original strain tensors respectively in vector form. The matrix $\mathbf{G}$ is the expansion of equation 3.3 using the transformation matrix $\mathbf{R}$ and contains all the geometric information about the optical fiber. For a single optical fiber, we have infinitely many strain projections along the optical fiber, where every projection being characterized by equation 3.2. To fully describe the DAS measurements $\mathbf{d}$, we use

equation 3.2 and account for the axial strain averaging effect due to the gauge length as

$$\mathbf{d} = \mathbf{WAGm}\ , \tag{3.3}$$

where $\mathbf{A}$ is a convolution operator describing strain averaging within a gauge-length, and $\mathbf{W}$ is a windowing operator that defines the channel spacing which refers to the distance between consecutive average strain measurements within a gauge length. The graphical representation of equation 3.3 is

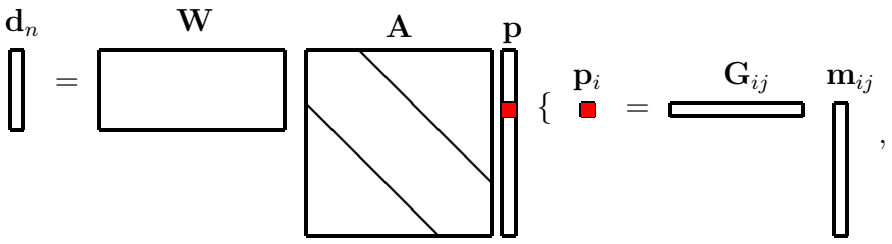

where indices i, j, and n represent samples along the optical fiber, components of the strain tensor, and measurements of a DAS system, respectively. Every sample i along the optical fiber is an element in the projection vector $\mathbf{p}$. Using the band matrix that describes the convolution operator $\mathbf{A}$, we capture the gauge length effect of the DAS system. In order to replicate a typical DAS system measurement, we apply a windowing operator $\mathbf{W}$ to determine the channel spacing between average strain measurements, usually equal to the gauge length. We represent the cascading operators $\mathbf{WAG}$ as a single linear operator $\mathbf{L}$. If we obtain sufficient strain projections to describe the surrounding strain tensor, we can reconstruct the strain tensor $\mathbf{m}$ in a least-squares sense as

$$\mathbf{m} = (\mathbf{L^T L})^{-1}\mathbf{L^T d}\ . \tag{3.4}$$

To achieve accurate reconstruction using equation 3.4, the Gram matrix $\mathbf{L^T L}$ has to be invertible, i.e., it has to be full rank, which means that all rows and as columns of the matrix must be linearly independent. The accuracy of the inverse matrix calculation is inferred from its condition number obtained as the ratio of the largest to the smallest singular values. If the condition number is large, then the matrix is ill-conditioned, implying the computation of its inverse tends to be spurious. However, a matrix with low condition number, has an

inverse that can be accurately computed. Therefore, it is advantageous to use the condition number as an indicator of strain tensor reconstruction capability. This also provides us with an opportunity to analyze various optical fiber system designs, as discussed later.

Lim Chen Ning and Sava (2016) propose two configurations to obtain multiple strain projections to reconstruct the entire strain tensor. They demonstrate that two helical optical fibers of different constant pitch angles provide sufficient strain projections to accurately reconstruct the entire strain tensor. They also show that a single helical optical fiber with varying pitch angle is capable to provide adequate strain projections to reconstruct the entire strain tensor. In this reconstruction, Lim Chen Ning and Sava (2016) group n consecutive strain measurements (where $n \geqslant 6$ and possibly higher for improved SNR) along the optical fiber(s) within a defined window to obtain $\mathbf{d}$ in equation 3.4. Similarly, they group the associated linear operators $\mathbf{L}$ to form the Gram matrix. Although they demonstrate successful reconstruction, their approach has the drawback that it assumes a seismic wavelength significantly larger than the defined window for reconstruction. This drawback limits the application of this method to acquisition of long seismic wavelengths, thus reducing the resolution of seismic imaging with DAS data.

To overcome this drawback especially for applications that require short seismic wavelengths, we propose a configuration using six optical fibers to reconstruct all components of the strain tensor. Our approach is similar to the method of Lim Chen Ning and Sava (2016), as we use multiple strain projections to reconstruct the entire strain tensor using the formulation in equation 3.4. However, our configuration forms a full rank Gram matrix using measurements from individual optical fibers instead of spatially grouping consecutive measurements along a single optical fiber. Our new method allows us to reconstruct the strain tensor $\mathbf{m}$ in equation 3.4 at any given location using data $\mathbf{d}$ from individual measurements in the constituent optical fibers. The equivalent graphical representation of equation 3.3 for our proposed method

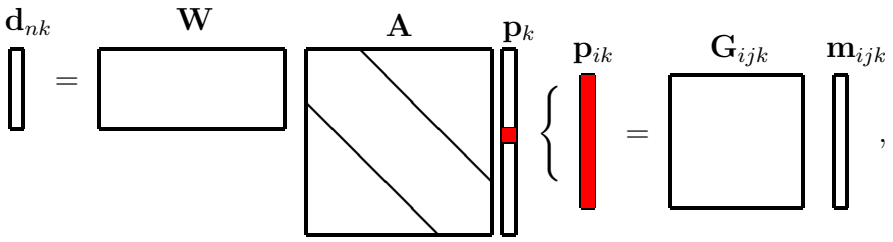

where index k denotes the number of optical fiber used for projections. Every sample i along the optical fiber k is given as an element in the projection vector $\mathbf{p}_k$. The presences of k optical fibers allow us to form the data vector $\mathbf{d}_{nk}$ and reconstruct the strain tensor $\mathbf{m}$ at a given location n. Note that the minimum requirement is to have $k = 6$ to reconstruct the six components of the strain tensor, which is similar to requirement of the method of Lim Chen Ning and Sava (2016) where they group $n \geqslant 6$ consecutive strain measurements.

We represent individual optical fibers in our proposed configuration with tangent vectors to conceptually visualize the associated measurements as shown in Figure 3.1(a) with different pitch angles from 20° to 70° at every 10°. Figure 3.1(c) demonstrates that by using the same origin for all the vectors, we obtain a right pentagonal pyramid. The geometrical implication of our configuration provides insights on the associated strain projection, as discussed later. Using the projection matrix $\mathbf{G}$ of the individual vectors, we evaluate the singular values of $\mathbf{L^T L}$ as shown in Figure 3.1(e), which indicates that our configuration is full rank, despite the fact that the smallest singular value is close to zero. A full rank Gram matrix indicates that the corresponding configuration can reconstruct the entire strain tensor. However, using multiple helical optical fibers of different pitch angles increases the engineering complexity required to assemble the optical fiber system.

In order to simplify the design, we set our configuration to five equally spaced helical optical fiber with a 20° pitch angle, together with a straight optical fiber as shown in Figure 3.1(b). Rearranging the vectors to share the same origin allows us to form a right pentagonal pyramid, as shown in Figure 3.1(d). The straight fiber makes it possible to have all nonzero singular values, as seen in Figure 3.1(f), that imply a full rank Gram matrix. This configuration uses five equally spaced helical optical fibers with constant pitch angle is

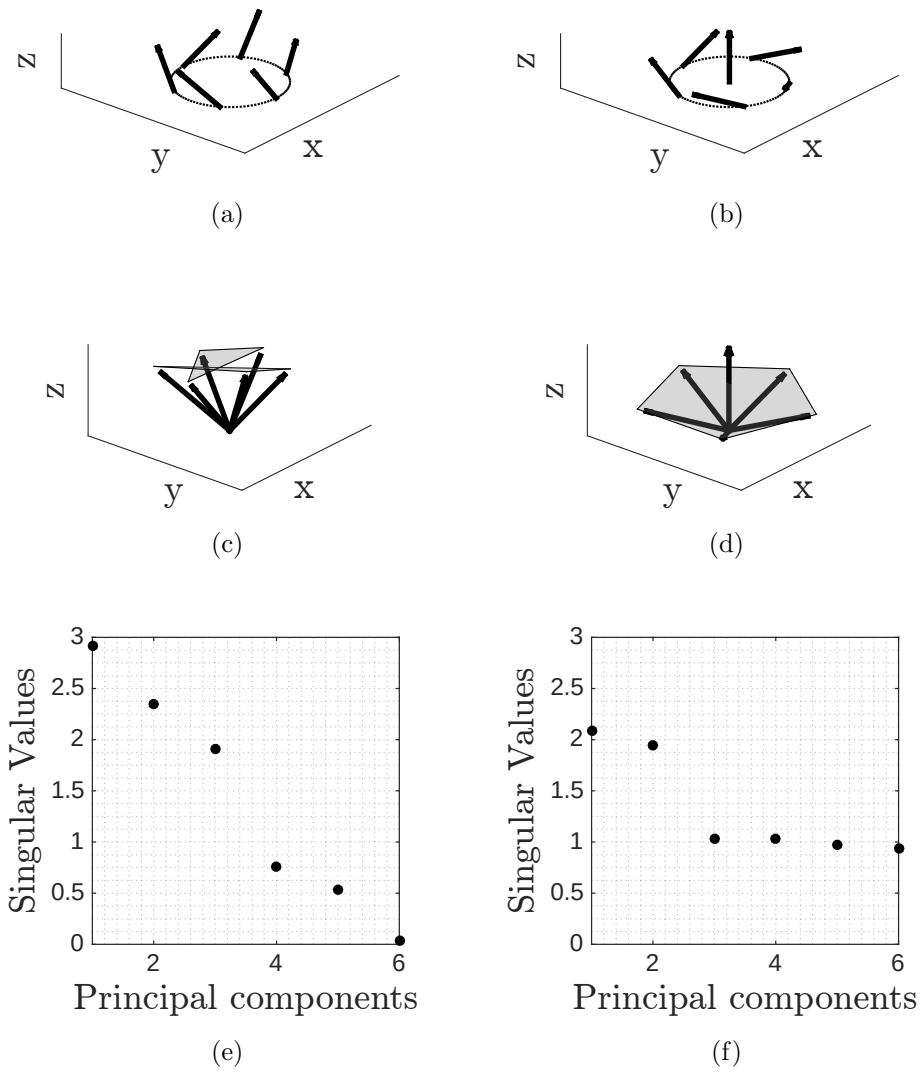

Figure 3.1: Optical fiber geometry with (a) **six** equally spaced vectors of six pitch angles (20°, 30°, 40°, 50°, 60°, and 70°), and (b) **five** equally spaced vectors of pitch angle of 20° with a straight vector in the middle. Panels (c) and (d) depict tetrahedra and right pentagonal pyramid respectively using the corresponding vectors in (a) and (b) sharing the same origin. The plots in (e) and (f) show singular values of the respective Gram matrices.

less manufacturing challenging than a sweeping helical optical fiber and allows us to obtain measurements at the same position in space along all the helical optical fibers (illustrated in Figure 3.2).

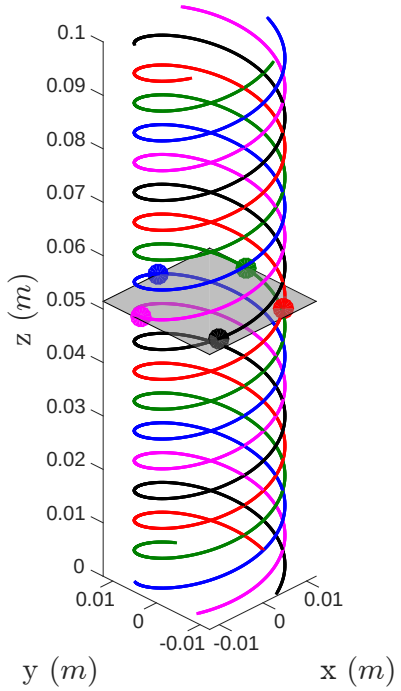

Figure 3.2: Example of five equally spaced helical optical fibers with a diameter of 2.44 cm (about 1 inch) and a pitch angle of 20°. The dots represent measurement at the same length along respective fibers which refer to the same portion of the cable indicated by the horizontal plane. The straight vertical optical fiber is not included in this plot.

Using the configuration in Figure 3.1(b) and analyzing the condition number of the corresponding Gram matrix, we search for the optimum pitch angle between 5° to 50° as shown (solid line) in Figure 3.3. The lowest condition number is around 20°; at this angle the strain projections are mainly contributed by the horizontal components. The vertical vector in our arrangement provides only vertical strain projections. This implies that to accurately reconstruct the entire strain tensor; lower pitch angles are desirable to obtain projections from horizontal strain components as seen in Figure 3.3 where the condition number of the corresponding Gram matrix increases with the pitch angle from 20°. However, we avoid low

pitch angles that are near horizontal to obtain projections from strain components between horizontal and vertical (i.e. ε_{xz} and ε_{yz}) for accurate reconstruction of the strain tensor as shown in Figure 3.3, where the condition number decreases as the pitch angle approaches 20°.

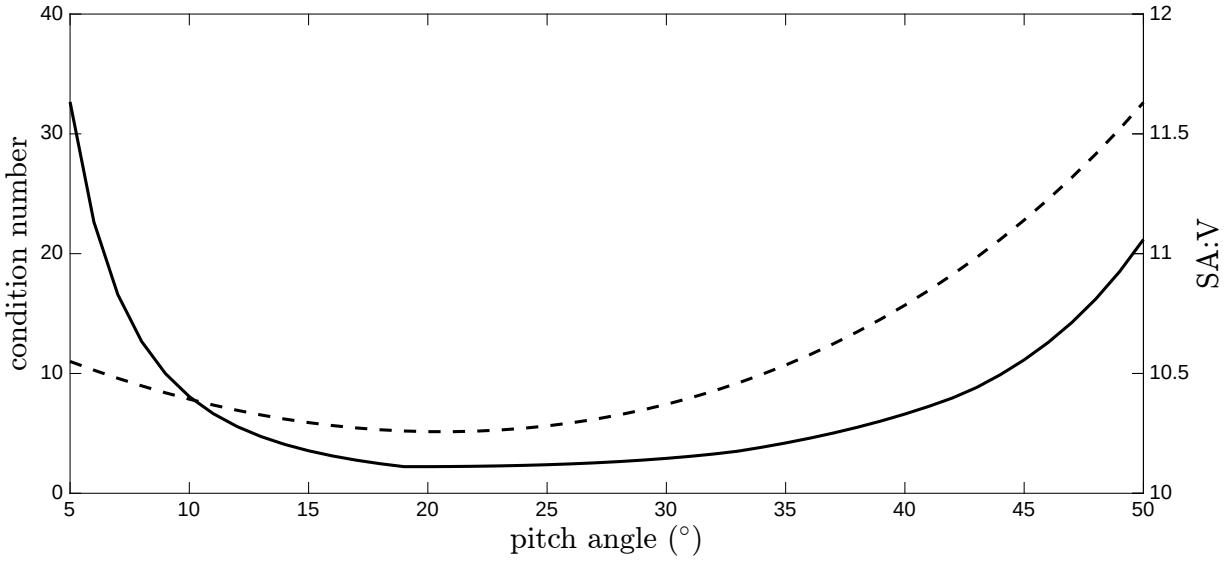

Figure 3.3: The solid line represents the condition number and the dashed line denotes the surface-area-to-volume ratio (SA:V) of a right pentagonal pyramid at different pitch angles for the five vectors in Figure 3.1(d). Both graphs share the same minimum at around 20° pitch angle.

We investigate the effects of the geometrical change in Figure 3.1(d) associated with the pitch angle of our configuration in Figure 3.1(b) on the condition number of the corresponding Gram matrix. To quantitatively assess the geometrical implication of our configuration in Figure 3.1(d) which corresponds to a right pentagonal pyramid, we can calculate the surface-area-to-volume ratio (SA:V) as shown (dashed line) in Figure 3.3. SA:V provides us a measure of compactness of the geometry associated with our configuration. Figure 3.3 shows that the lowest SA:V (most compact geometry) corresponds to the pitch angle around 20°, which coincides with the lowest condition number of the Gram matrix associated with our configuration in Figure 3.1(b). Observing the geometry for high SA:V at 5° (Figure 3.4(a)) and 50° (Figure 3.4(c)), we can infer that the geometries that are flat or elongated do

not provide a low condition numbers and thus do not lead to robust strain reconstruction. However, Figure 3.4(b) reveals a compact geometry with low SA:V that can provide sufficient projections to describe the surrounding strain tensor for full and accurate reconstruction.

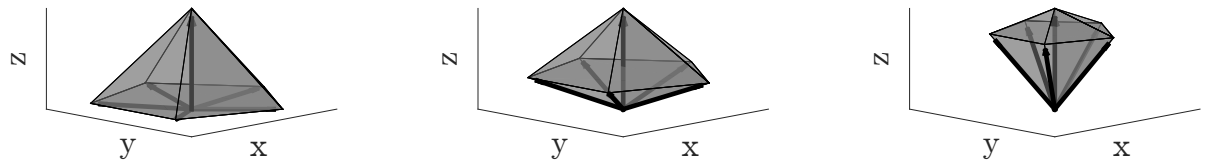

(a) (b) (c)

Figure 3.4: Two-pentagonal pyramid using five vectors with pitch angles of (a) **5°**, (b) **20°**, and (c) **50°**. The three pyramids show the visual relationship between the enclosed surface area and volume.

We investigate the effects of the gauge length on the Gram matrix by considering single measurements as shown (dots) in Figure 3.2. The azimuthal variation of the five equally spaced optical fibers does not affect the Gram matrix as the spacing between measurements are invariant as a function of position along the optical fiber. Using the condition number of the Gram matrix, we can systematically obtain the optimum design parameters (gauge length, diameter and pitch angle of the helical optical fibers) associated with low condition numbers as shown in Figure 3.5 (the colors represent the logarithm of condition number). We can scan pitch angles from 15° to 35° and diameters of the helical optical cable from 0.01 to 0.03 m, for specific gauge lengths of 0.2, 0.4, 0.6, 0.8, and 1.0 m.

The strain measurement by the DAS system using a helical geometry undergoes strain averaging in the azimuthal direction along the optical fiber within a gauge length. When the gauge length is equal to a multiple of the helix lead (the axial advance of a helix for a complete 360° turn), the DAS measurement does not contain azimuthal information, which translates into an undeniable high condition number in Figure 3.5. If we increase the gauge length for the same diameter and pitch angle (fixed helical optical fiber design parameters), the condition number is increasingly oscillatory, as shown in Figure 3.5. The DAS measure-

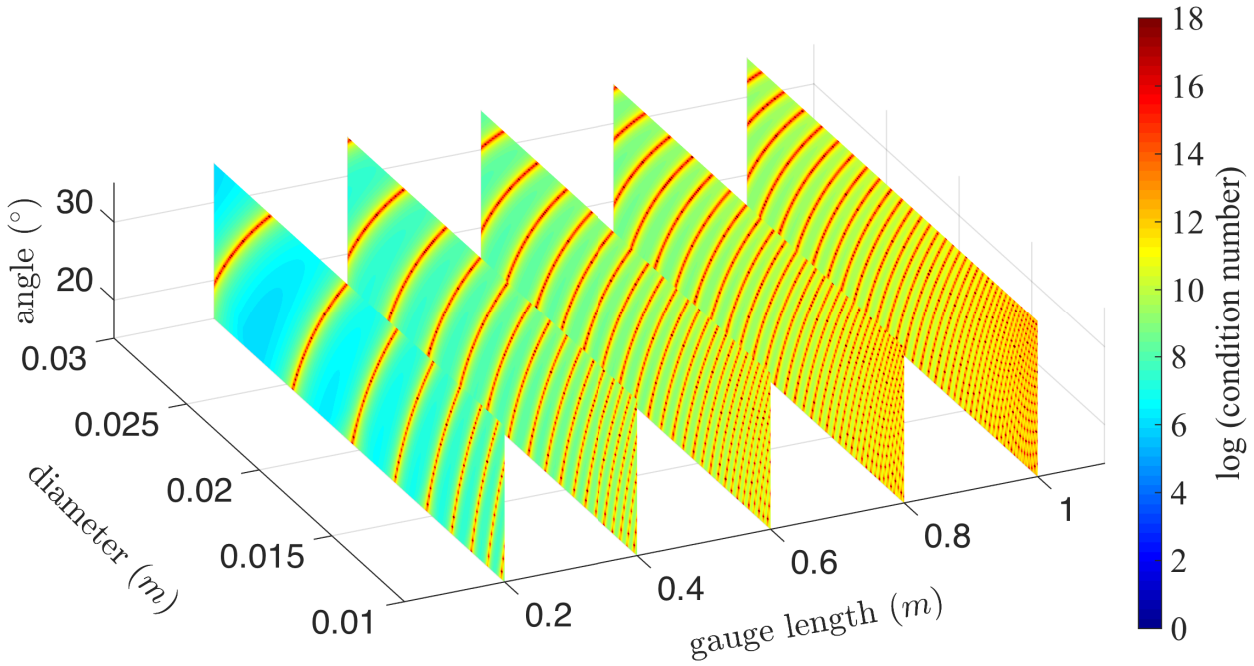

Figure 3.5: Condition number of the Gram matrix for pitch angle from 15° to 35° and diameter from 0.01 to 0.03 m. These slices are specifically scanned for but not limited to gauge lengths of 0.2, 0.4, 0.6, 0.8, and 1.0 m.

ment undergoes further azimuthal averaging within a longer gauge length, thus reducing the ability to accurately reconstruct the entire strain tensor. As we decrease the diameter of the helical optical fibers, the oscillations increase in frequency, which is also a result of increased azimuthal averaging. An informed reduction of the design parameters using the condition number ensures a high reconstruction accuracy.

In cases such as a borehole where dimensions (e.g. the diameter) are often limited, we can perform a two-dimensional parameter scan with one of the parameters fixed. In this paper, we show numerical examples of reconstructing the strain tensor using our new approach for identifying optimum parameters for a borehole environment, and we set the diameter of the optical fiber system at 2.44 cm (about 1 inch).

3.3 Numerical examples

Using numerical simulations, we reconstruct the entire 3D strain tensor with the parametrization analysis in a borehole scenario. In the following examples, we limit the dimensions of the helical optical fibers to a diameter of 2.44 cm (about 1 inch) and a pitch angle of 20° as shown in Figure 3.2. By constraining the design parameters for the helical optical fibers, we can search for an optimum gauge length using the condition number of the Gram matrix as shown in Figure 3.6(a). In our example, we scan between 0.05 and 1.10 m; we observe that there are several local minima corresponding to low condition number throughout Figure 3.6(a). The corresponding gauge lengths at these local minima are optimal (i.e. higher accuracy) for strain tensor reconstruction. The oscillating characteristic of the condition number in Figure 3.6(a) shows that the gauge length has to be reduced systematically to ensure a low condition number for high reconstruction accuracy. We illustrate our following examples with gauge lengths of 0.1, 0.5, and 1.0 m, as shown (stars) in Figure 3.6(a). We choose the gauge length of 0.5 m that does not lie at a local minimum to demonstrate that the strain tensor reconstruct of a smaller gauge length may not necessary be superior to a larger gauge length. This phenomenon is shown through a similar level of reconstruction accuracy in Figure 3.9(c) (gauge length of 0.5 m) and Figure 3.9(e) (gauge length of 1.0 m). If dimension is not a constraint, we can perform similar parameter scan for a range of diameter by limiting the pitch angle and gauge length as shown in Figure 3.6(b) for diameter between 0.01 to 0.03 m using 20° pitch angle and gauge length of 0.1 m.

Using synthetic examples of a complex wavefield, we illustrate the reconstruction of the three dimensional strain tensor from axial strain measurements along the proposed optical fiber geometry using different gauge lengths. We simulate using elastic finite-difference modeling a complex wavefield with triplications (Figure 3.7(d)) caused by a velocity model containing a low-velocity Gaussian anomaly, as shown in Figure 5.10(a). We use smaller than usual gauge lengths such as 0.1 and 0.5 m, which are possible using specially designed optical fibers, as indicated by Farhadiroushan et al. (2016). However, we also perform the

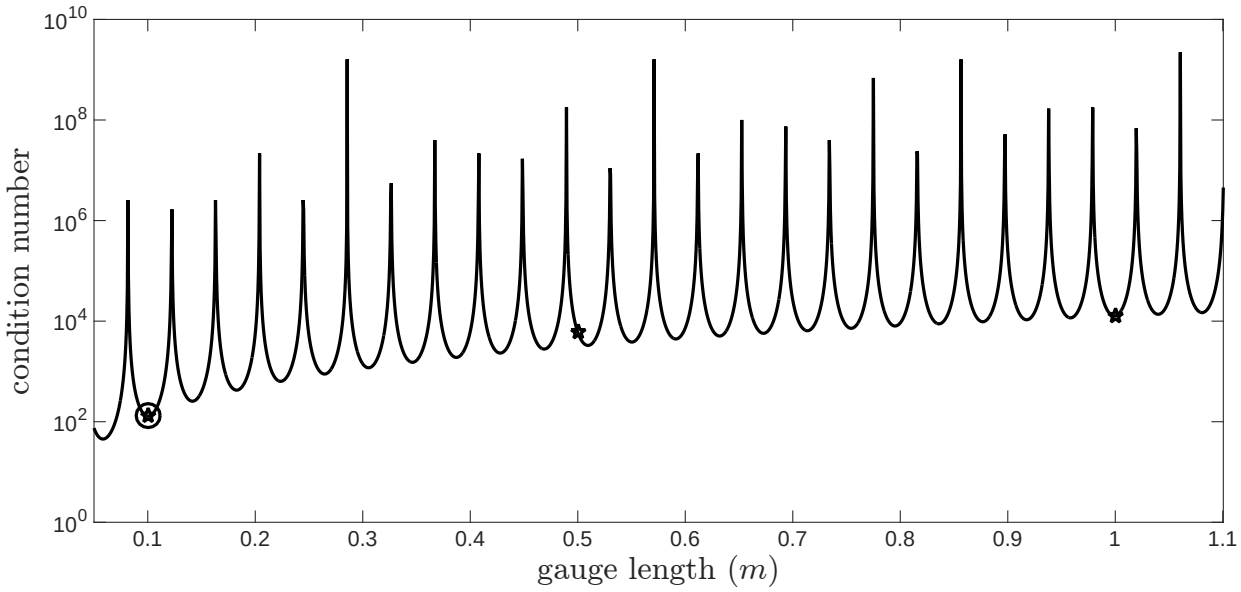

(a)

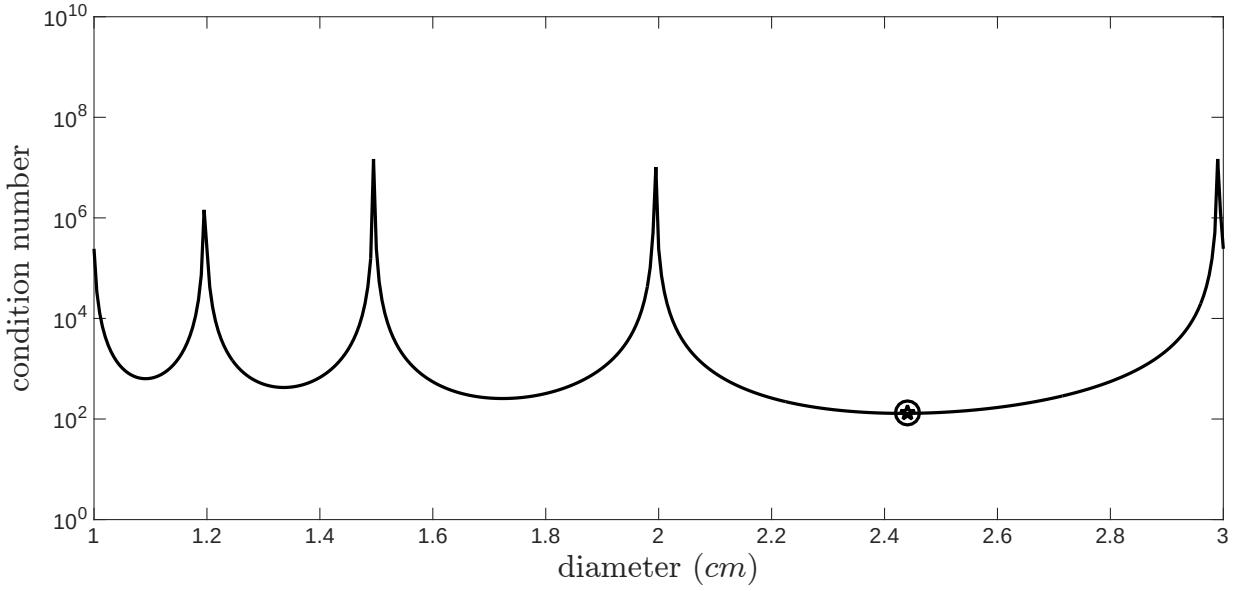

(b)

Figure 3.6: (a) The plot shows a 1D parameter scan for the intersection between diameter of 2.44 cm (about 1 inch) and 20° pitch angle of Figure 3.5. The stars mark the condition number for gauge lengths of 0.1, 0.5, and 1.0 m. (b) The plot shows diameter parameter scan by the fixing pitch angle at 20° and the gauge length at 0.1 m. The star marks the location at diameter of 2.44 cm (about 1 inch). The star with circle indicates the same combinations of parameters for both panels.

analysis using a gauge length of 1.0 m to show the effect of a more conventional fiber system.

Our experiment setup with a source indicated by a dot and receivers indicated by a straight line of coordinates (x_b, y_b) is shown in Figure 3.7(a). Figure 3.7(b), shown in a strain tensor matrix layout, represents our target strain tensor reconstruction observed along the receiver location at (x_b, y_b). The horizontal and vertical axes of the individual panels represent the reconstructed measurements along the optical fiber and time respectively. Using a gauge length of 0.1 m, we can reconstruct the strain tensor as shown in Figure 3.8(a). The difference plot between the observed and reconstructed strain tensor amplified 10 times is shown in Figure 3.8(b). We measure reconstruction quality with the residual sum of squares normalized as

$$\eta = \frac{\left\|\mathbf{m}^{obs} - \mathbf{m}^{rec}\right\|^2}{\left\|\mathbf{m}^{obs}\right\|^2} 100 \ , \tag{3.5}$$

where $\mathbf{m}^{obs}$ represents the observed strain tensor and $\mathbf{m}^{rec}$ represents the reconstructed strain tensor. The scalar values for η using a gauge length of 0.1 m are less than $10^{-4}\%$. Figure 3.8(c) shows the reconstructed strain tensor using the same configuration, but with the gauge length at 0.5 m. The differences in Figure 3.8(d) (also amplified 10 times) suggest that the increase of gauge length has minimal impact on our reconstruction. Although the calculated values for η increase overall with the larger gauge length, the highest η is less than $10^{-2}\%$, which is still a very high level of accuracy for practical applications. Figure 3.8(e) shows the results of performing the same reconstruction using a gauge length of 1.0 m. Although we can observe some minor differences in Figure 3.8(f) (also amplified 10 times), the highest η is less than $10^{-2}\%$ which is lower than the accuracy we get when we use a gauge length of 0.5 m. This result indicates that reducing the gauge length does not necessary improve the reconstruction accuracy; it moreover shows that careful analysis (as presented in Figure 3.6(a)) of the optical fiber parameters is needed for accurate reconstruction. It is worth noting that the parameter combination using gauge length of 0.5 m is not optimal as

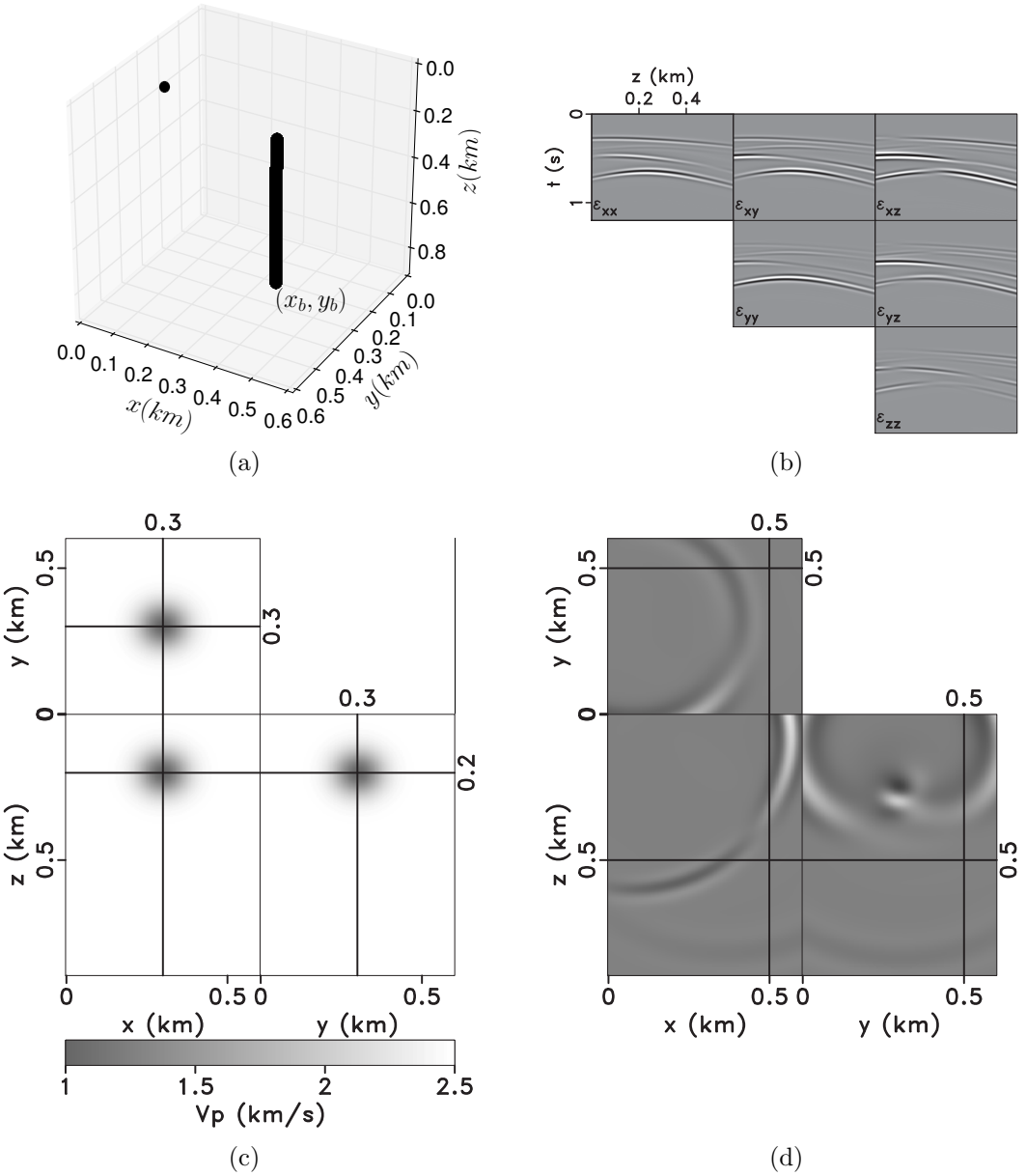

Figure 3.7: (a) Schematic representation of a DAS experiment depicting the source (dot) and receiver (line) locations. (b) The ideal strain tensor that we would like to reconstruct from DAS measurements. (c) The P-wave velocity model containing a low velocity Gaussian anomaly designed to produce wavefield triplications. The S-wave velocity is half of the P-wave velocity. (d) A snapshot of the vertical displacement wavefield.

it does not reside at a local minimum. Such combination of parameters leads to less robust reconstruction under the presence of noise, as shown in Figure 3.9(c). Diverging further from the local minimum, i.e., shifting the point for gauge length of 0.5 m as in Figure 3.6(a) to the upward-left, increases the noise level in the reconstructed strain tensor tremendously.

Since the strain tensor reconstruction for the gauge lengths of 0.1, 0.5, and 1.0 m is successful without noise, we repeat the process by adding random noise with amplitude up to 30% of the data maximum amplitude (i.e. strain projections) and in the data frequency band. In places where the signals are weak, the noise overwhelms the signal. Using a gauge length of 0.1 m, the reconstruction shown in Figure 3.9(a) is a success. The difference plot in Figure 3.9(b) shows primarily random noise. Figure 3.9(c) shows the reconstruction results by increasing the gauge length to 0.5 m. We observe stronger arrivals although the results are noisy. The difference plot shown in Figure 3.9(d) contains primarily noise. Figure 3.9(e) shows the reconstruction using a gauge length of 1.0 m, and it shows a similar result compared to the gauge length of 0.5 m. The same observation applies to the difference plot in Figure 3.9(f). The comparable quality of reconstruction between gauge length of 0.5 and 1.0 m shows that reducing gauge length significantly (half in this case) does not necessarily lead to improved reconstruction quality.

3.4 Discussion

We demonstrate full strain tensor reconstruction with a high level of accuracy using six optical fibers (five equally spaced helical optical fiber with a pitch angle of 20° and a straight optical fiber). Our results under the presence of noise show the importance of design parameters using the condition number, as reducing the gauge length does not guarantee improvements in reconstruction. However, small but achievable gauge length with low condition number such as 0.1 m provides a robust strain tensor reconstruction due to the low condition number of the Gram matrix. A larger diameter of the helical configuration allows for a larger gauge length which improves the reconstruction results in noisier environments. A relaxed diameter dimension would be more desirable in applications such as in a surface

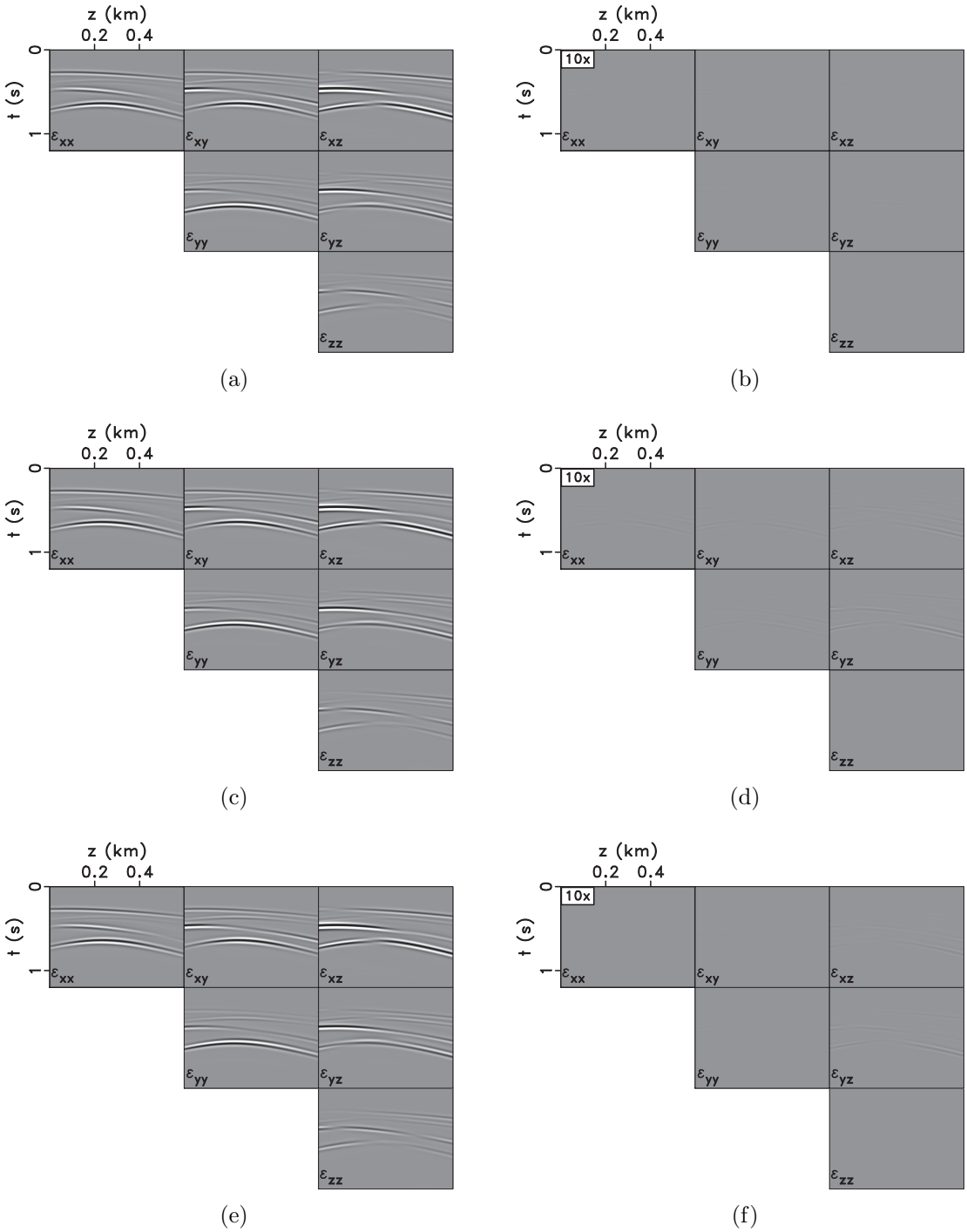

Figure 3.8: Strain tensor reconstructed with five equally spaced helical optical fibers and a straight optical fiber using a gauge length of (a) 0.1 m, (c) 0.5 m, and (e)1.0 m. (b), (d), and (f) are the difference between the ideal strain tensor in Figure 3.7(b) and the respective reconstructed tensor in (a), (c), and (e) magnified 10 times.

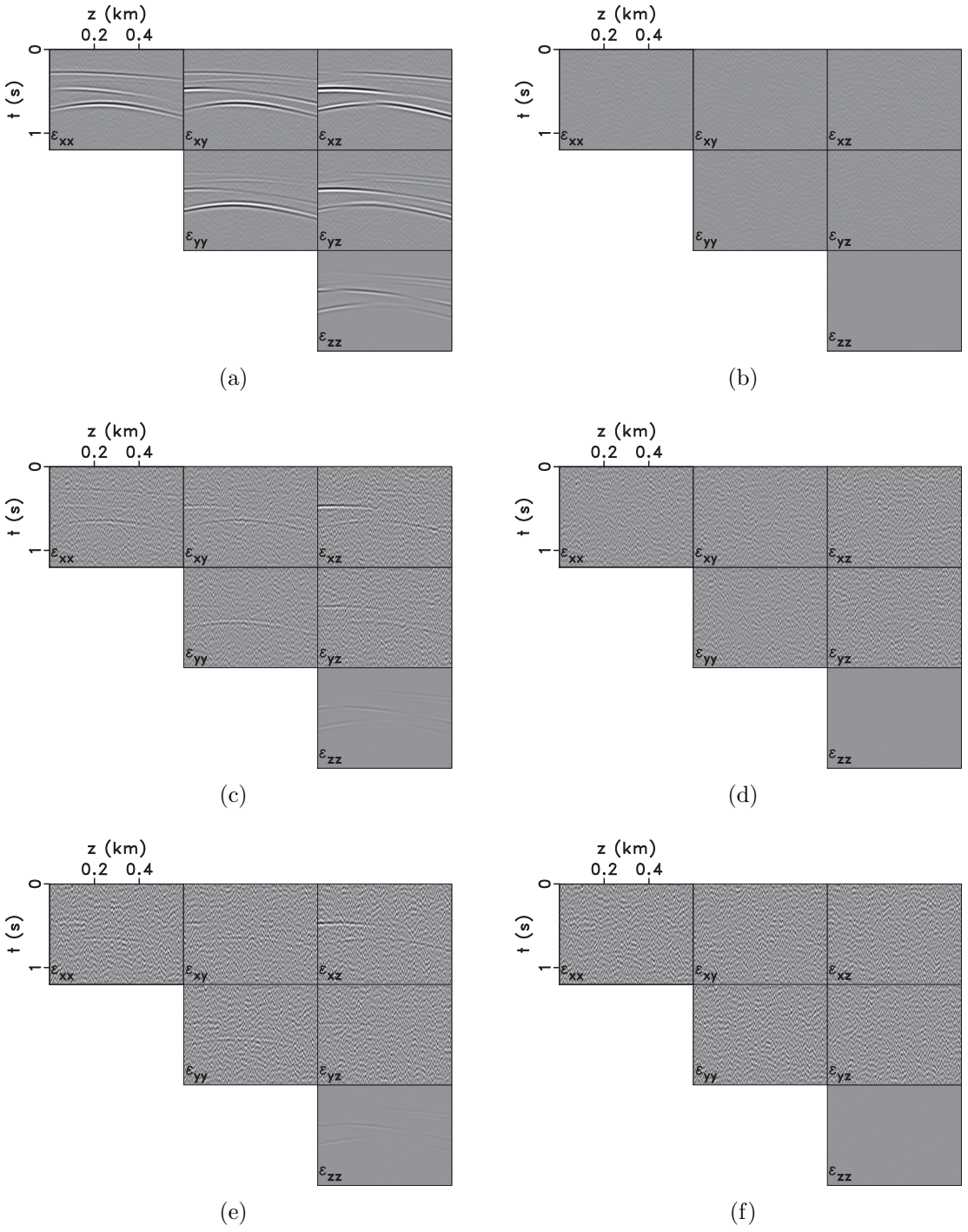

Figure 3.9: Strain tensor reconstructed from data containing random noise with 30% of the maximum data amplitude and band-limited to the data band with five equally spaced helical optical fibers and a straight optical fiber using a gauge length of (a) 0.1 m, (c) 0.5 m, and (e) 1.0 m. (b), (d), and (f) are the difference between the ideal strain tensor in Figure 3.7(b) and the respective reconstructed tensor in (a), (c) and (e).

seismic acquisition.

Using our proposed configuration, we can analyze the design parameters for the helical optical fibers systematically. Scanning can be done in a general manner as shown in Figure 3.5 or under certain constraints (diameter or pitch angle of the helical optical fiber) as shown in Figure 3.6(a). The design goal is to obtain parameters that have the lowest possible condition number of the Gram matrix $\mathbf{G^T A^T A G}$ calculated from the averaging $\mathbf{A}$ and projection $\mathbf{G}$ matrices, while also satisfying engineering constraints for optical fiber construction. Numerous configuration of equivalent robustness and quality are possible. In the presence of optical fiber geometry uncertainty, we can use a weighting operator in the reconstruction process or the shape-sensing method (Moore and Rogge, 2012), as discussed in our previous paper (Lim Chen Ning and Sava, 2016) to improve our reconstruction results.

3.5 Conclusions

We demonstrate that high resolution multicomponent distributed acoustic sensing data is achievable by using strain projections along several optical fibers to reconstruct all components of the 3D strain tensor. Five equally spaced helical optical fibers, together with a straight optical fiber can be used for reconstruction without assuming that strain changes slowly along the fiber, as shown by Lim Chen Ning and Sava (2016). We thus overcome the requirement that the seismic wavelength be significantly larger than the window, and achieve multicomponent strain reconstruction with high spatial resolution. This method opens the possibility for acquisition of shorter seismic wavelengths, which aids imaging and reservoir characterization applications. Numerical examples show that our method can reconstruct the full 3D strain tensor for wavefields of arbitrary complexity, and in the presence of strong noise in the band of the seismic data.

3.6 Acknowledgments

We would like to thank the sponsors of the Center for Wave Phenomena, whose support made this research possible and Martin Karrenbach of OptaSense for fruitful discussions.

The reproducible numeric examples in this paper use the Madagascar open-source software package (Fomel et al., 2013) freely available from http://www.ahay.org.

3.7 Appendix

This appendix describes the strain projection along the optical fiber.

3.7.1 Strain Projection

The strain projection measurement of the surrounding strain tensor along the optical fiber can be expressed through coordinate transformation as (Young and Budynas, 2002)

$$\bar{\boldsymbol{\varepsilon}} = \mathbf{R}\boldsymbol{\varepsilon}\mathbf{R}^{\mathbf{T}} \,, \tag{3.6}$$

where $\bar{\boldsymbol{\varepsilon}}$ and $\boldsymbol{\varepsilon}$ denote the strain tensors in the new and original coordinate systems, respectively. $\mathbf{R}$ represents the transformation (also known as rotation) matrix. Since the transformation matrix is given by the directional cosines between the intrinsic and global coordinate system, the transformation matrix can be expressed through the intrinsic coordinate system using tangent $\mathbf{t}$, normal $\mathbf{n}$ and binormal $\mathbf{b}$ unit vectors with respect to the global coordinate system as

$$\mathbf{R} = \begin{bmatrix} R_{11} & R_{12} & R_{13} \\ R_{21} & R_{22} & R_{23} \\ R_{31} & R_{32} & R_{33} \end{bmatrix} = \begin{bmatrix} t_x & t_y & t_z \\ n_x & n_y & n_z \\ b_z & b_y & b_z \end{bmatrix} \,, \tag{3.7}$$

where the rows of the transformation matrix $\mathbf{R}$ is represented by the tangent $\mathbf{t} = \{t_x, t_y, t_z\}$, normal $\mathbf{n} = \{n_x, n_y, n_z\}$ and binormal $\mathbf{b} = \{b_x, b_y, b_z\}$ unit vectors of intrinsic coordinate system. Since DAS measures axial strain along the optical fiber, it is sufficient to use the tangent vector $\mathbf{t}$ of the optical fiber to perform the axial strain tensor projection. Hence, we can narrow equation 3.6 to the rotated axial strain measurement in 3D at a location along

the optical fiber as follows

$$\begin{matrix} \mathrm{p} & & \mathrm{G} & & & & & \mathrm{m} \end{matrix}$$

$$\begin{bmatrix}\bar{\varepsilon}_t\end{bmatrix} = \begin{bmatrix} R_{11}^2 & R_{12}^2 & R_{13}^2 & 2R_{11}R_{12} & 2R_{11}R_{13} & 2R_{12}R_{13} \end{bmatrix} \begin{bmatrix} \varepsilon_{xx} \\ \varepsilon_{yy} \\ \varepsilon_{zz} \\ \varepsilon_{xy} \\ \varepsilon_{xz} \\ \varepsilon_{yz} \end{bmatrix}, \tag{3.8}$$

where the projected strain data $\mathbf{p}$ represents strain projection measurements $\bar{\varepsilon}_t$ onto the tangent vector $\mathbf{t}$. The matrix $\mathbf{G}$ represents the expanded rotation matrix from equation 3.7. $\mathbf{m}$ is the vectorized strain tensor $\boldsymbol{\varepsilon} = \{\varepsilon_{xx}, \varepsilon_{yy}, \varepsilon_{zz}, \varepsilon_{xy}, \varepsilon_{xz}, \varepsilon_{yz}\}$ on the original coordinate system.

CHAPTER 4

SEISMIC SOURCE MECHANISM IMAGING

To be submitted to *Geophysical Prospecting*

Ivan Lim Chen Ning[1,2,3] and Paul Sava[1]

Wavefield-based solutions are robust and facilitate straightforward seismic source parameter estimation. The potential to access multicomponent stress and particle displacement data through new technology such as distributed acoustic sensing (DAS) allows us to formulate the source mechanism imaging problem using full anisotropic elastic wavefields. We propose a method that enables us to obtain the source location and mechanism simultaneously, without the need for lengthy iterative inversion. Our technique requires knowledge of the medium model parameters (also a requirement for any other wavefield-based method) for reverse-time wavefield extrapolation, and the source wavelet (which can be reasonably well estimated) for the imaging condition. The source location and mechanism are inherent products of our imaging process. For high-resolution imaging, least-squares solutions diminish artifacts due to limited receiver coverage and illumination. We validate our approach using multiple 3D numerical experiments with various combinations of source mechanisms, demonstrating its capability to recover accurate source parameters.

4.1 Introduction

Seismic source imaging is widely used in seismology, especially for earthquake and microseismic monitoring and characterization. The source parameters such as location, excitation

[1]Graduate student and Professor, respectively, Center for Wave Phenomena, Colorado School of Mines, 1500 Illinois St., Golden, CO 80401, USA
[2]Primary researcher and author
[3]Author for correspondence

time, and focal mechanism are of great interest as they provide information about reservoirs subject to hydraulic fracturing (Baig and Urbancic, 2010). The source information also allows us to quantify the extent (width and distance) of the induced fractures. Through the source mechanism, we can infer the fracture orientation that enables timely strategic decisions for borehole placement to improve reservoir production (Maxwell et al., 2010).

The source parameters can be obtained through waveform tomography for simultaneous multi-source parameter inversion based on the amplitude and phase information of the recorded data. Waveform tomography utilizes adjoint wavefields simulated by reverse time extrapolation (Tromp et al., 2005; Kim et al., 2011; Jarillo Michel and Tsvankin, 2014, 2015, 2017). Alternatively, one can use reverse-time imaging for source location (Artman et al., 2010; Li et al., 2017), or can adopt optimization-based source imaging for reduced truncation artifacts and higher resolution (Fukahata et al., 2013; Bazargani and Snieder, 2015; Nakahara and Haney, 2015). Kawakatsu and Montagner (2008) as well as Gharti et al. (2011) outline the theory of reverse time imaging to provide an approximate estimate of the seismic source mechanism by conventional amplitude-based inversions, i.e., using the Greens functions. Similarly, Montagner et al. (2012) demonstrate the use of reverse time wavefields to retrieve the source mechanism (moment tensor) from long period waves. Aside from wavefield-based imaging methods, Chambers et al. (2014) investigate the use of diffraction stacking to obtain the source mechanism through imaging.

In this paper, we propose to use reverse-time wavefield extrapolation to obtain the seismic source mechanism through imaging without the need for lengthy iterative inversion. Our method requires both stress and particle displacement data to reconstruct accurately subsurface wavefields in heterogeneous and anisotropic media. Although stress data are not commonly acquired, we frame our method in the context of new acquisition technologies such as distributed acoustic sensing (DAS) that measures strain along optical fibers. We can obtain multicomponent DAS strain measurements using novel optical fiber configurations (Lim Chen Ning and Sava, 2016, 2018b, 2017). Assuming knowledge of the Earth's material

properties surrounding the optical fiber, we can compute stress from strain via conventional constitutive relations (Aki and Richards, 2002). Without loss of generality, we can formulate our imaging approach with either stress or particle displacement data as special cases. The source image contains information about its source location and mechanism.

We demonstrate the proposed imaging process using 3D numerical simulations that mimic passive seismic experiments. We test our algorithm with multiple source mechanism consisting of moment tensor or body force sources. The tested acquisition geometry includes both spherical receiver distributions for full aperture analysis, as well as surface receivers to emulate practical microseismic observation arrays.

4.2 Theory

We describe elastic-wave propagation using the second-order partial differential equations in space $\mathbf{x}$ and time t consisting both stress tensor $\underline{\mathbf{t}}(\mathbf{x},t)$ and particle displacement vector $\mathbf{u}(\mathbf{x},t)$ wavefields (Aki and Richards, 2002)

$$\rho \frac{\partial^2 \mathbf{u}}{\partial t^2} = \mathbf{D}\,\underline{\mathbf{t}} + \mathbf{f}\,, \tag{4.1}$$

where $\mathbf{D}$ represents the divergence operator. $\rho(\mathbf{x})$ is the density and $\mathbf{f}(\mathbf{x},t)$ is the external volume force. Under the assumption of linear elasticity the stress $\underline{\mathbf{t}}(\mathbf{x},t)$ is related to strain $\underline{\mathbf{e}}(\mathbf{x},t)$ through the constitutive relation

$$\underline{\mathbf{t}} = \underline{\underline{\mathbf{c}}}\,\underline{\mathbf{e}} + \underline{\mathbf{m}}\,, \tag{4.2}$$

where $\underline{\underline{\mathbf{c}}}(\mathbf{x})$ is the stiffness tensor and $\underline{\mathbf{m}}(\mathbf{x},t)$ is the seismic moment tensor source acting as stress perturbation. The relation between the strain $\underline{\mathbf{e}}(\mathbf{x},t)$ tensor and particle displacement $\mathbf{u}(\mathbf{x},t)$ is

$$\begin{aligned} \underline{\mathbf{e}} &= \frac{1}{2}\left[\,\nabla\mathbf{u} + (\nabla\mathbf{u})^{\intercal}\,\right] \\ &= \mathbf{H}\,\mathbf{u}\,, \end{aligned} \tag{4.3}$$

where the operator $\mathbf{H}$ captures the geometric relation between strain and particle displacement. We express the seismic moment tensor source as

$$\underline{\mathbf{m}} = \mathrm{s}^{\mathbf{m}}\,\mathbf{M}\,, \tag{4.4}$$

where $\mathbf{M}(\mathbf{x})$ is a unitless matrix that determines the magnitude of the moment tensor source. $\mathrm{s}^{\mathbf{m}}(t)$ denotes the moment tensor source wavelet with units of stress (force per unit area). Similarly, we express the body force vector as

$$\mathbf{f} = \mathrm{s}^{\mathbf{f}}\,\mathbf{F}\,, \tag{4.5}$$

where $\mathbf{F}(\mathbf{x})$ is a unitless vector that determines the magnitude of the body force source. $\mathrm{s}^{\mathbf{f}}(t)$ represents the body force source wavelet with units of force density (force per unit volume). We can interpret $\mathbf{M}(\mathbf{x})$ and $\mathbf{F}(\mathbf{x})$ as images that show the source location and its associated mechanism. Following the notations in equations 4.4 and 4.5, we can define the moment tensor source term in matrix form as

$$\begin{bmatrix} \underline{\mathbf{m}}_0 \\ \underline{\mathbf{m}}_1 \\ \underline{\mathbf{m}}_2 \\ \vdots \end{bmatrix} = \begin{bmatrix} \mathrm{s}_0^{\mathbf{m}} \\ \mathrm{s}_1^{\mathbf{m}} \\ \mathrm{s}_2^{\mathbf{m}} \\ \vdots \end{bmatrix} \Big[\mathbf{M}\Big] \tag{4.6}$$

and the corresponding body force source term as

$$\begin{bmatrix} \mathbf{f}_0 \\ \mathbf{f}_1 \\ \mathbf{f}_2 \\ \vdots \end{bmatrix} = \begin{bmatrix} \mathrm{s}_0^{\mathbf{f}} \\ \mathrm{s}_1^{\mathbf{f}} \\ \mathrm{s}_2^{\mathbf{f}} \\ \vdots \end{bmatrix} \Big[\mathbf{F}\Big]\,. \tag{4.7}$$

The images $\mathbf{M}(\mathbf{x})$ and $\mathbf{F}(\mathbf{x})$ scale the respective source wavelets to generate the external sources $\underline{\mathbf{m}}(\mathbf{x}, t)$ and $\mathbf{f}(\mathbf{x}, t)$ for wavefield extrapolation. We solve equations 4.1 and 4.2 using the finite-difference representation of the time-derivative leading to the recursive relations for stress

$$\underline{\mathbf{t}} = \underline{\underline{\mathbf{c}}}\,\mathbf{H}\,\mathbf{u} + \mathbf{M}\,\mathrm{s}^{\mathbf{m}} \tag{4.8}$$

and particle displacement

$$\mathbf{u}_+ = 2\mathbf{u} + \frac{\Delta t^2}{\rho}\left(\mathbf{D}\,\underline{\mathbf{t}} + \mathbf{F}\,\mathrm{s}^{\mathbf{f}}\right) - \mathbf{u}_- \,. \tag{4.9}$$

These recursive equations allow us to compute the subsequent time wavefield $\mathbf{u}_+$ from wavefields at the current time $\mathbf{u}$ and at preceding time $\mathbf{u}_-$. In matrix form, we express the recurrent equations 4.8 and 4.9 as

$$\left[\begin{array}{c|ccccc} \mathbf{I} & & -\underline{\underline{\mathbf{c}}}\,\mathbf{H} & & & \\ \hline & -\frac{2\rho}{\Delta t^2} & \frac{\rho}{\Delta t^2} & 0 & \cdots \\ & \frac{\rho}{\Delta t^2} & -\frac{2\rho}{\Delta t^2} & \frac{\rho}{\Delta t^2} & \cdots \\ -\mathbf{D} & 0 & \frac{\rho}{\Delta t^2} & -\frac{2\rho}{\Delta t^2} & \cdots \\ & \vdots & \vdots & \vdots & \ddots \end{array}\right] \left[\begin{array}{c} \underline{\mathbf{t}}_0 \\ \underline{\mathbf{t}}_1 \\ \underline{\mathbf{t}}_2 \\ \vdots \\ \hline \mathbf{u}_0 \\ \mathbf{u}_1 \\ \mathbf{u}_2 \\ \vdots \end{array}\right] = \left[\begin{array}{c} \underline{\underline{\mathbf{m}}}_0 \\ \underline{\underline{\mathbf{m}}}_1 \\ \underline{\underline{\mathbf{m}}}_2 \\ \vdots \\ \hline \mathbf{f}_0 \\ \mathbf{f}_1 \\ \mathbf{f}_2 \\ \vdots \end{array}\right] \tag{4.10}$$

where $\underline{\underline{\mathbf{m}}}$ and $\mathbf{f}$ are the input wavefields, i.e., the source, and $\underline{\mathbf{t}}$ and $\mathbf{u}$ are propagating wavefields. We solve for $\underline{\mathbf{t}}$ and $\mathbf{u}$ from the top, i.e., forward in time, using the moment tensor and the body force sources. The forward operator takes a wavefield $\mathbf{d} = [\,\underline{\underline{\mathbf{m}}}, \mathbf{f}\,]$ and generates a wavefield $\mathbf{w} = [\,\underline{\mathbf{t}}, \mathbf{u}\,]$ by propagating forward in time:

$$\mathbf{L}\mathbf{w} = \mathbf{d}\,. \tag{4.11}$$

The adjoint operator takes the wavefield $\mathbf{w} = [\,\underline{\mathbf{t}}, \mathbf{u}\,]$ and generates the adjoint wavefield $\mathbf{d}^* = [\,\underline{\underline{\mathbf{m}}}^*, \mathbf{f}^*\,]$ by propagating backward in time:

$$\mathbf{w} = \mathbf{L}^\dagger \mathbf{d}^*\,. \tag{4.12}$$

In matrix form, we can write equation 4.12 as

$$\left[\begin{array}{c|cccc} \mathbf{I} & -\mathbf{D}^\dagger & & & \\ \hline & -\frac{2\rho}{\Delta t^2} & \frac{\rho}{\Delta t^2} & 0 & \dots \\ -\mathbf{H}^\dagger\,\underline{\underline{\mathbf{c}}} & \frac{\rho}{\Delta t^2} & -\frac{2\rho}{\Delta t^2} & \frac{\rho}{\Delta t^2} & \dots \\ & 0 & \frac{\rho}{\Delta t^2} & -\frac{2\rho}{\Delta t^2} & \dots \\ & \vdots & \vdots & \vdots & \ddots \end{array}\right] \left[\begin{array}{c} \underline{\mathbf{m}}_0^* \\ \underline{\mathbf{m}}_1^* \\ \underline{\mathbf{m}}_2^* \\ \vdots \\ \hline \mathbf{f}_0^* \\ \mathbf{f}_1^* \\ \mathbf{f}_2^* \\ \vdots \end{array}\right] = \left[\begin{array}{c} \underline{\mathbf{t}}_0 \\ \underline{\mathbf{t}}_1 \\ \underline{\mathbf{t}}_2 \\ \vdots \\ \hline \mathbf{u}_0 \\ \mathbf{u}_1 \\ \mathbf{u}_2 \\ \vdots \end{array}\right] . \tag{4.13}$$

We solve for $\underline{\mathbf{m}}^*$ and $\mathbf{f}^*$ from the bottom, i.e., backward in time, using the sources $\underline{\mathbf{t}}$ and $\mathbf{u}$. The time reversal iterative equation for the adjoint strain is

$$\underline{\mathbf{m}}^* = \mathbf{D}^\dagger\,\mathbf{f}^* + \underline{\mathbf{t}} \tag{4.14}$$

and the adjoint particle displacement is

$$\mathbf{f}_-^* = 2\mathbf{f}^* + \frac{\Delta t^2}{\rho}\left(\mathbf{H}^\dagger\,\underline{\underline{\mathbf{c}}}\,\underline{\mathbf{m}}^* + \mathbf{u}\right) - \mathbf{f}_+^*\,, \tag{4.15}$$

where $\underline{\mathbf{m}}^*$ denotes the adjoint strain and $\mathbf{f}^*$ is the adjoint particle displacement. Finally, we obtain the respective adjoint source mechanism image using the adjoint fields as zero lag crosscorrelation with the moment tensor source wavelet

$$\left[\mathbf{M}^*\right] = \left[\,\mathrm{s}_0^{\mathbf{m}}\;\mathrm{s}_1^{\mathbf{m}}\;\mathrm{s}_2^{\mathbf{m}}\;\dots\,\right] \left[\begin{array}{c} \underline{\mathbf{m}}_0^* \\ \underline{\mathbf{m}}_1^* \\ \underline{\mathbf{m}}_2^* \\ \vdots \end{array}\right] \tag{4.16}$$

and the body force source wavelet

$$\left[\mathbf{F}^*\right] = \left[\,\mathrm{s}_0^{\mathbf{f}}\;\mathrm{s}_1^{\mathbf{f}}\;\mathrm{s}_2^{\mathbf{f}}\;\dots\,\right] \left[\begin{array}{c} \mathbf{f}_0^* \\ \mathbf{f}_1^* \\ \mathbf{f}_2^* \\ \vdots \end{array}\right] . \tag{4.17}$$

We represent the forward cascading operations in equations 4.6, 4.7 and 4.10 through forward operator

$$\mathbf{Gn} = \quad \mathbf{w} \tag{4.18}$$

and the equivalent adjoint cascading operations in equations 4.13, 4.16 and 4.17 by the adjoint operator

$$\mathbf{n} = \mathbf{G}^{\dagger}\mathbf{w}\,. \tag{4.19}$$

The forward operator $\mathbf{G}$ generates data $\mathbf{w}$ comprising of stress $\underline{\mathbf{t}}$ and particle displacement $\mathbf{u}$ from source mechanism image $\mathbf{n}$ of moment tensor $\mathbf{M}$ and body force $\mathbf{F}$ sources. The adjoint operator $\mathbf{G}^{\dagger}$ forms an image representing the source mechanism and is analogous to the gradient for the centroid-moment tensor inversion method (Kim et al., 2011). Since we formulate both the forward (equation 4.18) and adjoint (equation 4.19) operations, we can perform least-squares imaging to obtain high-resolution source mechanism images as

$$\mathbf{n} = \left(\mathbf{G}^{\dagger}\mathbf{G}\right)^{-1}\mathbf{G}^{\dagger}\mathbf{w}\,. \tag{4.20}$$

We can interpret $\mathbf{G}^{\dagger}\mathbf{G}$ as a point spread function (PSF) that blurs (via convolution) the image $\mathbf{n}$. Least-squares imaging deconvolves the PSF to generate high-resolution images. Note that we present a general formulation that includes both stress and displacement data together with both seismic source mechanisms of moment tensor and body force sources. Nonetheless, simplification such as reducing the data requirement to either stress or displacement is possible without any loss of generality. The same is true for the moment tensor and body force sources as they contain complementary information.

4.3 Numerical examples

To analyze the theoretical performance of our proposed method, we perform a passive seismic numerical simulation with full aperture geometry. This ideal coverage enables us to discount the possibility of truncation artifacts through inadequate wavefield sampling to

impair our analysis. We also show a review of our technology with a surface seismic acquisition to demonstrate the feasibility of our technique in a realistic scenario. The following examples cover reverse-time migrations and least-squares solutions. We present the source mechanism images using the tensor-vector matrix layout

$$\begin{array}{|c|c|c|} \hline \mathrm{M}_{xx} & \mathrm{M}_{xy} & \mathrm{M}_{xz} \\ \hline \mathrm{F}_{x} & \mathrm{M}_{yy} & \mathrm{M}_{yz} \\ \hline \mathrm{F}_{y} & \mathrm{F}_{z} & \mathrm{M}_{zz} \\ \hline \end{array} \quad ,$$

which combines the stress tensor (in red) in its natural matrix representation together with the particle displacement vector wavefield in a combined 3×3 plot.

We set up our perfect aperture experiment using a constant elastic model with compressional velocity of 2400 m/s, shear velocity of 1300 m/s, and density of 1000 kg/m^3. Figure 4.1(a) illustrates the acquisition geometry with the source (in red) and spherical receiver (in black), emulating a passive seismic example. Note that the receivers are nearly evenly distributed on the sphere using a Fibonacci lattice (González, 2010). Table 4.1 represents the six different combinations of source mechanisms for analysis using the same acquisition geometry. Table 4.1 shows a summary of the figures and the corresponding source mechanisms. The image consists of three different slices of the 3D cube along the principal axes centered at the source location.

Table 4.1: Summary of all the 3D source mechanism experiment.

Experiment	M_{xx}	M_{yy}	M_{zz}	M_{yz}	M_{xz}	M_{xy}	F_{x}	F_{y}	F_{z}
1	0	0	0	0	-1	0	0	0	0
2	1	1	1	0	0	0	0	0	0
3	0	0	0	0	0	0	0	0	1

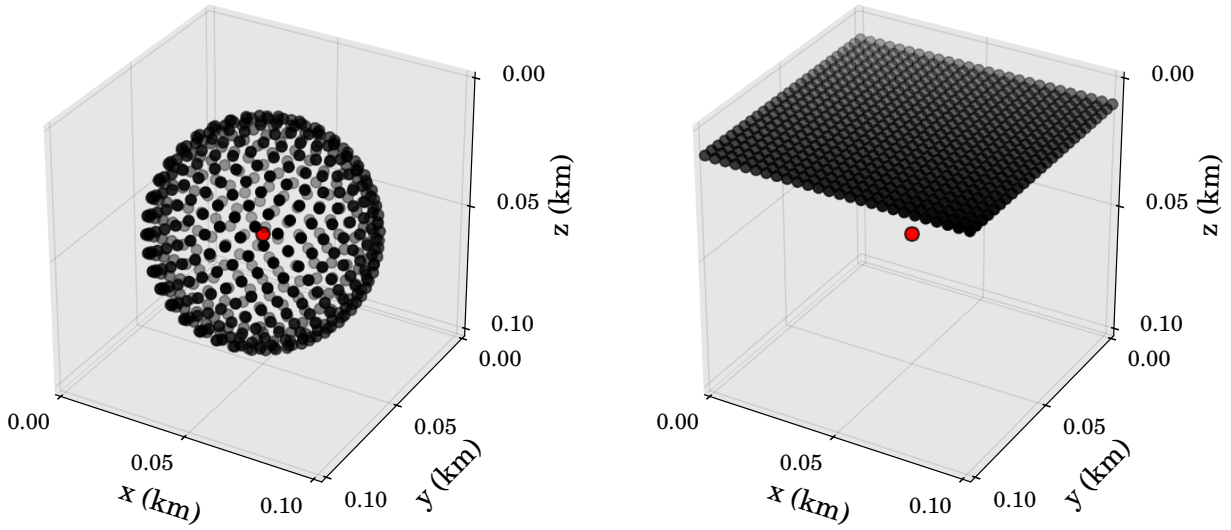

Figure 4.1: 3D microseismic experiment setup with receivers providing (a) ideal spherical coverage and (b) surface seismic acquisition. The red dot represents the source location.

The first experiment in Table 4.1 resembles a double-couple earthquake source in the xz-plane. Figure 4.2 shows nine panels that populate the moment tensor matrix $\mathbf{M}$ and the body force vector $\mathbf{F}$. We observe components of the source image that are symmetric in some axes, i.e., the image panel of F_x along the vertical axis or the image panel of F_z along the horizontal axis. However, of particular interest is the image panel of M_{xz} that is symmetric along both major axes which coincide with our exact source mechanism at $\mathrm{M}_{xz} = -1$ as the only nonzero component. The negative blue dot in panel M_{xz} shows the source location. Table 4.2 shows a summary of the image symmetry with the corresponding elements of the source mechanism. We obtain higher resolution source mechanism images through the least-squares formulation in equation 4.20. Comparing Figure 4.2 to Figure 4.3, the least-squares images are sharper and provide a more compact representation of the source image due to the removal of the PSF blurring effect. For the remaining examples, we focus on the source images from least-squares.

Table 4.2: xz-plane double-couple source mechanism and image symmetry comparison.

	M_{xx}	M_{yy}	M_{zz}	M_{yz}	M_{xz}	M_{xy}	F_x	F_y	F_z
symmetry	no	no	no	no	yes	no	no	no	no
values	0	0	0	0	-1	0	0	0	0

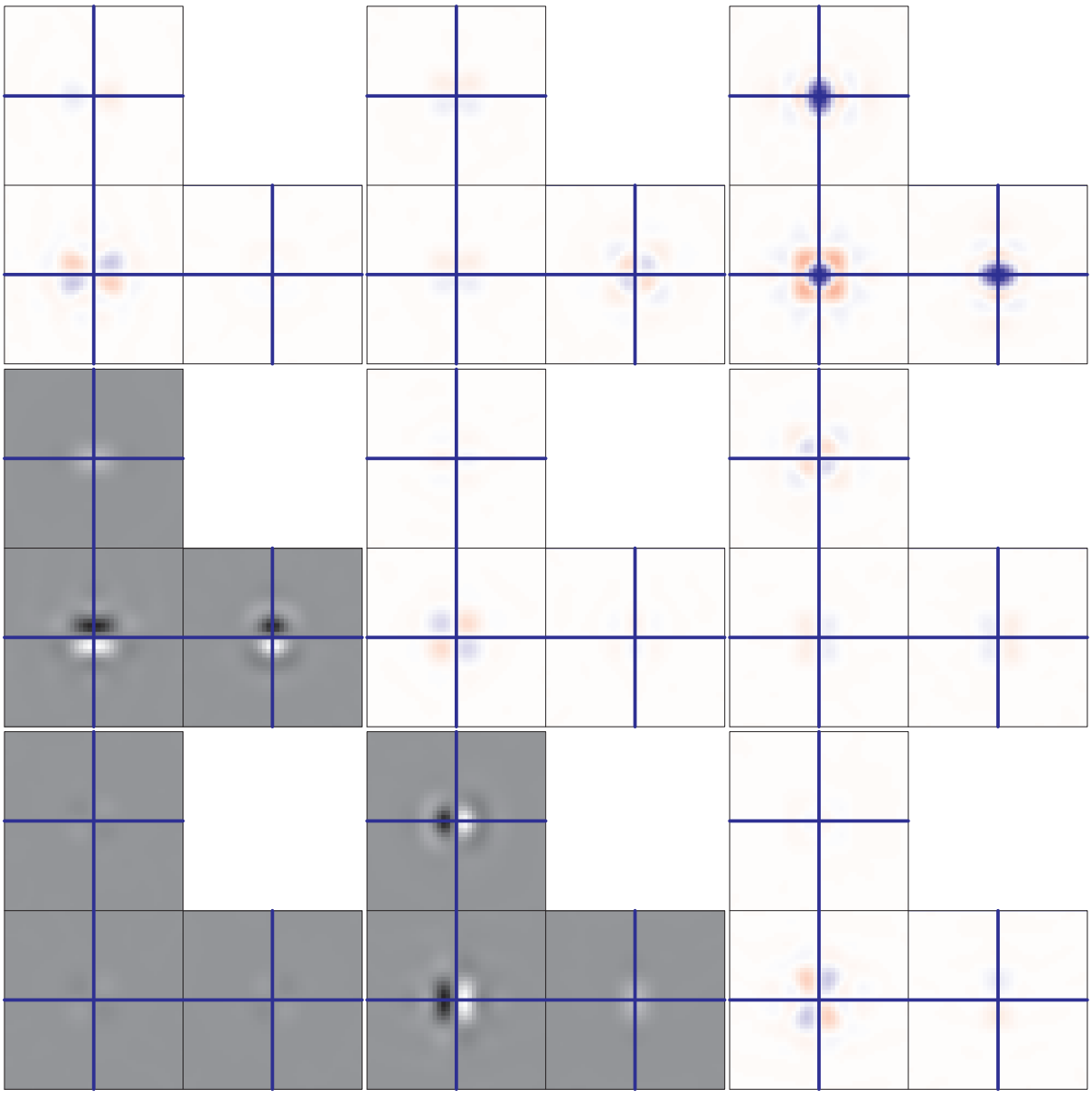

Figure 4.2: Source mechanism reverse time migration using the experiment setup in Figure 4.1(a) with seismic moment tensor $\mathbf{M} = \{\mathbf{0}, \mathbf{0}, \mathbf{0}, \mathbf{0}, -\mathbf{1}, \mathbf{0}\}$.

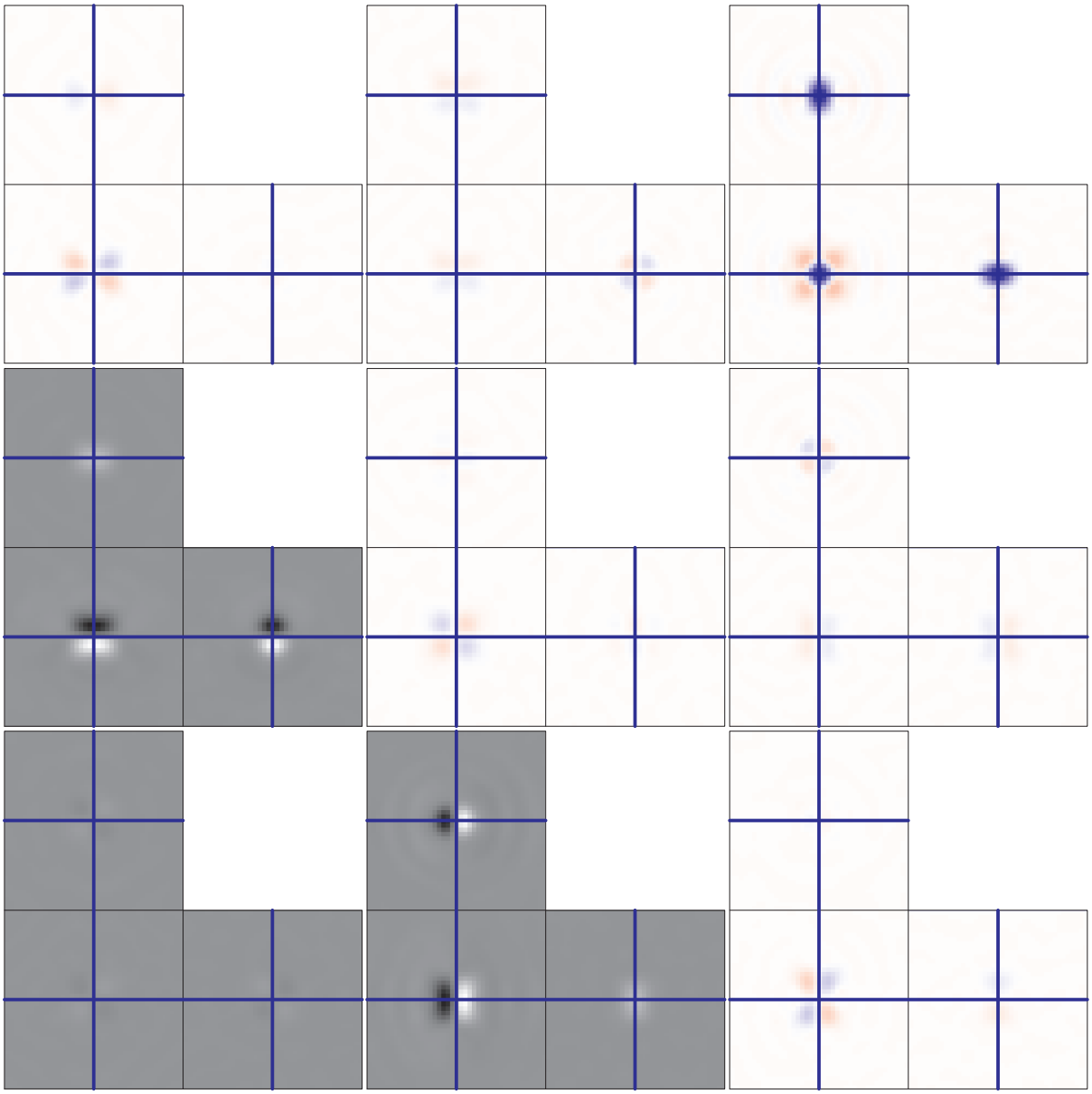

Figure 4.3: Source mechanism **Least-squares** reverse time migration corresponding to the images in Figure 4.2 with seismic moment tensor $\mathbf{M} = \{\mathbf{0}, \mathbf{0}, \mathbf{0}, \mathbf{0}, -\mathbf{1}, \mathbf{0}\}$.

We demonstrate the ability of our method to identify source mechanism with multiple nonzero components such as an explosion. The source images in Figure 4.4 that display symmetry are on the main diagonal of the moment tensor images that indicates an explosive source. The source images consist of stacked spheres along the components associated with the principal axis, i.e., M_{xx}, M_{yy}, and M_{zz} along x-, y-, and z-axis respectively. Besides that, we perform least-squares imaging on body force source such as a seismic vibrator source. In Figure 4.5, we use a vertical body force as our source mechanism. The only panel that shows symmetry is F_z which demonstrates the capability of our method to identify both moment tensor and body force sources. This is important for scenarios where the recorded data is insufficient to describe the moment tensor source, we can define them through its body force equivalent.

We repeat the experiment using surface receivers (Figure 4.1(b)) to demonstrate our method by using surface monitoring methods to test the robustness against wavefield truncation artifacts. The limited aperture which translates to inadequate sampling of the wavefield may lead to inaccurate identification of the source mechanism from the artifacts. However, we demonstrate the robustness of our method through least-squares to minimize artifacts. For comparison with the full aperture scenario, we use the same double-couple earthquake source example in Figure 4.2 but deploying surface receivers instead. The least-squares solution in Figure 4.6 shows that only panel M_{xz} describes the symmetry for source mechanism identification, although a reduction in compactness of the source image due to the limited aperture of a single-sided illumination from the top.

4.4 Discussion

We demonstrate the ability to locate and identify the seismic source mechanism accurately. Since our formulation is derived from the elastic anisotropic wave equation, our method can be applied to media of arbitrary anisotropy and heterogeneity given the media parameters are known (also a requirement for any other wavefield-based method). The source mechanism imaging method provides a fast and robust way to obtain the source pa-

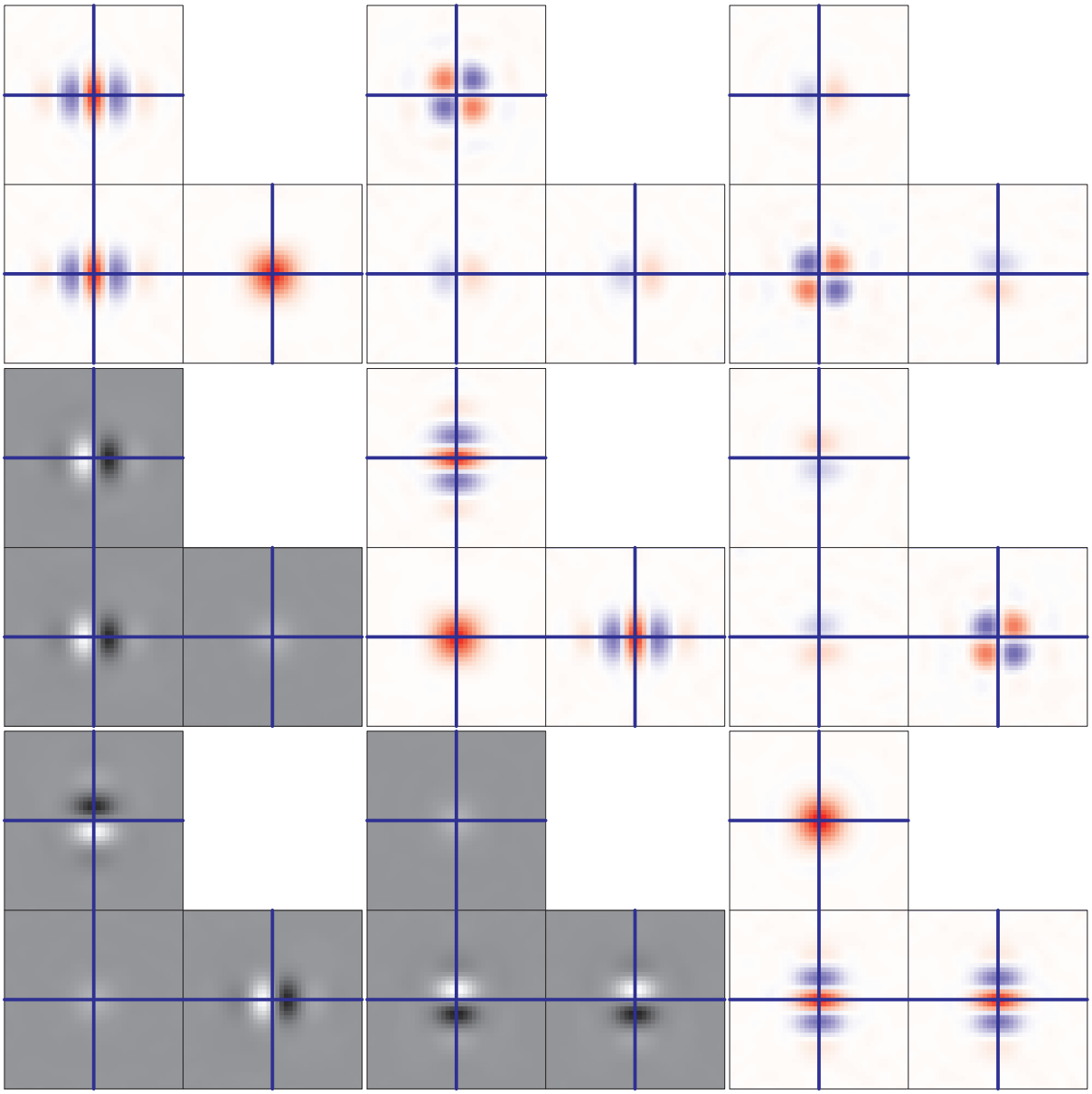

Figure 4.4: Source mechanism **Least-squares** reverse time migration for seismic moment tensor $\mathbf{M} = \{\mathbf{1}, \mathbf{1}, \mathbf{1}, \mathbf{0}, \mathbf{0}, \mathbf{0}\}$.

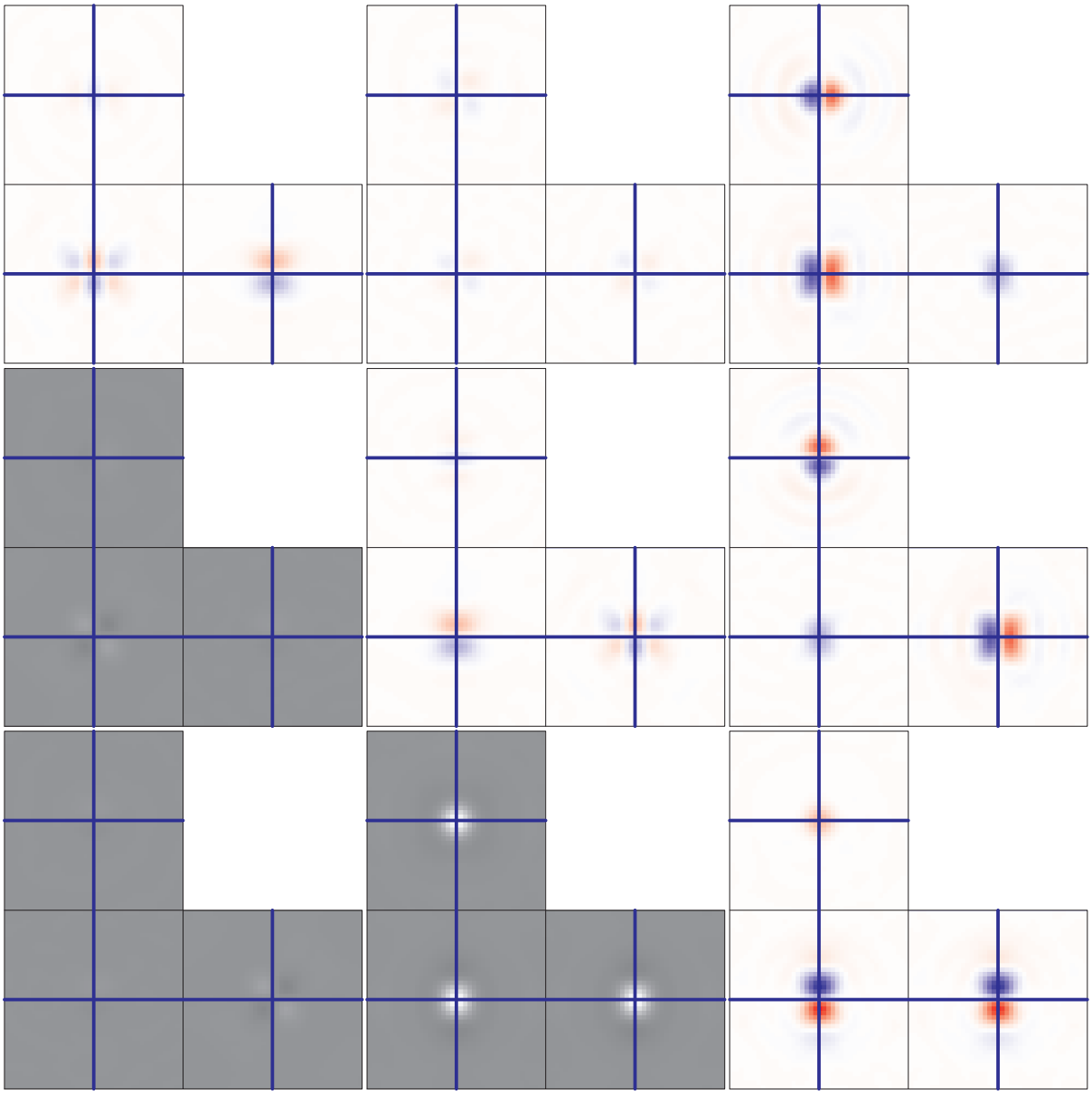

Figure 4.5: Source mechanism **Least-squares** reverse time migration for body force vector $\mathbf{F} = \{\mathbf{0}, \mathbf{0}, \mathbf{1}\}$.

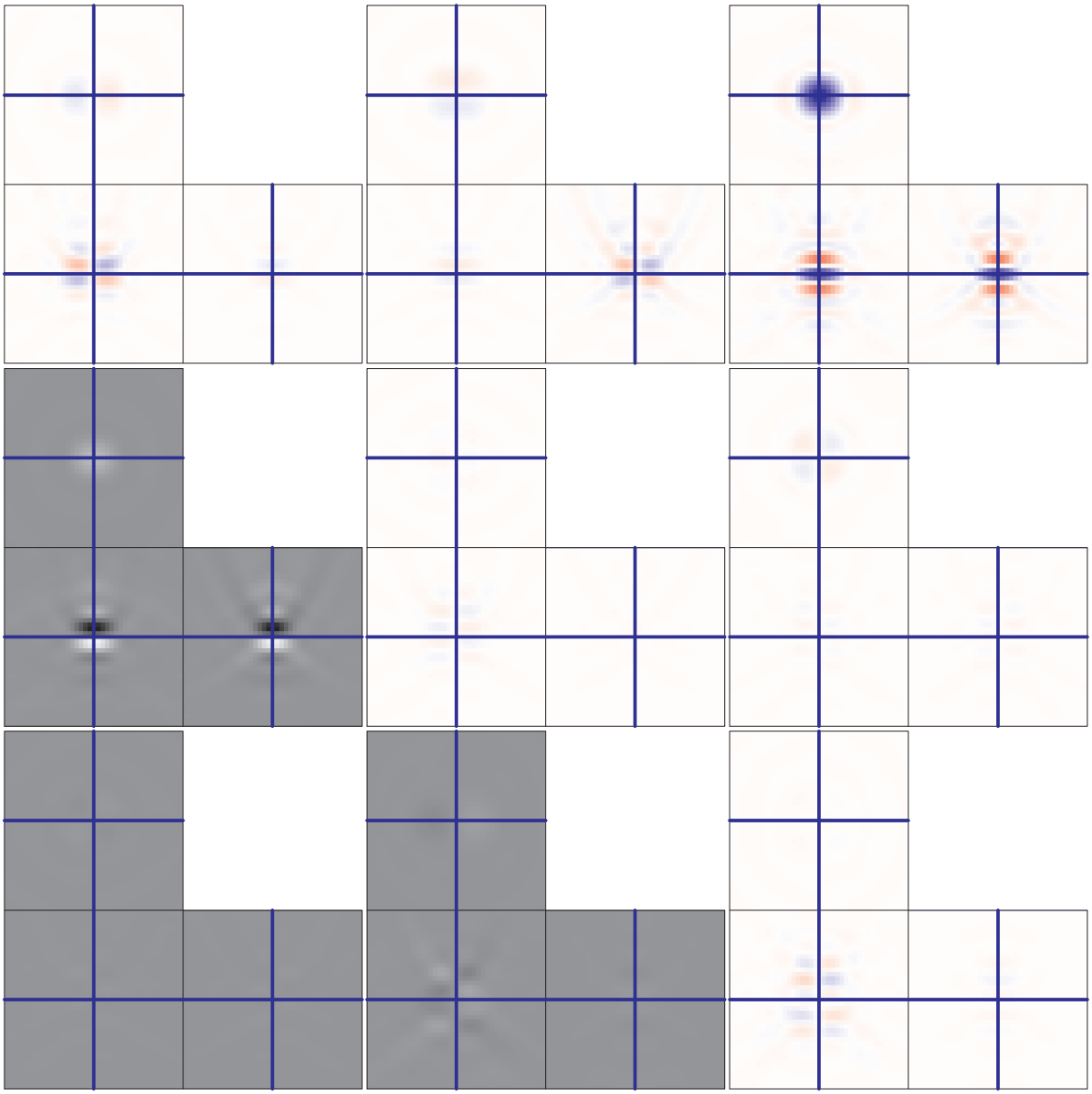

Figure 4.6: Source mechanism **Least-squares** reverse time migration using the surface seismic acquisition geometry in Figure 4.1(b) for seismic moment tensor $\mathbf{M} = \{\mathbf{0}, \mathbf{0}, \mathbf{0}, \mathbf{0}, -\mathbf{1}, \mathbf{0}\}$.

rameters without the need for lengthy iterative inversion. However, to reduce aperture and source wavelet related artifacts, we are required to perform least-squares imaging that would increase the computational cost. Our imaging method and conventional inversion-based methods are related in that the source images form the gradient for waveform inversions. The imaging condition in equation 4.16 is comparable to the moment tensor gradient defined from the Fréchet derivatives by Kim et al. (2011) in their centroid-moment tensor inversion method. Besides the moment tensor image, our approach also provides the body force image which is essential when the observed data are not capable to adequately describe the moment tensor source. A natural extension of our approach is to use all of the source images ($\mathbf{M}$ and $\mathbf{F}$) to perform waveform-based inversion to obtain medium parameters. The least-squares imaging provides high-resolution source images and could accelerate waveform inversions.

4.5 Conclusions

We demonstrate a wavefield-based imaging method that can robustly and accurately locate seismic sources and identify its mechanism. Our technique requires both stress and particle displacement data but can be formulated using either stress or particle displacement as special cases. This methodology leverages strain and displacement acquisition using novel multicomponent DAS acquisition. Our source images naturally identify the source mechanism as they are individual images for the respective moment tensor and body force components. The ability to obtain the source location and mechanism without the need for lengthy iterative processes could potentially allow practitioners to make timely decisions about the reservoirs for immediate business impact. Our method using the least-squares solution facilitates fast and accurate waveform inversion for source and medium parameters. The methodology presented in this paper applies to media of arbitrary anisotropy and heterogeneity.

4.6 Acknowledgments

We would like to thank the sponsors of the Center for Wave Phenomena, whose support made this research possible and Oscar Jarillo Michel for fruitful discussions. The reproducible numeric examples in this paper use the Madagascar open-source software package (Fomel et al., 2013) freely available from http://www.ahay.org.

CHAPTER 5

OPTIMAL ELASTIC SOURCE WAVEFIELD RECONSTRUCTION

To be submitted to *Geophysical Prospecting*

Ivan Lim Chen Ning[1,2,3] and Paul Sava[1]

Reverse time migration (RTM) is capable of producing seismic images of complex geology by correlating extrapolated source and receiver wavefields. RTM is commonly regarded as a memory intensive operation because the source and receiver are not synchronous, which fundamentally require wavefield storage. Many methods are proposed to manipulate the source wavefield efficiently, such as storing the wavefield in the boundary layer followed by its reconstruction as necessary. However, the memory requirement is still considerably voluminous due to the need to save at least several layers around the computational zone. By using the integral solution of the representation theorem enclosing the computational volume, we can reduce the boundary storage to a single layer and still precisely extrapolate the wavefield back into the volume. Building on this idea, we propose the reconstruction of the source wavefield for elastic RTM and waveform inversion from a single layer of the boundary enclosing the computational domain. This reduces the memory and the computational requirements, which is especially important for large-scale 3D experiments. Numerical examples demonstrate the effectiveness of our proposed method to successfully reconstruct the source wavefield from a single boundary layer without lessening the ability to produce accurate representations of the subsurface of arbitrary anisotropy and heterogeneity. We test our method to a distributed acoustic sensing (DAS) vertical seismic profile (VSP) dataset from the Eagle Ford shale formation.

[1]Graduate student and Professor, respectively, Center for Wave Phenomena, Colorado School of Mines, 1500 Illinois St., Golden, CO 80401, USA
[2]Primary researcher and author
[3]Author for correspondence

5.1 Introduction

Reverse time migration (RTM) is a household name in the world of exploration seismology and has become one of the primary workhorses for subsurface seismic imaging in complex geologic settings. The underlying principle of RTM involves correlation of source and receiver wavefields reconstructed in the entire image space. These wavefields are obtained through forward and backward wavefield extrapolation from the source function and the recorded data, respectively. For correlation, the two wavefields need to be available at all times and positions. A naive implementation of RTM would compute and save both source and receiver wavefields prior to correlation. For large-scale 3D experiments, accessing such large 4D (space and time) hypercubes is hugely expensive, both regarding storage and I/O. Since the RTM imaging condition implies zero-lag crosscorrelation, we can lessen the storage burden by accruing the image gradually as we access the reconstructed wavefields. Doing so requires wavefields readily available for simultaneous access which suggests large storage and costly I/O. Per contra, there are ways to efficiently store parts of the source wavefield to be reconstructed on the fly as we extrapolate the receiver wavefields backward in time. This approach reduces the I/O load significantly by a slight increase in computation cost.

A natural way to address the storage problem is to save intermediate time snapshots of the source wavefield hypercube and recursively fill in the wavefield at other times when necessary for correlation with the receiver wavefield (Symes, 2007; Anderson et al., 2012). This method is known as optimal checkpointing which is effective, yet still memory and computationally intensive. An alternative to significantly reduce storage requirements while reconstructing the source wavefield is to store the wavefield at a conventional boundary (Dussaud et al., 2008; Nguyen and McMechan, 2014; Yang et al., 2014) or a random boundary (Clapp, 2009; Shen and Clapp, 2011, 2015; Jia and Yang, 2017). Since the deployment of the random boundary reconstructs the source wavefield at the price of slight artifacts from the generation of scattered wavefields due to the random perturbations of material properties in the boundary zone, we focus on methods that utilize the conventional boundary method.

Accurate reconstruction of the source wavefield from the boundary requires storage of at least half the finite-difference stencil size. We can achieve further storage reduction by saving intermediate time steps, followed by filling in through interpolation (Yang et al., 2016). However, as we increase the accuracy of finite-difference, the boundary layer required for reconstruction increases along with the storage volume. Reducing the boundary layer size can be accomplished by a linear combination of the wavefields along the boundary at the expense of modest reconstruction errors (Liu et al., 2015). An alternative is to gradually reduce the finite-difference order as we approach the boundary, yet again with the loss of accuracy (Bo and Huazhong, 2011). To further decrease storage at a single boundary layer and maintain accuracy, one can improve the reconstruction through the Lax-Wendroff method by obtaining spatial derivative from temporal derivatives on the boundary (Tan and Huang, 2014; Mulder, 2017).

As an alternative to achieve significant memory storage reduction, we can use the representation theorem as the primary mechanism to reconstruct wavefields from minimal information available on the boundary of the domain through the deployment of so-called the multiple point sources (Morse and Feshbach, 1953; Masson et al., 2013). The source wavefield recorded on a single boundary layer (the surface) is reconstructed via multiple point source injection into the computational domain which is equivalent to the integral solution of the representation theorem (Aki and Richards, 2002; Wapenaar, 2014). This method is successfully demonstrated by Vasmel and Robertsson (2016), using the acoustic wave approximation.

The acoustic approximation is inadequate to characterize the Earth's elastic subsurface accurately. However, imaging methods based on the full elastic anisotropic wave equation are both expensive computationally and from the storage perspective. Ravasi and Curtis (2013) exploit the representation theorem for receiver-side exact elastic wavefield extrapolation for subsurface imaging that avoids nonphysical waves, i.e., wave modes reconstructed during reverse-time extrapolation that were not present in the observed data. In this paper,

we utilize the representation theorem to accurately reconstruct the elastic source wavefield from data stored on a single boundary layer. This methodology applies to memory intensive applications such as elastic RTM or elastic waveform tomography. Raknes and Weibull (2016) demonstrate a reconstruction by approximating the representation theorem at the cost of generating nonphysical wave modes. In this paper, we honor the full representation theorem as we illustrate the feasibility of this method numerical examples of elastic RTM using forward-propagated wavefields and reconstructed wavefields derived from stored boundaries.

5.2 Theory

We describe elastic-wave propagation using the second-order partial differential equations in space $\mathbf{x}$ and time t consisting both stress tensor $\underline{\mathbf{t}}\,(\mathbf{x},t)$ and the particle displacement vector $\mathbf{u}\,(\mathbf{x},t)$ wavefields (Aki and Richards, 2002)

$$\rho\,\frac{\partial^2\mathbf{u}}{\partial t^2} = \nabla\cdot\underline{\mathbf{t}} + \mathbf{f}\,, \tag{5.1}$$

where $\rho\,(\mathbf{x})$ is the density and $\mathbf{f}\,(\mathbf{x},t)$ is the external volume force. The stress $\underline{\mathbf{t}}\,(\mathbf{x},t)$ and strain $\underline{\mathbf{e}}\,(\mathbf{x},t)$ tensors are related through the constitutive relation with the assumption of linear elasticity by

$$\underline{\mathbf{t}} = \underline{\underline{\mathbf{c}}}\,(\underline{\mathbf{e}} + \underline{\mathbf{h}})\ , \tag{5.2}$$

where $\underline{\mathbf{h}}\,(\mathbf{x},t)$ is the external deformation source which together with stiffness tensor $\underline{\underline{\mathbf{c}}}\,(\mathbf{x})$ to forms a stress perturbation source $\underline{\mathbf{m}}\,(\mathbf{x},t) = \underline{\underline{\mathbf{c}}}\,(\mathbf{x})\ \underline{\mathbf{h}}\,(\mathbf{x},t)$. The relationship between the strain tensor and the particle displacement is

$$\underline{\mathbf{e}} = \frac{1}{2}\left[\,\nabla\mathbf{u} + (\nabla\mathbf{u})^{\intercal}\,\right]\ , \tag{5.3}$$

The representation theorem describing the particle motion in a volume Ω due to a body force $\mathbf{f}$ together with the traction $\underline{\mathbf{t}}\cdot\mathbf{n}$ and the displacement on the surface $\partial\Omega$ is given in

the convolution form as (Aki and Richards, 2002)

$$\mathbf{u}(\mathbf{x}) = \iiint_{\Omega} dV\, \mathbf{f}(\boldsymbol{\xi}) * \mathbf{G}(\mathbf{x},\boldsymbol{\xi}) + \oiint_{\partial\Omega} ds \left[\underline{\mathbf{t}}(\boldsymbol{\xi}) * \mathbf{G}(\mathbf{x},\boldsymbol{\xi}) - \underline{\underline{\mathbf{c}}}\, \mathbf{u}(\boldsymbol{\xi}) * \frac{\partial \mathbf{G}(\mathbf{x},\boldsymbol{\xi})}{\partial \boldsymbol{\xi}} \right] \cdot \mathbf{n}\,, \tag{5.4}$$

where $*$ denotes time convolution. $\boldsymbol{\xi}$ and $\mathbf{x}$ are the source and evaluation locations, respectively. The vector $\mathbf{n}$ is the normal to the surface $\partial\Omega$ enclosing the volume Ω. Figure 5.1 illustrates the physical elements of the representation theorem. If we assume that there are no external volume forces $\mathbf{f}$ present, the volume integral vanishes. The surface integral disappears under the assumption of a homogeneous boundary condition (Gangi, 1970). When the traction $\underline{\mathbf{t}} \cdot \mathbf{n}$ and the displacement $\mathbf{u}$ on the surface $\partial\Omega$ enclosing the volume Ω are excited from the external volume force $\mathbf{f}$ within the volume, i.e. the data recorded on a surface, we can express the particle displacement $\mathbf{u}$ wavefield inside the volume Ω surrounded by the surface $\partial\Omega$ as

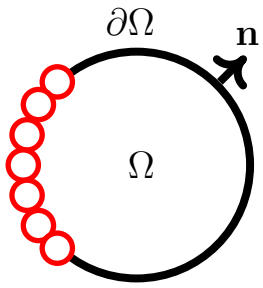

Figure 5.1: Schematic diagram to illustrate the elements of the representation theorem. The black circle denotes the surface $\partial\Omega$ enclosing a volume Ω with the corresponding normal vector $\mathbf{n}$ pointing outwards. The red circles denote the locations of sources/receivers.

$$\mathbf{v}(\mathbf{x}) = -\oiint_{\partial\Omega} ds \left[\underline{\mathbf{t}}(\boldsymbol{\xi}) * \mathbf{G}(\mathbf{x},\boldsymbol{\xi}) - \underline{\underline{\mathbf{c}}}\, \mathbf{u}(\boldsymbol{\xi}) * \frac{\partial \mathbf{G}(\mathbf{x},\boldsymbol{\xi})}{\partial \boldsymbol{\xi}} \right] \cdot \mathbf{n}\,. \tag{5.5}$$

The Green's function $\mathbf{G}(\mathbf{x},\boldsymbol{\xi})$ in equation 5.5 denotes a wave-propagator using the external volume force $\mathbf{f}$ as source. The stiffness tensor $\underline{\underline{\mathbf{c}}}$ together with the spatial derivative of the Green's function $\partial\mathbf{G}(\mathbf{x},\boldsymbol{\xi})/\partial\boldsymbol{\xi}$ in equation 5.5 form the equivalent of a wave-propagator using an external deformation force $\underline{\mathbf{h}}$ as the source in reverse-time propagation, the sign

inside the integral changes to negative to denote backward propagating Green's function (Wapenaar, 2014).

To obtain the integral solution of the representation theorem, we use the multiple point sources method (Morse and Feshbach, 1953; Masson et al., 2013) to turn the saved wavefield along the boundary $\partial\Omega$ into sources. In order to reconstruct the source wavefield using the representation theorem, we save the source wavefield along the boundary $\partial\Omega$ (black dots) as highlighted in Figure 5.2(a) which requires less memory than conventional methods. The conventional boundary methods reconstruct the source wavefield by storing at least half (Yang et al., 2014) of the finite-difference stencil size as shown in Figure 5.2(b).

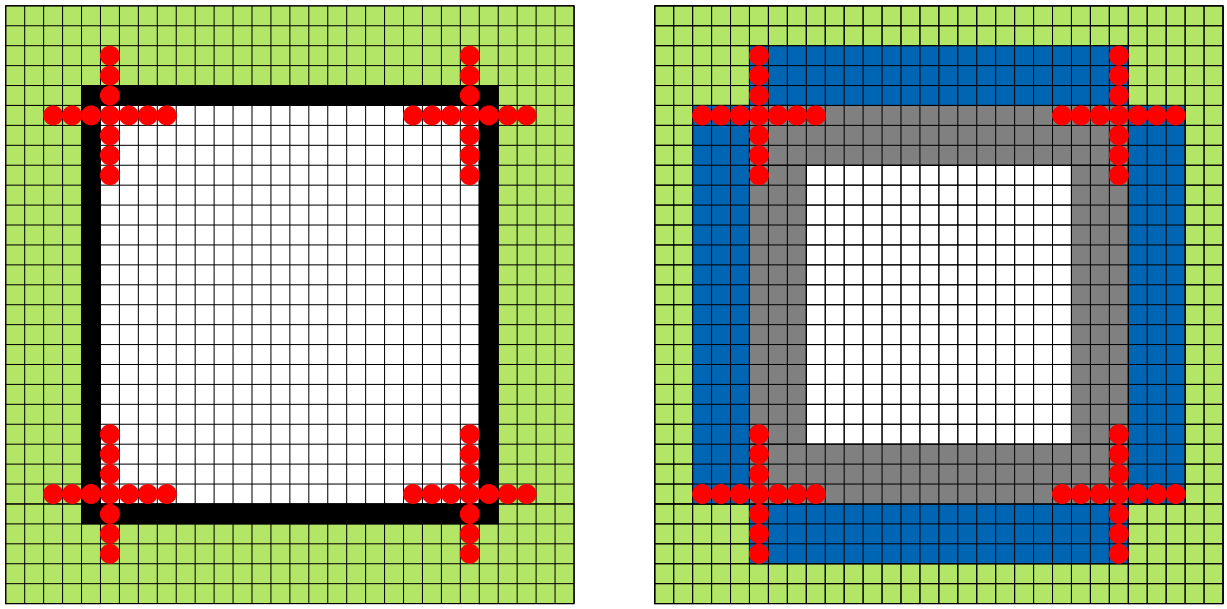

(a) (b)

Figure 5.2: An example for computational (in white) and boundary domain (in green) set up. (a) Our method to reconstruct the source wavefield only require storage at a single boundary layer (black dots). (b) Conventional methods require storage at half the finite-difference stencil either in the computational (in gray) or in the boundary (in blue) domain. Our method in (a) shows significant reduction for storage requirement compared to conventional methods in (b).

Our primary goal in this paper is to perform elastic RTM and LSRTM by reconstructing the source wavefield on the fly. To avoid comparing multiple elastic RTM images for a given

experiment, we adopt the energy imaging condition (Rocha et al., 2017) which generates a single elastic image without wave-mode decomposition. We modify the potential term of the imaging condition to exploit the forward simulated displacement and stress wavefields $(\mathbf{u}, \underline{\mathbf{t}})$ together with the adjoint displacement and strain wavefields $\left(\mathbf{u}^{\dagger}, \underline{\mathbf{e}}^{\dagger}\right)$

$$\begin{aligned} \mathcal{I} &= \sum_{e,t} \left[\rho \dot{\mathbf{u}} \cdot \dot{\mathbf{u}}^{\dagger} - \left(\underline{\underline{\mathbf{c}}}\, \underline{\mathbf{e}}\right) \cdot \underline{\mathbf{e}}^{\dagger}\right] \\ &= \sum_{e,t} \left[\rho \dot{\mathbf{u}} \cdot \dot{\mathbf{u}}^{\dagger} - \quad \underline{\mathbf{t}} \cdot \underline{\mathbf{e}}^{\dagger}\right] \end{aligned} \tag{5.6}$$

where the image $\mathcal{I}(\mathbf{x})$ is formed by summation over experiment e. The dot $(\dot{})$ represents time derivative, and the dagger $\left(^{\dagger}\right)$ denotes adjoint. The reformulation allows us to avoid the additional re-computation of wavefield derivatives in the kinetic term of the imaging condition as we solve equation 5.13 through the elastodynamic relationship. As pointed out by Rocha et al. (2017), the source and receiver particle velocity $\left(\dot{\mathbf{u}}, \dot{\mathbf{u}}^{\dagger}\right)$ wavefields describe the kinetic energy term, and the elastic strain $\left(\underline{\underline{\mathbf{c}}}\, \underline{\mathbf{e}}, \underline{\mathbf{e}}^{\dagger}\right)$ gives the potential energy term. The imaging condition represents the Lagrangian density, the difference between kinetic and potential energy.

5.3 Source reconstruction example

In reconstructing the source wavefield, we first perform a forward propagation in time and save the wavefield at a single layer between the computational and boundary domains, as shown in Figure 5.2(a). Wavefield computation occurs in the volume Ω, and the single layer where we store the source wavefield in the boundary $\partial\Omega$, equation 5.5. The source wavefield is reconstructed backward in time together with the receiver wavefield. To illustrate the theory numerically, we use a simple two-layer elastic model with the P-wave velocity shown in Figure 5.3(a). The S-wave and density are constant at 1300 m/s and 1000 kg/m^3, respectively. When comparing the source wavefield, we save the forward extrapolated source wavefield to serve as a reference for the wavefield reconstructed from the boundary $\partial\Omega$ using the representation theorem. We present the wavefield displays in the following tensor-vector matrix layout

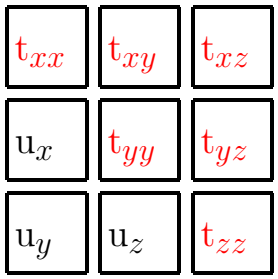

,

where we combine the stress tensor in its natural matrix form together with the particle displacement vector wavefield. In the case of 2D simulations confined to the xz-plane, the corresponding y-components are left empty. Figure 5.4 shows the reference source wavefield at 3 different time snapshots using an explosive type source from the location of the white dot shown in Figure 5.3(a) at $(0.075 \text{ km}, 0.005 \text{ km})$. Figure 5.5 shows the corresponding reconstructed source wavefield. We evaluate the accuracy of the reconstruction by analyzing the difference wavefield plots between reference and reconstruction in Figure 5.6. The subtle amplitudes in the difference plot are due to the weak reflections from imperfect absorbing boundary condition. The four corners of the computational domain contribute towards the amplitudes in the difference plot as well. At the corner points, the normal vectors $\mathbf{n}$ are undefined which contribute towards the generation of artifacts during reconstruction. A possible solution is to adopt the superellipse geometry in place of the rectangle.

To further examine the reconstruction accuracy, we graph the wavefields along the x-axis at a depth of 0.025 km. Figure 5.7 shows the graphs for the reference source wavefield (in blue) overlaid on the reconstructed source wavefield (in red) for the same time snapshots as in Figure 5.4 and 5.5. The small ripple like artifacts in Figure 5.6 are due to the corner points.

5.4 RTM example

Notwithstanding a successful reconstruction of the source wavefield, we apply the method to elastic RTM using the energy norm imaging condition in equation 5.6. Figure 5.3(b) shows the smooth velocity model for RTM. We use the reference wavefield to produce the reference energy norm RTM image based on the so-called full wavefield storage method

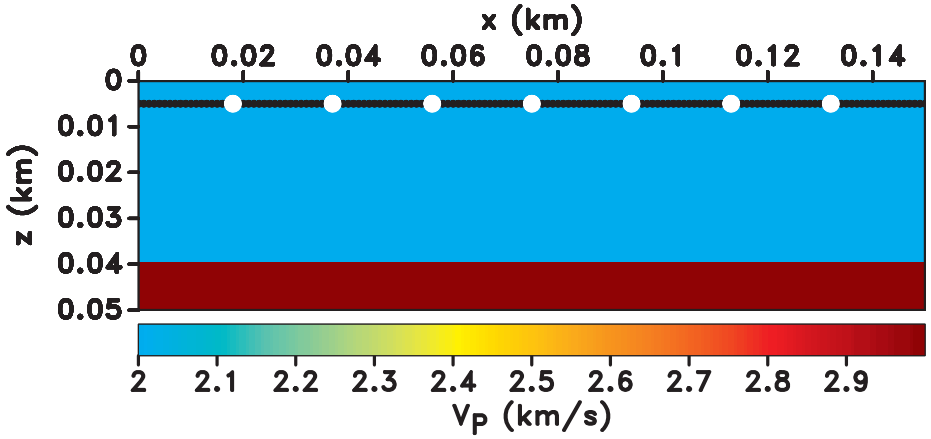

(a)

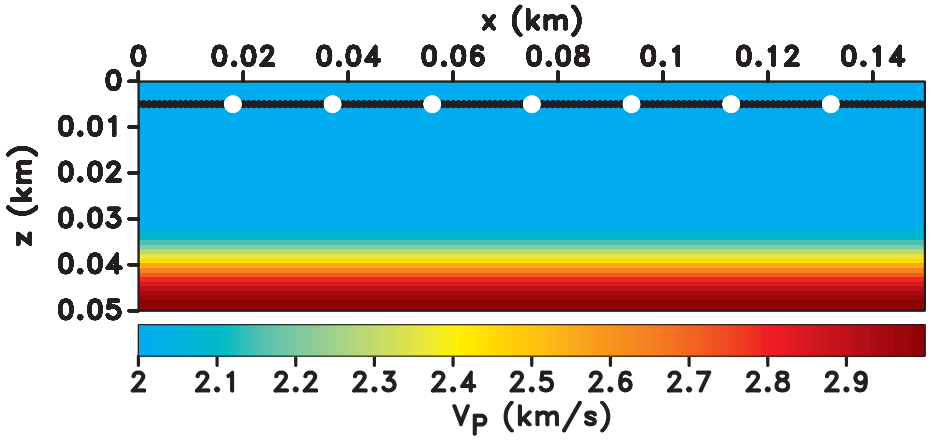

(b)

Figure 5.3: (a) The P-wave velocity model with an overlay of a 2D experiment depicting the source (white dots) and receiver (black line) locations. (b) The corresponding smooth P-wave velocity for reverse time migration.

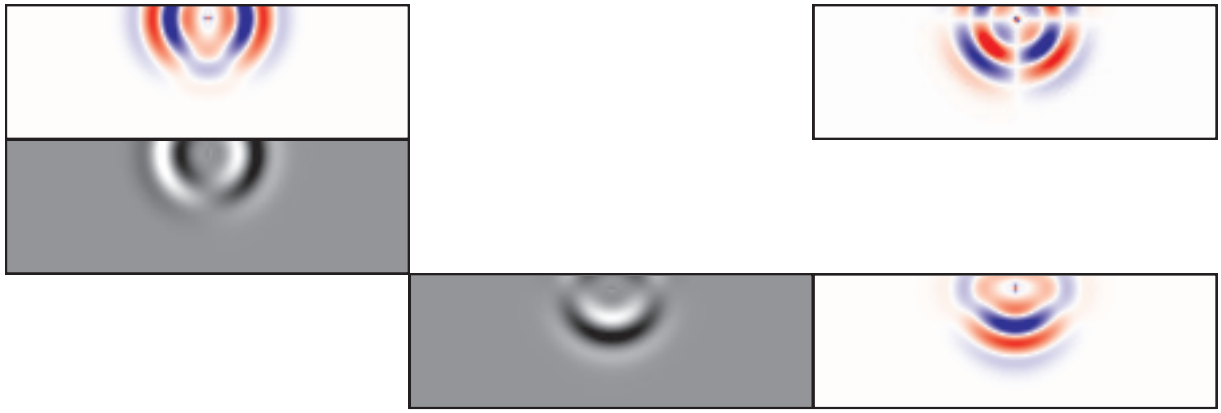

(a)



(b)

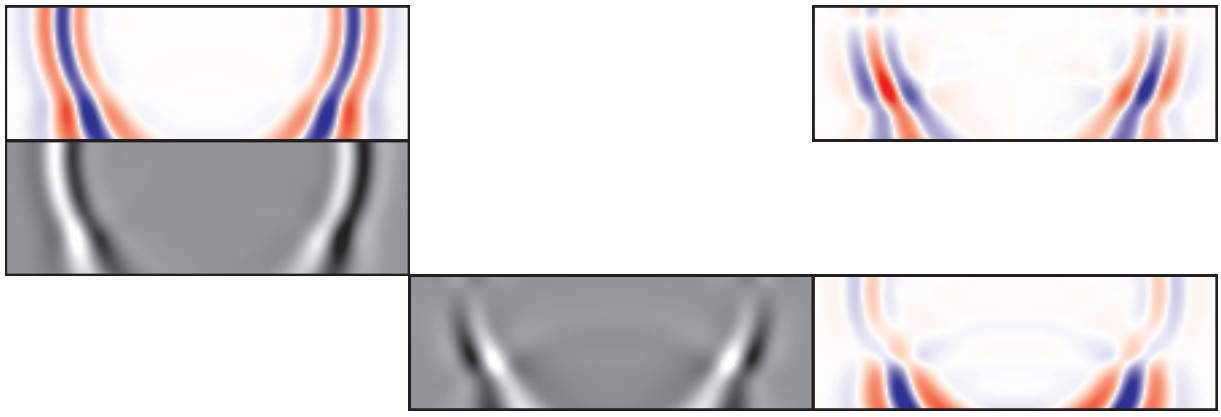

(c)

Figure 5.4: Snapshots of the reference source wavefield for time-step at (a) 200, (b) 300, and (c) 400. In all panels, the vertical axes represent depth, whereas the horizontal axes denote horizontal position. The panels consist of the stress $(\mathrm{t}_{xx}, \mathrm{t}_{zz}, \mathrm{t}_{xz})$ tensor and particle displacement $(\mathrm{u}_x, \mathrm{u}_z)$ vector field in the tensor-vector matrix layout.

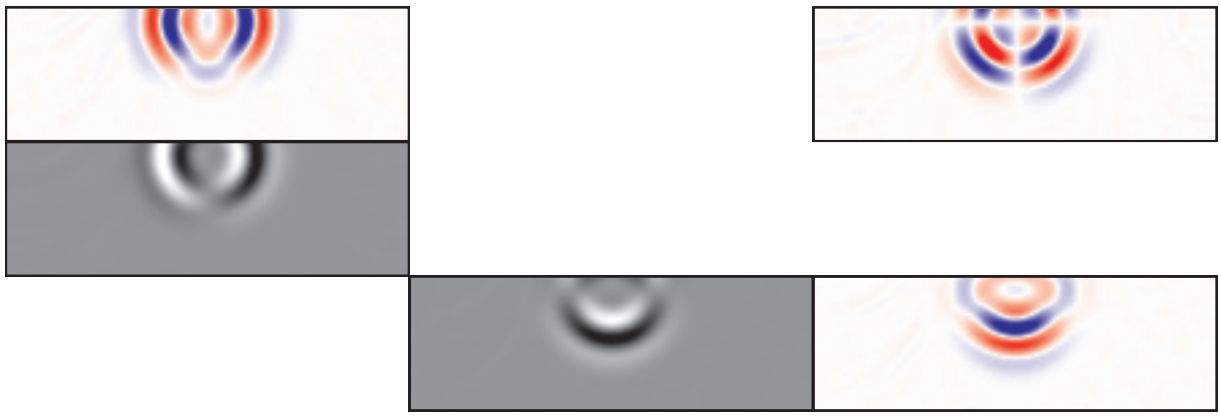

(a)



(b)

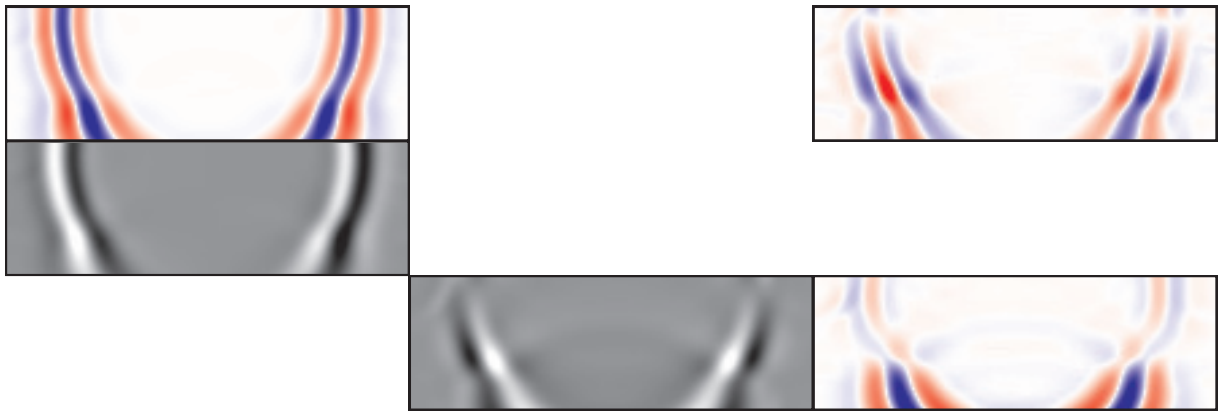

(c)

Figure 5.5: Snapshots of the reconstructed source wavefield from a single boundary layer for time-step at (a) 200, (b) 300, and (c) 400. In all panels, the vertical axes represent depth, whereas the horizontal axes denote horizontal position. The panels consist of the stress $(\mathrm{t}_{xx}, \mathrm{t}_{zz}, \mathrm{t}_{xz})$ tensor and particle displacement $(\mathrm{u}_x, \mathrm{u}_z)$ vector field in the tensor-vector matrix layout.

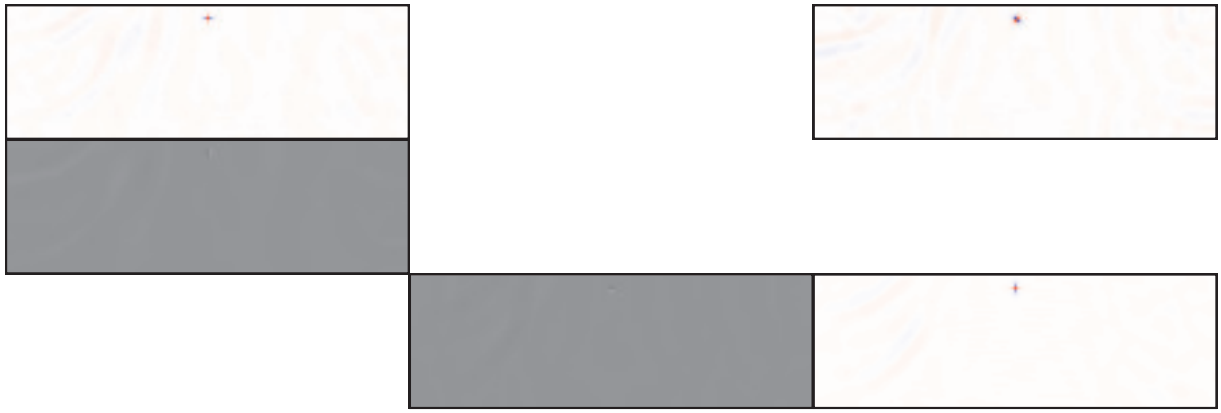

(a)

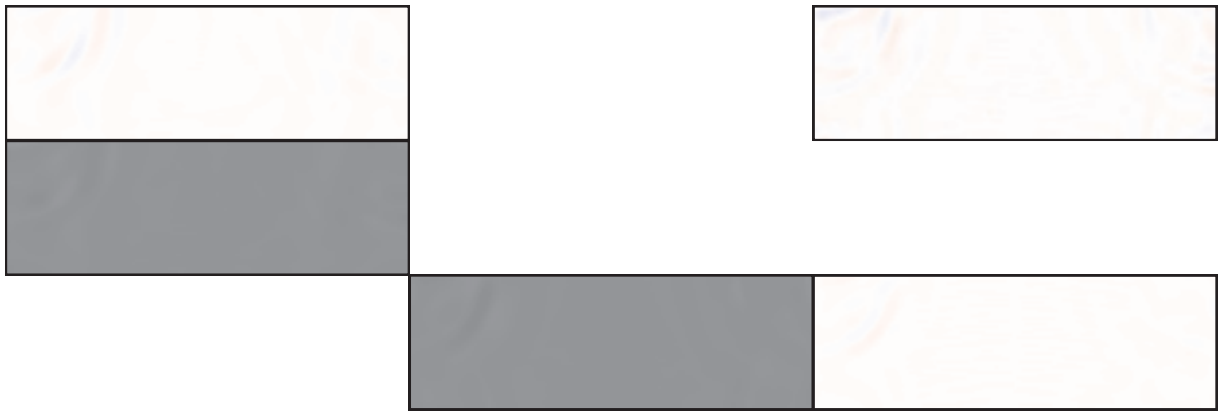

(b)

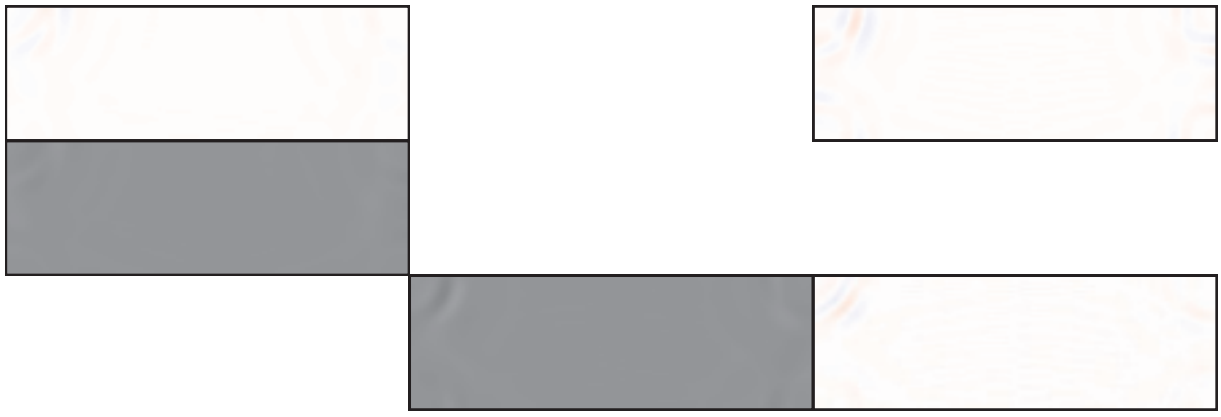

(c)

Figure 5.6: Snapshots of the difference between the forward source wavefield (Figure 5.4) extrapolation and the reconstructed source wavefield (Figure 5.5) from the single boundary layer for time-step at (a) 200, (b) 300, and (c) 400. In all the panels, the vertical axes represent depth whereas the horizontal axes denote horizontal position.

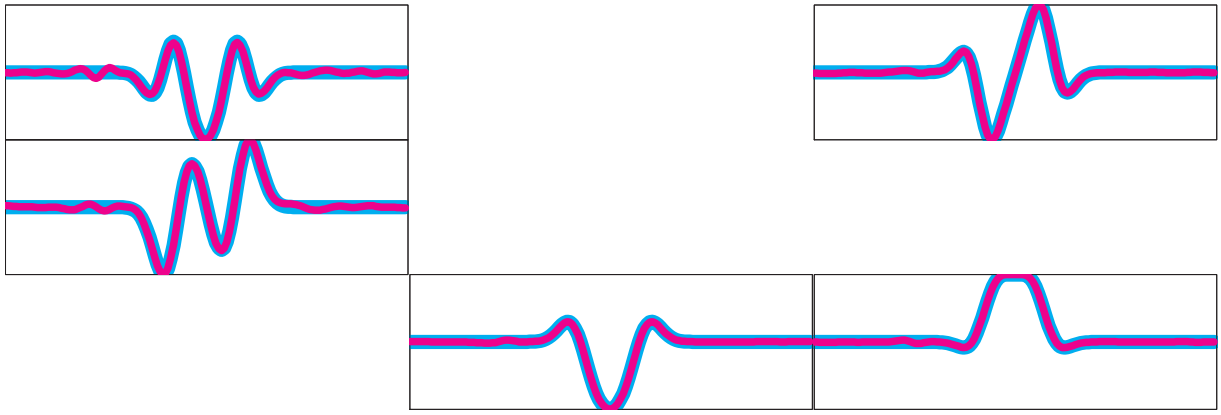

(a)

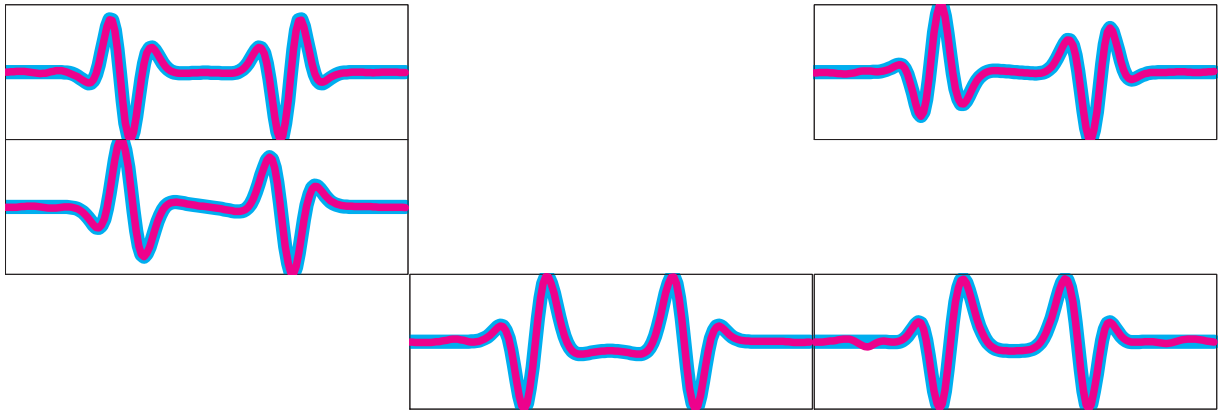

(b)

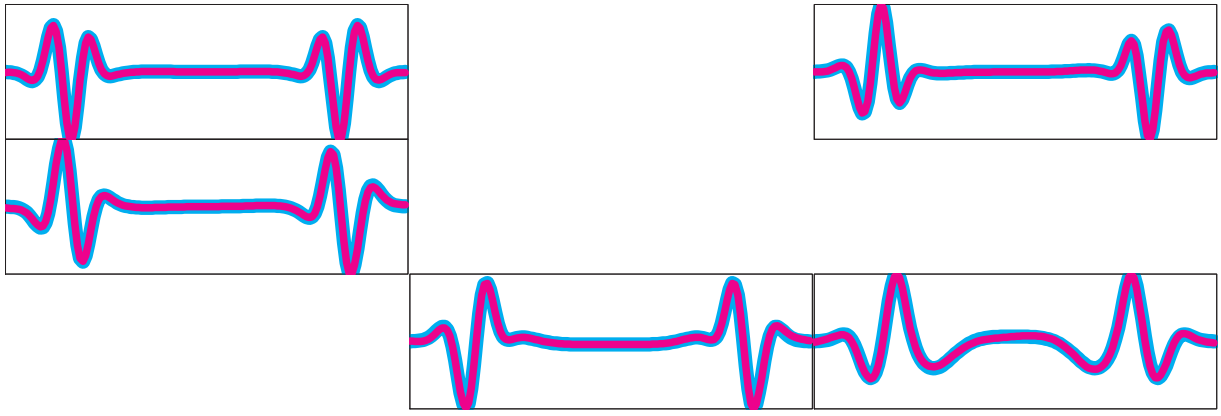

(c)

Figure 5.7: Graph along depth $z = 0.025$ km for the reference source wavefield (in blue) and the reconstructed source wavefield (in red) at time-steps of (a) 200, (b) 300, and (c) 400. The vertical axis of the individual panels represents the amplitude whereas the horizontal axis denotes the horizontal position. The panels consist of the stress $(\mathrm{t}_{xx}, \mathrm{t}_{zz}, \mathrm{t}_{xz})$ tensor and particle displacement $(\mathrm{u}_x, \mathrm{u}_z)$ vector field in the tensor-vector matrix layout.

(Nguyen and McMechan, 2014). Figure 5.8 depicts images for a single shot of the reference image, Figure 5.8(a) and for the reconstructed source wavefield, Figure 5.8(b), as well as the difference, Figure 5.8(c). Since Figure 5.8(a) and 5.8(a) are near identical, we take the difference plot in Figure 5.8(c) where the amplitudes here are due to the corner points artifacts in the source wavefield reconstruction. Note the amplitude difference at the source location in Figure 5.8(b), caused by the fact that the source wavefield continues to expand after collapsing at the source location at the wavelet peak time.

We also extract amplitude profiles along the depth direction (vertical dotted line) at the shot location and along the horizontal direction (horizontal dotted line) at the reflection depth in Figure 5.8. Figures 5.8(a) and 5.8(b) show the same amplitude profile with the reference image (in blue) overlaid with the reconstructed source wavefield image (in red). The amplitude profiles are in excellent agreement overall with the corresponding difference image track along zero. The residual sum of squares (RSS) for the difference image normalized to the reference image is approximately 0.2%.

We perform RTM on all the shots (7 total) and stack the images to perform a similar analysis for the single shot RTM. Figure 5.9(b) shows the reference image, and Figure 5.9(a) depicts the image using reconstructed source wavefields for all shots. The same artifacts due to the source wavefield expanding beyond wavelet peak time in Figure 5.8(c) are present in Figure 5.9(c). The same semi-vertical events at 0.01, 0.03, 0.05, 0.06, 0.07, 0.10, 0.12, and 0.14 km are crosstalk between the source and receiver wavefields that propagate along the horizontal axis. The amplitude profiles on the RTM image for all shots share the same observations as the single shot images and the difference image amplitude profile is consistently zero where the RSS normalized to the reference image is approximately 1%.

5.5 Marmousi II example

We also test our method for source wavefield reconstruction on an anisotropic version of the elastic Marmousi II model (Martin et al., 2006), shown in Figure 5.10. We calculate the dimensionless Thomsen parameters for vertical transverse isotropy (VTI) ε and δ using

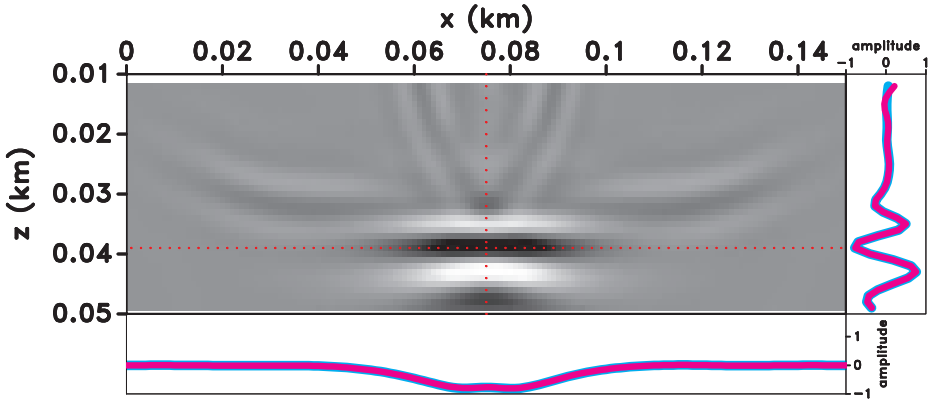

(a)

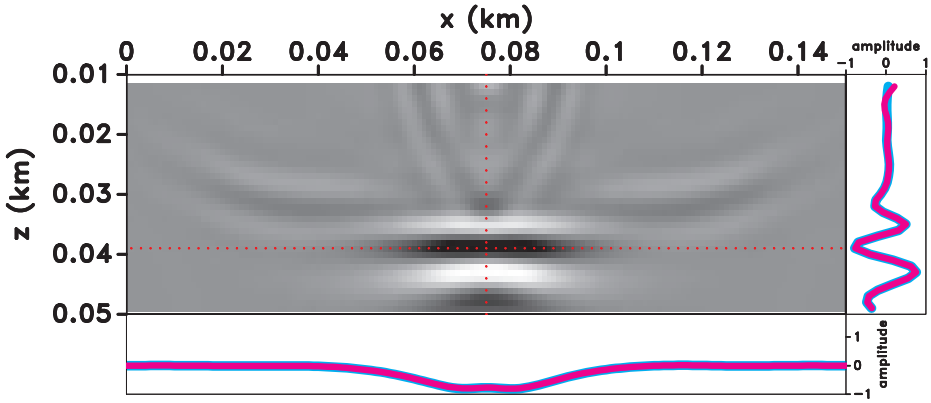

(b)

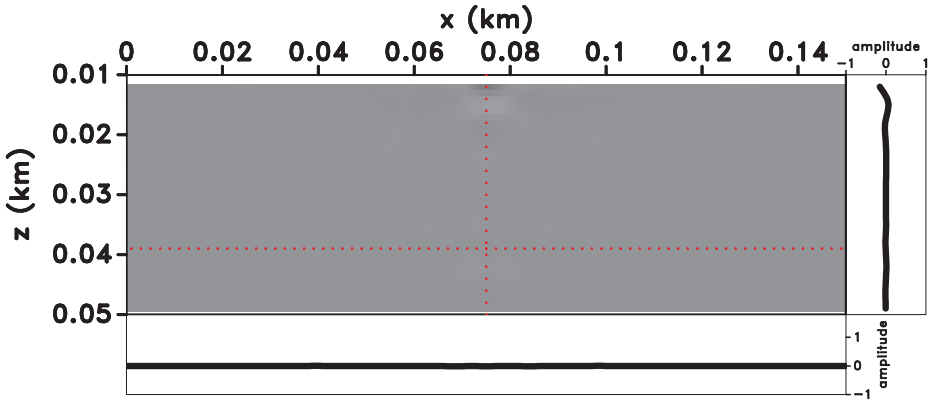

(c)

Figure 5.8: Single shot energy norm elastic reverse time migration using (a) forward source wavefield extrapolation and (b) reconstructed source wavefield. (c) The corresponding difference plot between (a) and (b). The graphs at the bottom of (a), (b), and (c) denote amplitude profile along the horizontal direction (horizontal dotted line) at the reflection depth while the graphs on the right show the amplitude profile along the depth direction (vertical dotted line) at the shot location. The blue amplitude profile corresponds to (a), red from (b), and black from (c).

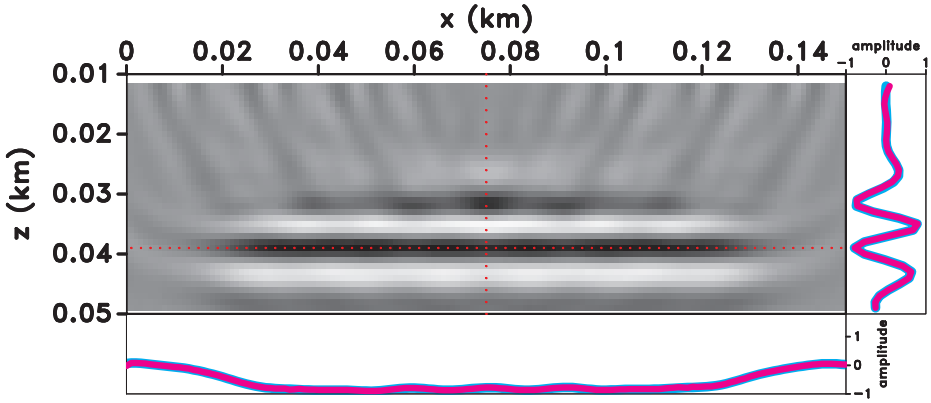

(a)

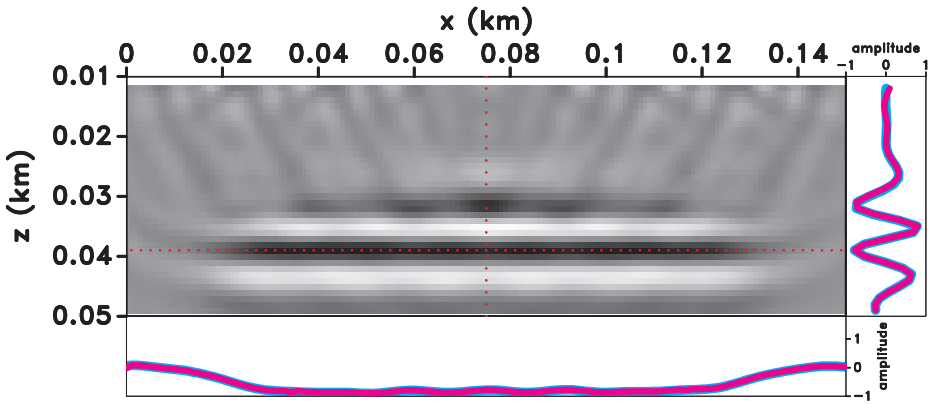

(b)

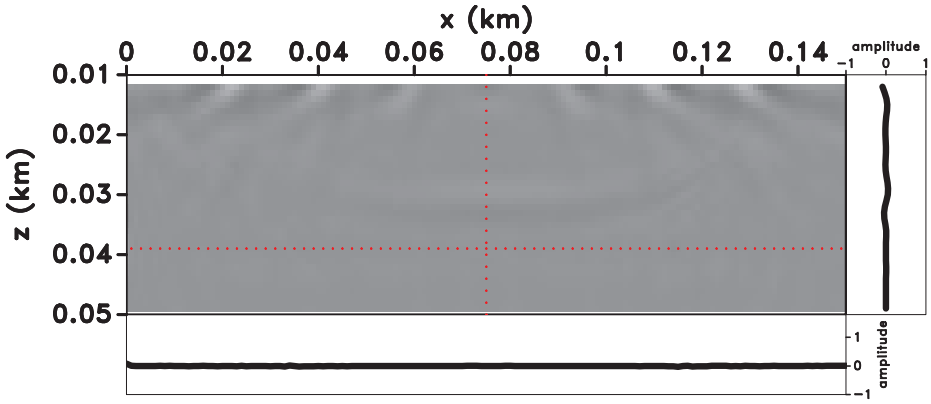

(c)

Figure 5.9: Energy norm elastic reverse time migration from all the available shots using (a) forward source wavefield extrapolation and (b) reconstructed source wavefield. (c) The corresponding difference plot between (a) and (b). The graphs at the bottom of (a), (b), and (c) denotes amplitude profile along the x-axis (horizontal dotted line) at the reflection depth while the graphs on the right show the amplitude profile along the z-axis (vertical dotted line) at the shot location. The blue amplitude profile corresponds to (a), red from (b), and black from (c).

the density model with the expressions of $\varepsilon = 0.25\rho - 0.3$ and $\delta = 0.125\rho - 0.125$ adopted from Yan and Sava (2012). We compare the reference and reconstructed source wavefields, Figures 5.11(a) and 5.11(b), respectively. The small amplitude contrasts in the difference plot (Figure 5.11(c)) are mainly due to numerical dispersion and the corner points of the boundary used for backward reconstruction. Despite the small differences, we can image the Marmousi II model by performing RTM using the energy norm imaging condition on the smoothed models for a single shot (Figure 5.12(a)) and 17 shots (Figure 5.12(b)).

5.6 Eagle Ford Shale example

We validate our proposed method using a 2D walkaway vertical seismic profile (VSP) field dataset acquired using distributed acoustic sensing (DAS) in Lavaca County, Texas, USA. Although the DAS data are acquired in both the vertical and horizontal sections within the deviated well, we select only the vertical portion of optical fiber, as shown in Figure 5.13(a). We are unable to observe any arrivals in the horizontal section of the DAS recordings due to the low signal-to-noise ratio and the directivity of the optical fiber measurement. The DAS data consist of recordings at approximately every 8 m using a gauge length of 10 m. Figure 5.13(a) shows the estimated compressional velocity through first-break picking and Figure 5.13(b) shows the shear velocity derived from the available well logs. To perform RTM, we utilize the upgoing wavefield from the VSP data. The imaging condition for this example is the modified energy norm formulation in equation 5.6.

Similar to examples discussed in sections 5.3 to 5.5, we compare the boundary source wavefield reconstruction method with the reference wavefield obtained by storing the forward extrapolated source wavefield. We select a single shot in the middle of the survey to show the energy norm RTM image using the reference source wavefield, Figure 5.14(a) and the corresponding image obtained through source wavefield reconstruction, Figure 5.14(b). The difference between Figures 5.14(a) and 5.14(b) is shown in Figure 5.14(c). Although low in amplitude, differences exist around the source location due to the backward source wavefield reconstruction expanding beyond wavelet peak time and due to the corners of the

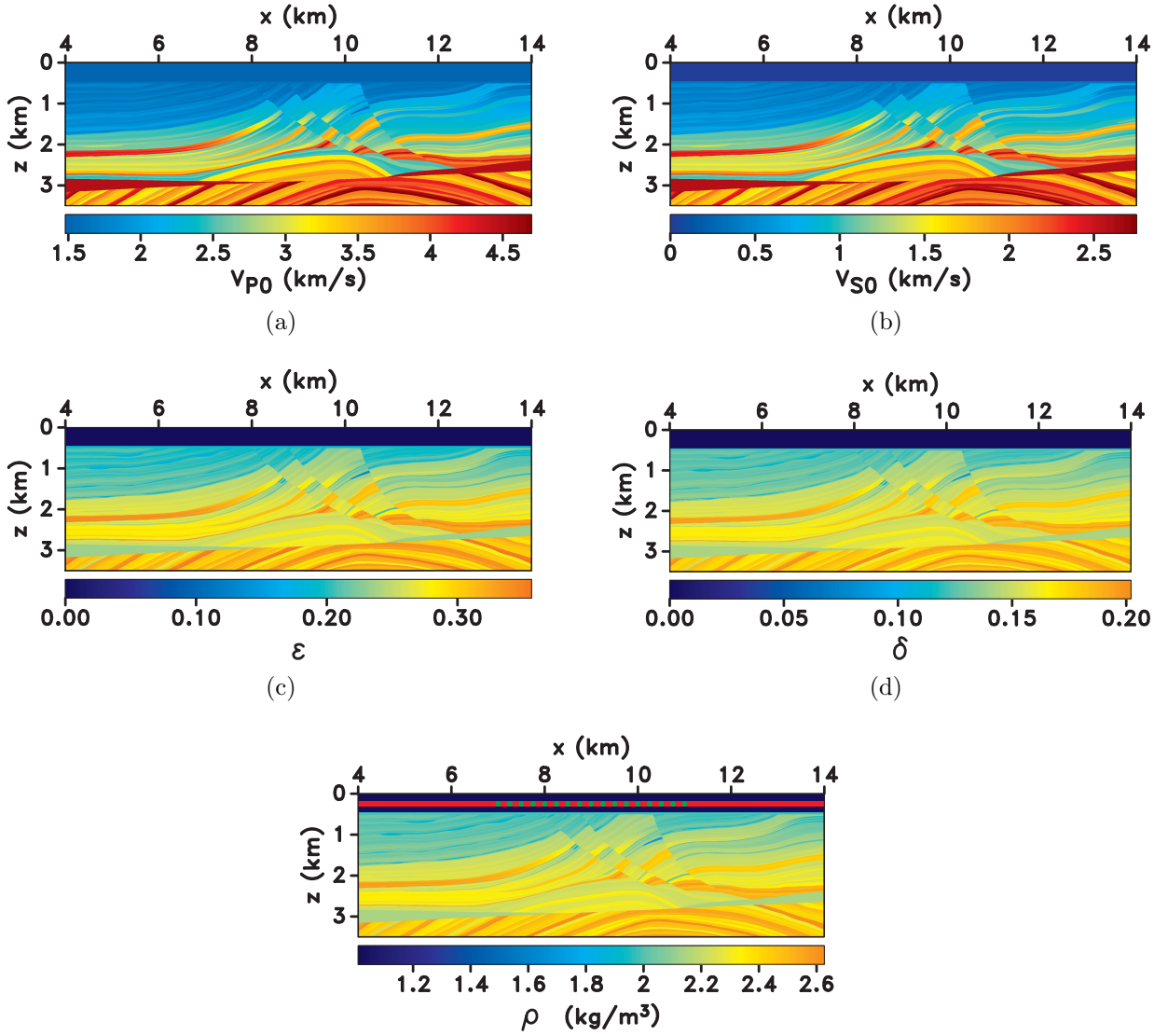

Figure 5.10: Vertical transverse isotropic Marmousi II model with the vertical (a) P (V_{P0}) and (b) S (V_{S0}) velocities. The dimensionless anisotropic Thomsen parameters (c) ε and (d) δ are derived from (e) the density model. The overlay white dots and red line in (e) depict the source and receiver locations, respectively.

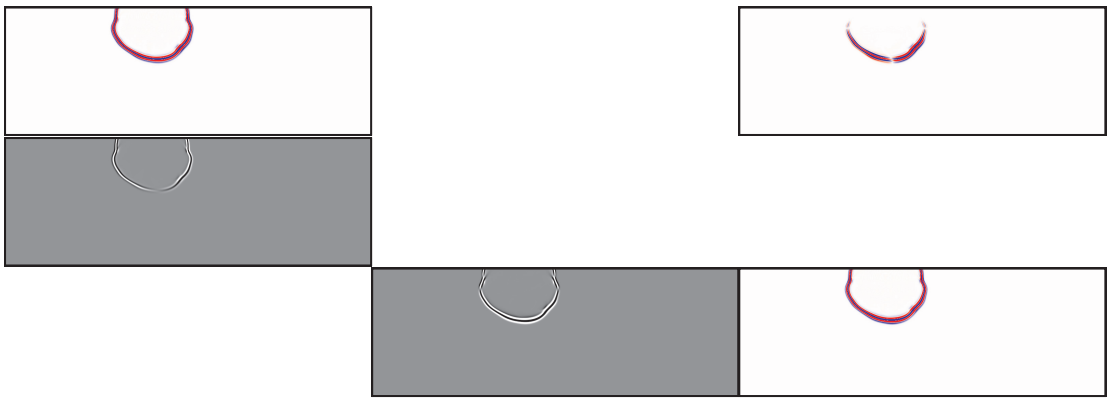

(a)

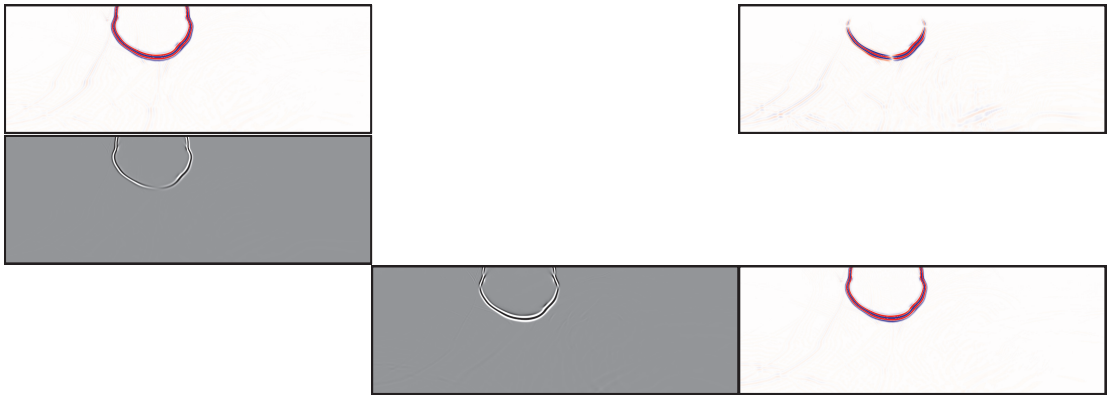

(b)

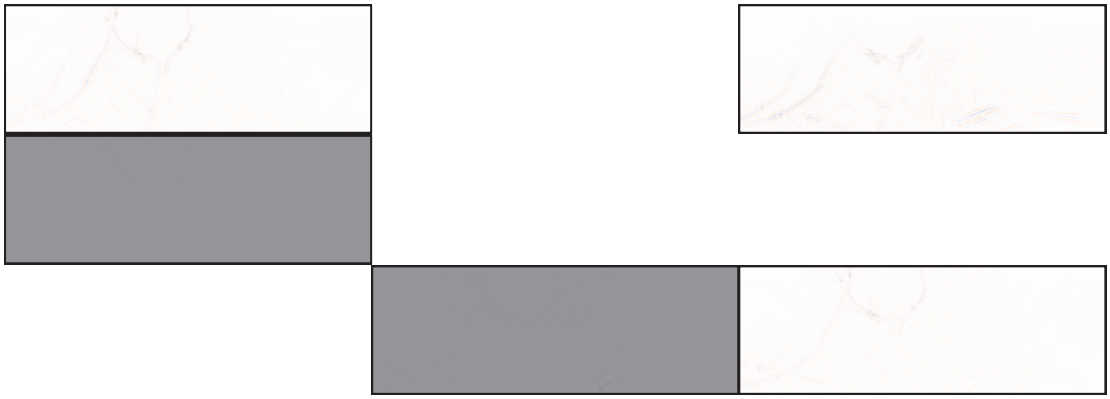

(c)

Figure 5.11: A wavefield snapshot in the anisotropic elastic Marmousi II model shown in Figure 5.10 for the (a) reference and (b) reconstructed source wavefields. (c) The corresponding difference between (a) and (b). The vertical and horizontal axes of the panels represent depth and horizontal position. The panels consist of the stress $(\mathrm{t}_{xx}, \mathrm{t}_{zz}, \mathrm{t}_{xz})$ tensor and particle displacement $(\mathrm{u}_x, \mathrm{u}_z)$ vector in the tensor-vector matrix layout.

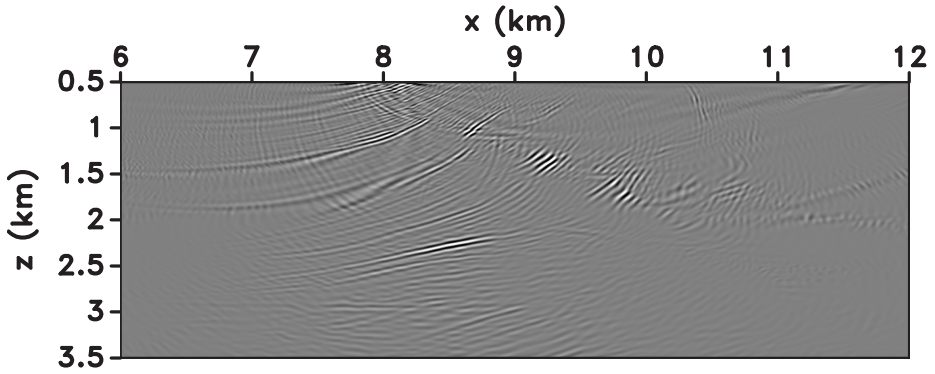

(a)

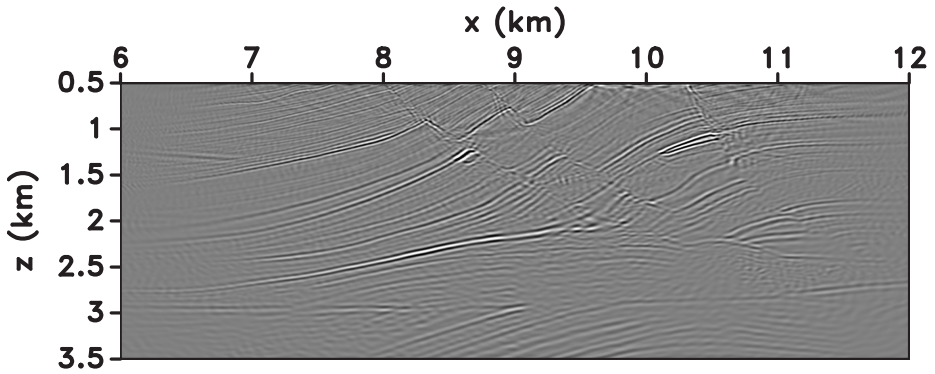

(b)

Figure 5.12: Energy norm elastic reverse time migration for the anisotropic Marmousi II model in Figure 5.10 using the reconstructed source wavefields for (a) a single shot and (b) all 17 shots.

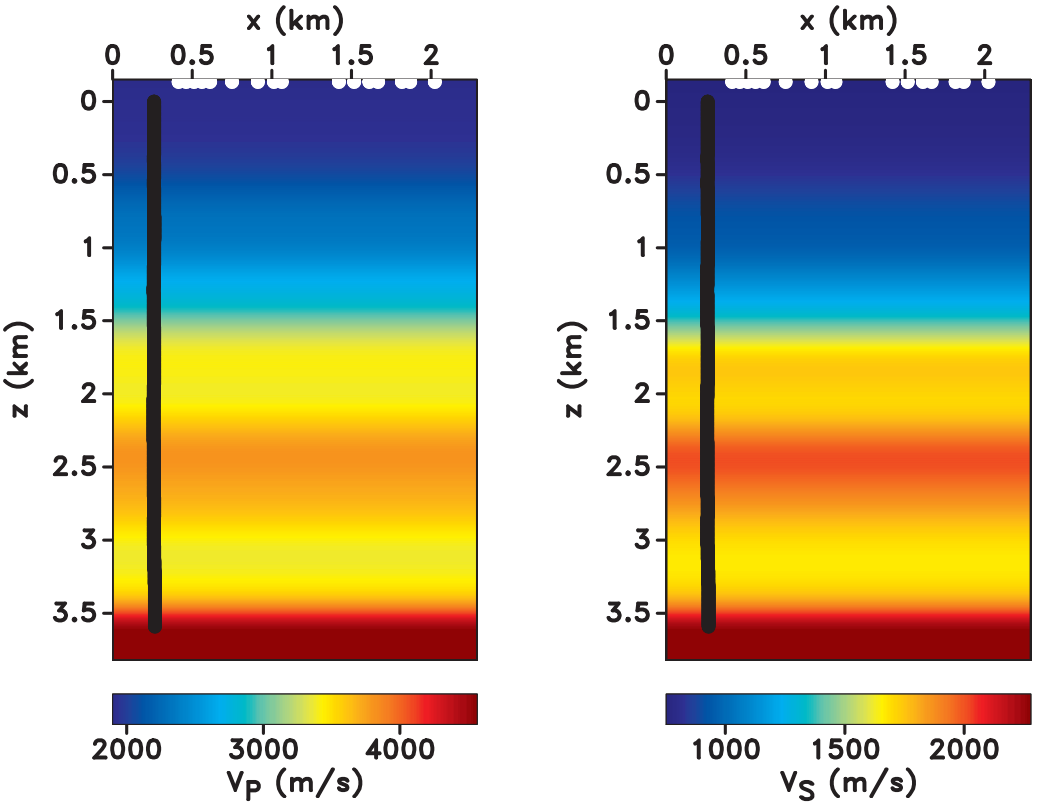

(a) (b)

Figure 5.13: Panel (a) shows the P-wave velocity obtained through first-break picking, while panel (b) shows the S-wave velocity obtained from the well logs. Both panels show the acquisition geometry with the receivers in black and sources in white.

computational domain with undefined normal vectors. In Figures 5.14(d) and 5.14(e) we remove by dip filtering the steeply dipping migration smiles for better interpretability of the images shown in Figures 5.14(a) and 5.14(b). The low amplitude present in the image difference in Figure 5.14(f) is similar to Figure 5.14(c) where the RSS for both the difference image normalized to the respective reference image is less than 0.02%.

We also test our method through the iterative least-squares method using the formulation outlined in Appendix 5.10.1. Figure 5.15(a) shows the least-squares RTM (LSRTM) image after 5 iterations using the reference source wavefield, while Figure 5.15(b) shows the LSRTM image via source wavefield reconstruction. The amplitude differences between Figures 5.15(a) and 5.15(b) in Figure 5.15(c) are a result of the iterative least-squares process propagating the artifact located around the source. After dip filtering, we arrive at Figures 5.15(d) and 5.15(e) for the corresponding LSRTM images in Figures 5.15(a) and 5.15(b). The difference image is shown in Figure 5.15(f). Figures 5.16(a) and 5.16(b) show the initial data residual for LSRTM using the reference and reconstructed source wavefields, respectively. The equivalent final residuals after 5 iterations of LSRTM are shown in Figures 5.16(c) and 5.16(d). Both final residuals indicate that the least-squares process matches the majority of the arrivals in the data. The more prominent residual for the bottom two reflectors around 2.25 and 3.5 km in depth is due to the weaker amplitude in the modeled DAS response as shown in Figures 5.16(e) and 5.16(f), which can improve with increasing number of iterations.

We perform RTM and LSRTM for the remaining shots (16 total) and stack the images to perform a similar analysis as for the single shot RTM and LSRTM. Figure 5.17(a) shows the energy norm RTM image using the reference source wavefield and Figure 5.17(b) shows the image obtained through source wavefield reconstruction. Note that we apply a poststack amplitude gain with one power of depth to balance the stronger shallow events amplitudes. The corresponding amplitude difference in Figure 5.17(c) is minimal due to the power of stack across multiple shots with the RSS normalized to the reference image approximately 0.01%. We apply the same dip filtering for single shot RTM on every shot to remove the

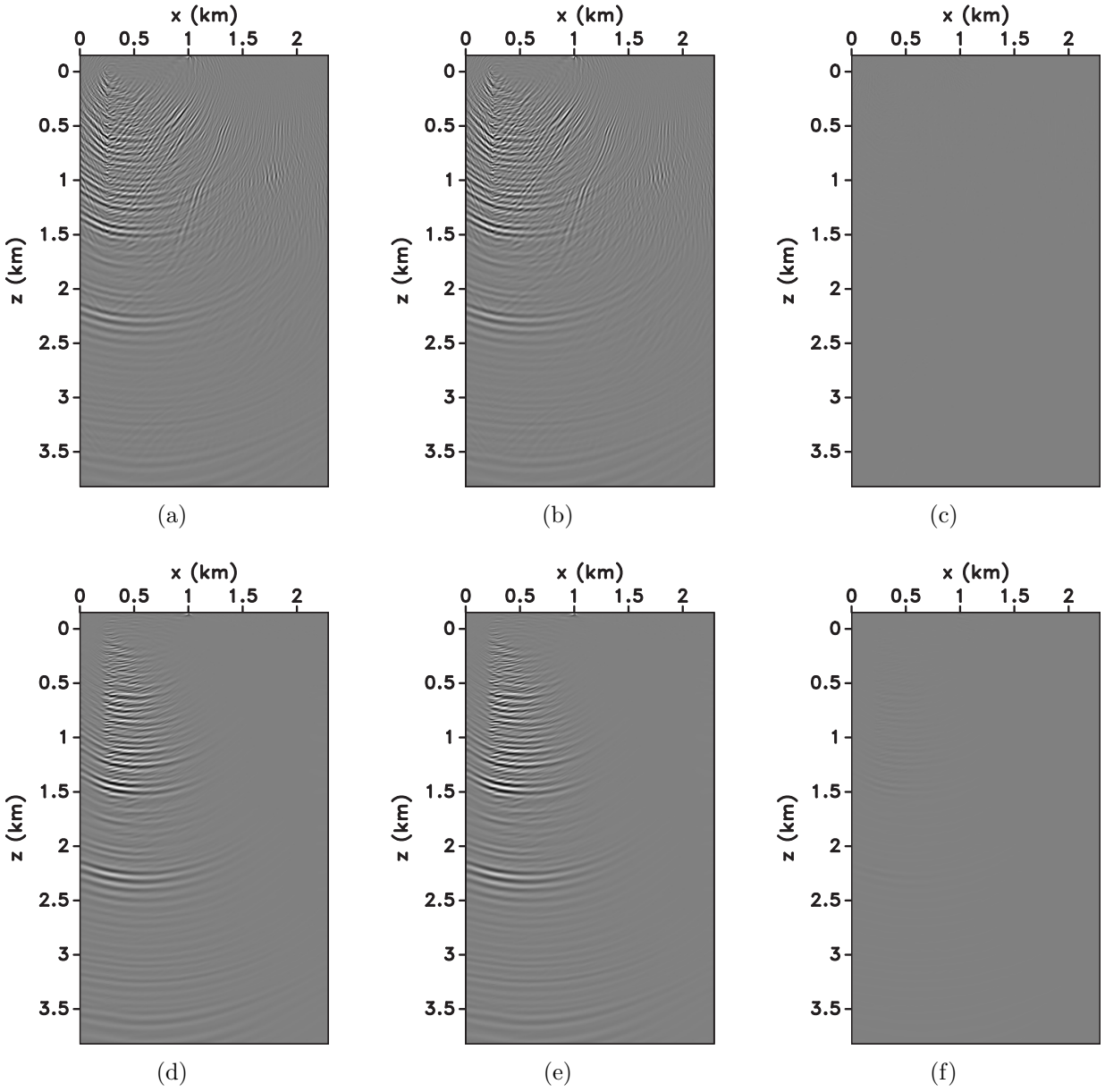

Figure 5.14: Single shot reverse time migration (RTM) image using (a) reference and (b) reconstructed source wavefield. (c) The difference between (a) and (b). (d)-(e) The equivalent images of (a)-(c) after dip filtering.

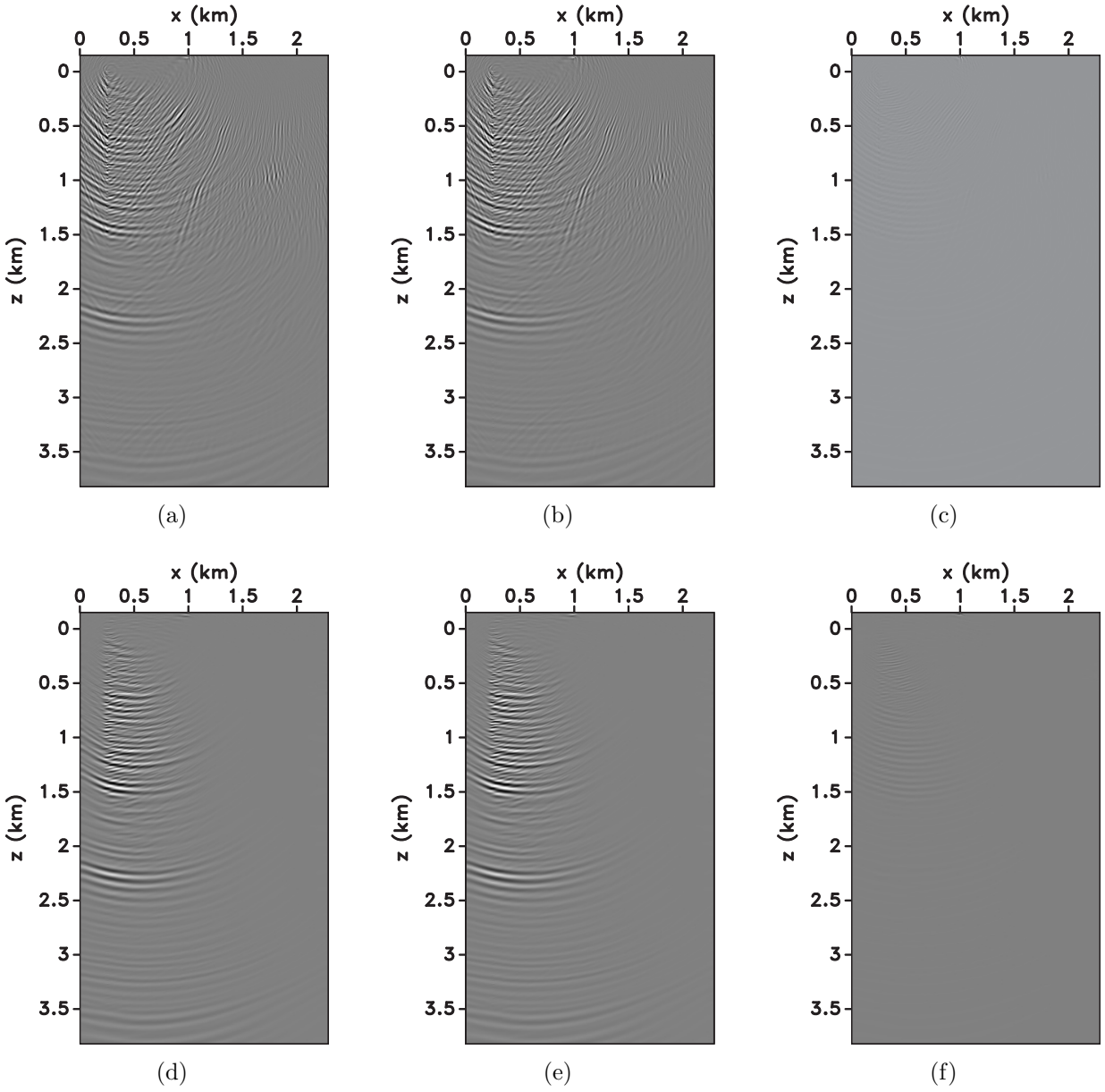

Figure 5.15: Single shot least-squares reverse time migration (LSRTM) image using (a) reference and (b) reconstructed source wavefield. (c) The difference between (a) and (b). (d)-(e) The equivalent images of (a)-(c) after dip filtering.

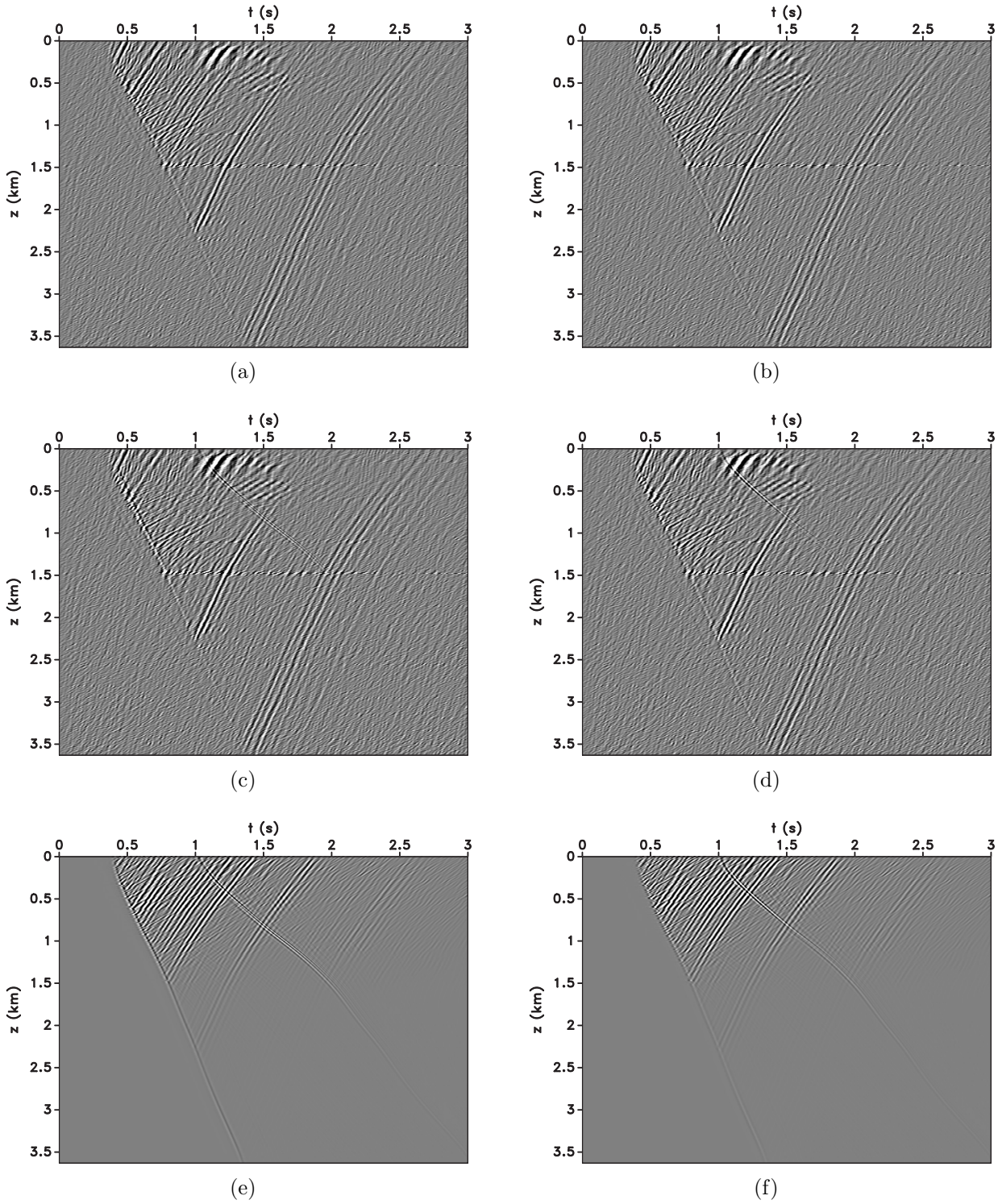

Figure 5.16: Initial data residuals for single shot least-squares reverse time migration (LSRTM) image using (a) reference and (b) reconstructed source wavefield. The final data residuals for the corresponding methods in (c) and (d). The least-squares solution modeled DAS response using (e) reference and (f) reconstructed source wavefield.

migration smiles before stacking and poststack amplitude gain as shown in Figures 5.17(d) and 5.17(e) for the respective images in Figures 5.17(a) and 5.17(b). The low amplitude differences in Figure 5.17(f) is the same as Figure 5.17(c) where the RSS normalized to the reference image approximately 0.005%.

Figures 5.18(a) and 5.18(b) shows the LSRTM for all the shots using the reference and the reconstructed source wavefield. Both of the images are indistinguishable through visual inspection. However, there is a slight amplitude difference as shown in Figure 5.18(c) as a result of stacking coherent amplitude differences among all the shots with an increase of the RSS normalized to the reference image at 2%. Nevertheless, the amplitude differences are minimal and do not affect the interpretability of the final image. The images from dip filtering and poststack amplitude gain are shown in Figures 5.18(d) and 5.18(e) for the respective images in Figures 5.18(a) and 5.18(b). The amplitude difference observations in Figure 5.18(f) is consistent with Figure 5.18(c) with an RRS normalized to the reference image of 2%.

5.7 Discussion

We successfully demonstrate accurate reconstruction of the source wavefield by saving on a single layer on the perimeter of the computational zone in Figure 5.2(a). The elastic RTM images demonstrate that our method through the representation theorem can produce comparable images to the conventional method based on utilizing wavefields stored in the entire domain. Our approach requires that the single boundary layer adequately samples the source wavefield, i.e., the source wavefield needs to propagate out from the computational zone fully. If parts of the source wavefield do not reach the boundary layer, we are unable to reconstruct that particular portion of the source wavefield. Therefore, our method assumes that the source wavefield exits the computational zone which is reasonable. Our iterative LSRTM results also demonstrate that the source wavefield reconstruction method is tantamount to the conservative but costly approach of saving all the wavefields. The introduction of boundaries with well-defined normal vectors such as a superellipse boundary can eradicate

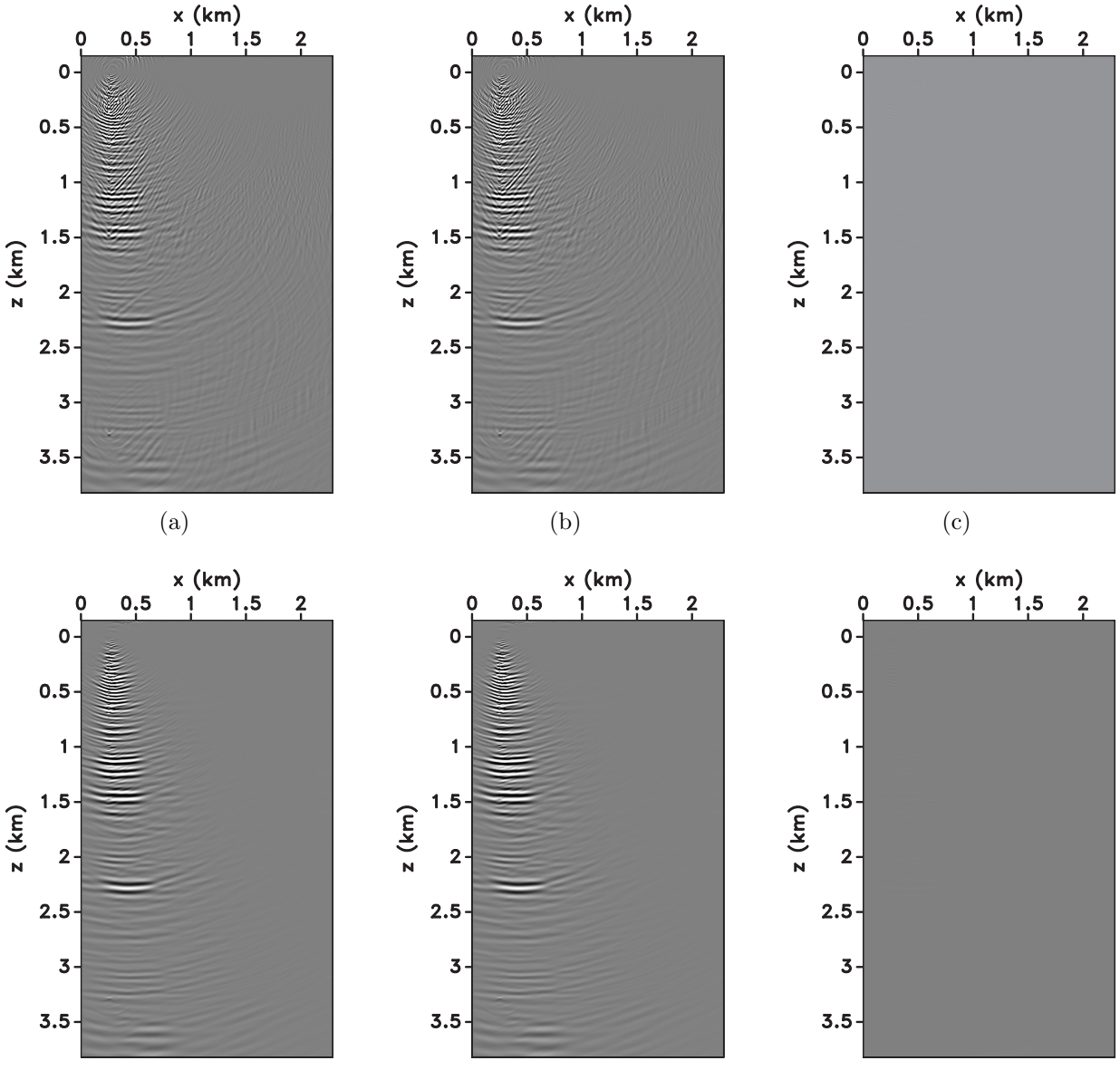

Figure 5.17: All 16 shots reverse time migration (RTM) image using (a) reference and (b) reconstructed source wavefield. (c) The difference between (a) and (b). (d)-(e) The equivalent images of (a)-(c) after dip filtering and poststack amplitude gain with one power of depth.

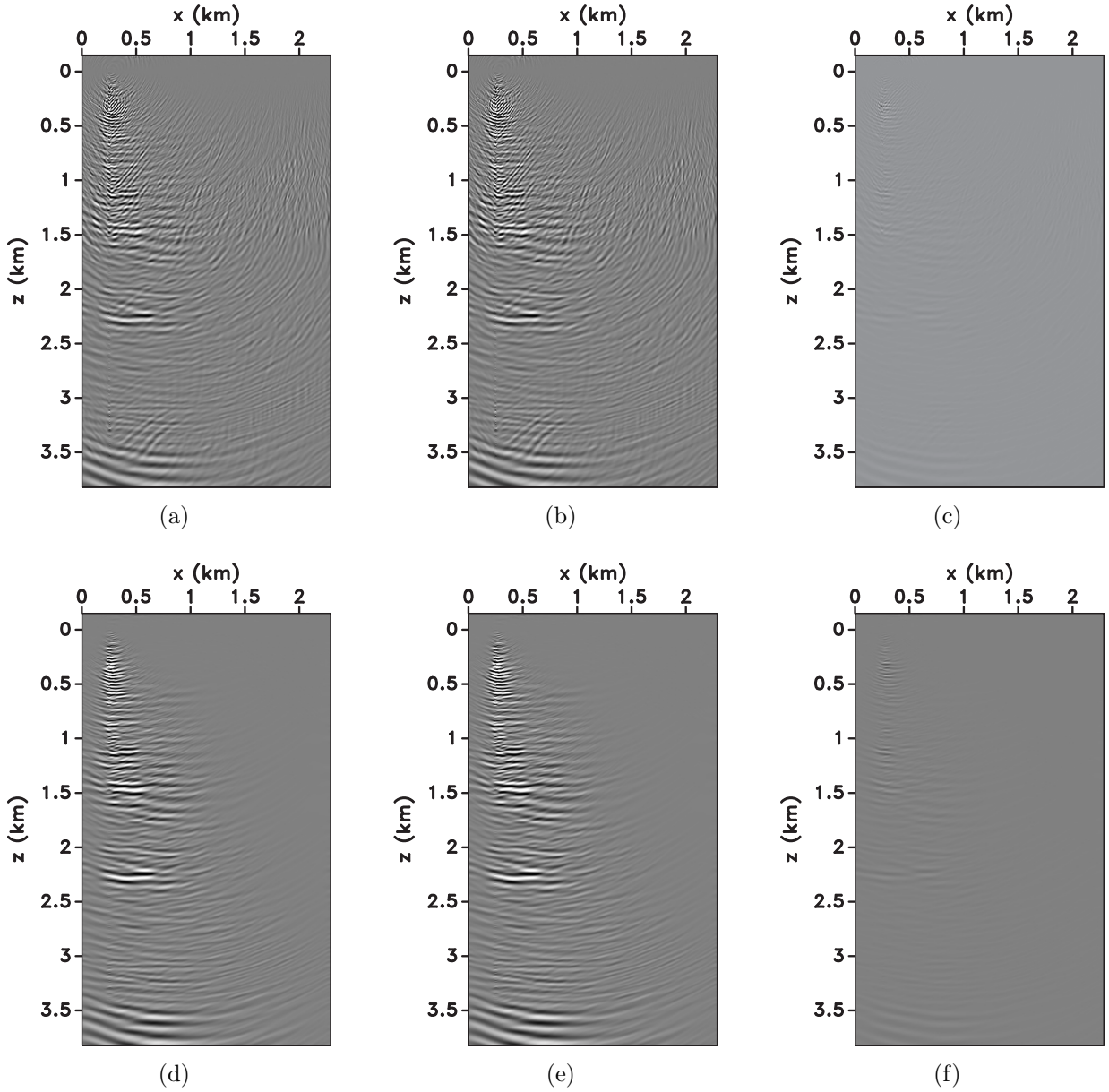

Figure 5.18: All 16 shots least-squares reverse time migration (LSRTM) image using (a) reference and (b) reconstructed source wavefield. (c) The difference between (a) and (b). (d)-(e) The equivalent images of (a)-(c) after dip filtering and poststack amplitude gain with one power of depth.

the artifacts due to the corners of the computational domain.

5.8 Conclusions

We produce both accurate elastic LSRTM and RTM images of the subsurface with source wavefield reconstructed synchronously with the receiver wavefield from data stored in a single layer boundary. Reducing the dimension of the stored source wavefield hypercube dramatically reduces the storage requirements for large 3D imaging problems. Minimal artifacts due to the corners of the computational domain do not impair our ability to image the subsurface accurately and are mostly negligible for most practical applications. Successful demonstration of the method on LSRTM creates opportunities to accelerate other similar costly techniques implementations such as elastic anisotropic full waveform inversion (FWI). The source wavefield reconstruction method presented in this paper applies to media of arbitrary anisotropy and heterogeneity.

5.9 Acknowledgments

We would like to thank the sponsors of the Center for Wave Phenomena, whose support made this research possible. We thank Whitney Schultz and Jim Simmons of the Reservoir Characterization Program (RCP), Colorado School of Mines for processing the Eagle Ford Shale dataset. We are grateful to Devon Energy Corporation for providing access to the Eagle Ford Shale dataset. The reproducible numeric examples in this paper use the Madagascar open-source software package (Fomel et al., 2013) freely available from http://www.ahay.org.

5.10 Appendix

This appendix describes the forward and adjoint operators for least-squares reverse time migration (LSRTM).

5.10.1 Energy norm modeling and migration operators

We modify the potential term of the energy norm imaging condition from Rocha et al. (2017) to obtain the energy image $\mathcal{I}(\mathbf{x})$ which exploits the source wavefield in space $\mathbf{x}$ and time t with both displacement and stress wavefields $\mathbf{w}_s(\mathbf{x},t) = [\mathbf{u}(\mathbf{x},t), \underline{\mathbf{t}}(\mathbf{x},t)]$ together with the receiver wavefield adjoint displacement and strain wavefields $\mathbf{w}_r(\mathbf{x},t) = \left[\mathbf{u}^\dagger(\mathbf{x},t), \underline{\mathbf{e}}^\dagger(\mathbf{x},t)\right]$ as

$$\begin{aligned}
\mathcal{I} &= \sum_t \left(\rho \dot{\mathbf{u}}_s \cdot \dot{\mathbf{u}}_r - \underline{\mathbf{t}}_s \cdot \underline{\mathbf{e}}_r\right) \\
&= \left(\begin{bmatrix} \rho^{1/2}\mathbf{B} & 0 \\ 0 & \mathbf{I} \end{bmatrix} \begin{bmatrix} \mathbf{u}_s \\ \underline{\mathbf{t}}_s \end{bmatrix}\right)^\intercal \begin{bmatrix} \rho^{1/2}\mathbf{B} & 0 \\ 0 & \mathbf{I} \end{bmatrix} \begin{bmatrix} \mathbf{u}_r \\ -\underline{\mathbf{e}}_r \end{bmatrix} \\
&= (\square \mathbf{w}_s)^\intercal \square \mathbf{w}_r \\
&= (\square^\intercal \square \mathbf{w}_s)^\intercal \mathbf{w}_r \\
&= \mathbf{E}^\intercal \mathbf{w}_r \,,
\end{aligned} \tag{5.7}$$

where $\rho(\mathbf{x})$ is the density and $\mathbf{B}$ denotes the time derivative operator. $\mathbf{E}^\intercal$ and $\mathbf{E}$ represent the energy norm migration and demigration operators. Following the linearized elastic wave formulation in Appendix 5.10.2, we use the following expressions for brevity:

$$\begin{aligned}
\mathbf{L}\mathbf{w} &= \mathbf{p} \\
\mathbf{w} &= \mathbf{L}^{-1}\mathbf{p} \\
\mathbf{w} &= \mathbf{G}\mathbf{p} \,,
\end{aligned} \tag{5.8}$$

where $\mathbf{G}$ is the forward modeling operator for wavefield $\mathbf{w}$ using the input wavefield $\mathbf{p}$. The adjoint operator $\mathbf{G}^\intercal$ represents the backward modeling operator for wavefield $\mathbf{p}$ using the input wavefield $\mathbf{w}$. We introduce the forward operator $\mathbf{K}$ to extract the wavefield and the adjoint operator $\mathbf{K}^\intercal$ to inject data at known locations:

$$\mathbf{K}\mathbf{w} = \mathbf{d} \,. \tag{5.9}$$

We express the entire demigration process from the energy norm image $\mathcal{I}(\mathbf{x})$ to the receivers $\mathbf{d}_r(\mathbf{x},t)$ as a series of cascading operators:

$$\begin{aligned}
\mathcal{I} &= \mathbf{E}^\intercal \mathbf{w}_r \\
&= \mathbf{E}^\intercal \mathbf{G}^\intercal \mathbf{K}^\intercal \mathbf{d}_r \\
&= \mathbf{L}^\intercal \mathbf{d}_r \\
\mathbf{L}\,\mathcal{I} &= \mathbf{d}_r \,,
\end{aligned} \tag{5.10}$$

where the migration cascade operator $\mathbf{L}^\intercal$ injects the receiver data $\mathbf{d}_r\,(\mathbf{x},t)$ through operator $\mathbf{K}^\intercal$ to allow operator $\mathbf{G}^\intercal$ to backward extrapolate the receiver wavefield. Operator $\mathbf{E}^\intercal$ performs the energy imaging condition to generate the final image $\mathcal{I}\,(\mathbf{x})$. The forward operator $\mathbf{L}$ demigrates the energy image to generate data at the receiver locations. To mimic the single component distributed acoustic sensing (DAS) strain measurements, we introduce a compliance operator $\mathbf{S}$ that converts the stress outputs to strain and a windowing operator $\mathbf{W}$ to restrict the output to a single component:

$$\mathbf{W}\,\mathbf{S}\,\mathbf{L}\,\mathcal{I} = \mathbf{d}_r\,. \tag{5.11}$$

The corresponding DAS migration (adjoint) operation is

$$\mathbf{L}^\intercal\mathbf{S}^\intercal\mathbf{W}^\intercal\mathbf{d}_r = \mathcal{I}\,. \tag{5.12}$$

5.10.2 Linearized elastic wave modeling operator

We describe the forward wavefield extrapolation using the elastic-wave propagation through the second-order partial differential equations consisting of both stress $\underline{\mathbf{t}}\,(\mathbf{x},t)$ and particle displacement $\mathbf{u}\,(\mathbf{x},t)$ wavefields (Aki and Richards, 2002)

$$\rho\,\frac{\partial^2\mathbf{u}}{\partial t^2} = \mathbf{D}\,\underline{\mathbf{t}} + \mathbf{f}\,, \tag{5.13}$$

where $\mathbf{D}$ and $\mathbf{f}\,(\mathbf{x},t)$ denote the divergence operator and external volume force, respectively. Under the assumption of linear elasticity the stress $\underline{\mathbf{t}}\,(\mathbf{x},t)$ is related to strain $\underline{\mathbf{e}}\,(\mathbf{x},t)$ through the constitutive relation

$$\underline{\mathbf{t}} = \underline{\underline{\mathbf{c}}}\,\underline{\mathbf{e}} + \underline{\mathbf{m}}\,, \tag{5.14}$$

where $\underline{\mathbf{m}}\,(\mathbf{x},t)$ is the seismic moment tensor source acting as stress perturbation. The relation between the strain $\underline{\mathbf{e}}\,(\mathbf{x},t)$ tensor and particle displacement $\mathbf{u}\,(\mathbf{x},t)$ is

$$\begin{aligned}\underline{\mathbf{e}} &= \frac{1}{2}\,[\,\nabla\mathbf{u} + (\nabla\mathbf{u})^\intercal\,]\\ &= \mathbf{H}\,\mathbf{u}\,,\end{aligned} \tag{5.15}$$

where the operator $\mathbf{H}$ captures the geometric relation between strain and particle displacement. We solve equations 5.13 and 5.14 using the finite-difference representation of the

time-derivative leading to the recursive relations for stress

$$\underline{\mathbf{t}} = \underline{\underline{\mathbf{c}}}\,\mathbf{H}\,\mathbf{u} + \underline{\mathbf{m}} \tag{5.16}$$

and particle displacement

$$\mathbf{u}_{+} = 2\mathbf{u} + \frac{\Delta t^2}{\rho}\left(\mathbf{D}\,\underline{\mathbf{t}} + \mathbf{f}\right) - \mathbf{u}_{-}\,. \tag{5.17}$$

These recursive equations allow us to compute the subsequent time wavefield $\mathbf{u}_{+}$ from wavefields at the current time $\mathbf{u}$ and at preceding time $\mathbf{u}_{-}$. In matrix form, we express the recurrent equations 5.16 and 5.17 as

$$\left[\begin{array}{c|cccc} \mathbf{I} & -\underline{\underline{\mathbf{c}}}\,\mathbf{H} & & & \\ \hline & -\frac{2\rho}{\Delta t^2} & \frac{\rho}{\Delta t^2} & 0 & \cdots \\ & \frac{\rho}{\Delta t^2} & -\frac{2\rho}{\Delta t^2} & \frac{\rho}{\Delta t^2} & \cdots \\ -\mathbf{D} & 0 & \frac{\rho}{\Delta t^2} & -\frac{2\rho}{\Delta t^2} & \cdots \\ & \vdots & \vdots & \vdots & \ddots \end{array}\right] \left[\begin{array}{c} \underline{\mathbf{t}}_0 \\ \underline{\mathbf{t}}_1 \\ \underline{\mathbf{t}}_2 \\ \vdots \\ \hline \mathbf{u}_0 \\ \mathbf{u}_1 \\ \mathbf{u}_2 \\ \vdots \end{array}\right] = \left[\begin{array}{c} \underline{\mathbf{m}}_0 \\ \underline{\mathbf{m}}_1 \\ \underline{\mathbf{m}}_2 \\ \vdots \\ \hline \mathbf{f}_0 \\ \mathbf{f}_1 \\ \mathbf{f}_2 \\ \vdots \end{array}\right] \tag{5.18}$$

where $\underline{\mathbf{m}}\,(\mathbf{x},t)$ and $\mathbf{f}\,(\mathbf{x},t)$ are the input wavefields, i.e., the source, and $\underline{\mathbf{t}}\,(\mathbf{x},t)$ and $\mathbf{u}\,(\mathbf{x},t)$ are propagating wavefields. We solve for $\underline{\mathbf{t}}\,(\mathbf{x},t)$ and $\mathbf{u}\,(\mathbf{x},t)$ from the top, i.e., forward in time, using the moment tensor and the body force sources. The forward operator takes an external force wavefield $\mathbf{p}\,(\mathbf{x},t) = [\underline{\mathbf{m}}\,(\mathbf{x},t)\,,\mathbf{f}\,(\mathbf{x},t)]$ and generates the source wavefield $\mathbf{w}\,(\mathbf{x},t) = [\underline{\mathbf{t}}\,(\mathbf{x},t)\,,\mathbf{u}\,(\mathbf{x},t)]$ by propagating forward in time:

$$\mathbf{L}\mathbf{w} = \mathbf{p}\,. \tag{5.19}$$

The adjoint operator takes the wavefield $\mathbf{w}\,(\mathbf{x},t) = [\underline{\mathbf{t}}\,(\mathbf{x},t)\,,\mathbf{u}\,(\mathbf{x},t)]$ and generates the adjoint wavefield $\mathbf{p}\,(\mathbf{x},t) = [\underline{\mathbf{m}}\,(\mathbf{x},t)\,,\mathbf{f}\,(\mathbf{x},t)]$ by propagating backward in time:

$$\mathbf{w} = \mathbf{L}^{\intercal}\mathbf{p}\,. \tag{5.20}$$

In matrix form, we can write equation 5.20 as

$$\left[\begin{array}{c|cccc} \mathbf{I} & -\mathbf{D}^\dagger & & & \\ \hline & -\frac{2\rho}{\Delta t^2} & \frac{\rho}{\Delta t^2} & 0 & \cdots \\ & \frac{\rho}{\Delta t^2} & -\frac{2\rho}{\Delta t^2} & \frac{\rho}{\Delta t^2} & \cdots \\ -\mathbf{H}^\dagger\,\underline{\underline{\mathbf{c}}} & 0 & \frac{\rho}{\Delta t^2} & -\frac{2\rho}{\Delta t^2} & \cdots \\ & \vdots & \vdots & \vdots & \ddots \end{array}\right] \left[\begin{array}{c} \underline{\mathbf{m}}_0 \\ \underline{\mathbf{m}}_1 \\ \underline{\mathbf{m}}_2 \\ \vdots \\ \hline \mathbf{f}_0 \\ \mathbf{f}_1 \\ \mathbf{f}_2 \\ \vdots \end{array}\right] = \left[\begin{array}{c} \underline{\mathbf{t}}_0 \\ \underline{\mathbf{t}}_1 \\ \underline{\mathbf{t}}_2 \\ \vdots \\ \hline \mathbf{u}_0 \\ \mathbf{u}_1 \\ \mathbf{u}_2 \\ \vdots \end{array}\right] . \tag{5.21}$$

We solve for $\underline{\mathbf{m}}$ and $\mathbf{f}$ from the bottom, i.e., backward in time, using the sources $\underline{\mathbf{t}}$ and $\mathbf{u}$. The time reversal iterative equation for the adjoint strain is

$$\underline{\mathbf{m}} = \mathbf{D}^\dagger\,\mathbf{f} + \underline{\mathbf{t}} \tag{5.22}$$

and the adjoint particle displacement is

$$\mathbf{f}_- = 2\mathbf{f} + \frac{\Delta t^2}{\rho}\left(\mathbf{H}^\dagger\,\underline{\underline{\mathbf{c}}}\,\underline{\mathbf{m}} + \mathbf{u}\right) - \mathbf{f}_+ . \tag{5.23}$$

CHAPTER 6

CONCLUSIONS

In this thesis, I develop new seismic acquisition configurations for distributed acoustic sensing (DAS) that enable observation of the full strain tensor. The general design I propose for multicomponent DAS acquisition can identify optimal fiber geometry parameters without assumptions about the medium parameters. I present a simple design in **Chapter 2**, where I demonstrate that the potential for multicomponent distributed acoustic sensing of the full strain tensor through sequential strain projections along purposefully built optical fibers. Clustering recordings within a section of the fiber and assuming local invariance allows for analytic reconstruction of the complete strain tensor. I present multiple configurations that achieve diverse projections, including, but not limited to a chirping helical optical fiber and combinations of helical and straight optical fibers. However, the chirping helix geometry is both challenging and laborious to manufacture and deploy. Nonetheless, the necessary condition for accurate reconstruction is that the seismic wavelength of interest be greater than the acquisition section, which limits widespread implementation of such configurations due to its implied low frequency. It is worth mentioning that such configurations have a higher likelihood of success with teleseismic events which naturally have larger wavelengths.

In **Chapter 3**, I overcome the resolution limitations of the preceding design by using individual strain projections recorded along several specially designed optical fibers that lead to the measurement of high resolution multicomponent distributed acoustic sensing. I demonstrate that the entire strain tensor can be reconstructed at every point with five equally spaced helical optical fibers, together with a straight optical fiber. This achievement allows for data recording of arbitrary wavelength in applications such as seismic imaging, and reservoir characterization, but would also work for teleseismic or geotechnical applications. The analysis in my thesis shows that a short gauge length plays a significant role in the

accuracy of the strain tensor reconstruction, especially in the presence of noise. Systems with short gauge length are possible with specially engineered optical fiber in combination with the rapidly evolving DAS interrogator technology. Even using current technology, increasing the diameter of the proposed configurations when the dimension of the optical fiber cable is not restricted, such as for surface seismic acquisition, allows for the use of longer gauge lengths. Nevertheless, as shown in my analysis, careful selection of the design parameters through parameter scanning is necessary to ensure accurate reconstruction. Future work on **Chapters 2** and **3** involves manufacturing and field testing of the proposed optical fiber configuration.

In **Chapter 4**, I develop a generalized seismic source mechanisms imaging method that incorporates the new multicomponent DAS data and uses both vector and tensor measurements to produce images of body force and/or moment tensor sources. Since the resulting images correspond directly to the respective components of the sources, this imaging technology provides direct access to the theoretical representation of seismic source mechanisms. Although my method can handle both vector and tensor measurements, in the absences of either data the formulation reduces to special cases previously discussed in the literature. I demonstrate the robustness of this wavefield-based method through field data example with smooth models. Identifying the seismic source mechanism through this imaging method enables near real-time decision-making and hazard early warning. I also demonstrate the ability to improve image resolution by removing the imaging point spread function through least-squares processing. The results can be further improved by deploying arrays of multicomponent DAS acquisition technology discussed in **Chapters 2** and **3** to obtain the full strain data for accurate receiver wavefield extrapolation via the representation theorem. In the absences of the strain tensor, the inexact wavefield extrapolation introduces nonphysical wave modes that generate artifacts in the final images, but can be lessened by the least-squares method.

Building on the representation theorem, **Chapter 5** shows computational acceleration for wavefield-based applications such as reverse time migration (RTM) by accurate source wavefield reconstruction synchronously with the receiver wavefield from a single layer computational boundary. By holding minimal data in memory and eliminating the need for permanent computer storage, the reconstruction technique can mitigate the risk of I/O bottlenecks where data transactions could not keep up with requests from the processor. This is especially relevant for large 3D applications where the source wavefield represents a spatio-temporal 4D unit hypercube (also known as a unit tesseract). Due to the cuboid nature of the finite difference computational grid, the reconstruction from abrupt changes at vertices generates artifacts. However, my numerical examples show that the artifacts are negligible for most practical applications. Introducing a geometry with smooth transitioning vertices such as a superellipsoid can abate the artifacts. I demonstrate this technique with LSRTM, but highlight that the same method can be used for more computationally intensive algorithms like full waveform inversion (FWI).

All the methodology presented in this thesis apply to elastic media of arbitrary anisotropy and heterogeneity. Although I have explicitly chosen to focus on seismic imaging for the applications of multicomponent DAS data, the new acquisition technology discussed in this thesis has bountiful potential in areas outside of geophysics, such as infrastructure health monitoring and global seismology.

6.1 Limitations and opportunities

The gauge length remains a significant hurdle to overcome. The success of strain tensor reconstruction is higher with smaller gauge lengths when DAS measurements converge to point observations. In **Chapters 2** and **3**, I demonstrate successful reconstruction of the strain tensor using currently available DAS systems, which are capable of data acquisition down to gauge length of 1 m. However, the present day DAS technology acquires data with signal-to-noise (SNR) that improves with increasing gauge length. Therefore, it is paramount for the advancement of the DAS interrogation technology to reduce the gauge length while

maintaining geophone-like SNR for widespread application of multicomponent DAS. Despite the need for DAS hardware advancements, this also poses a new research opportunity to perform better reconstruction with large gauge lengths by introducing a regularization term during the inversion process. An example of regularization term implementation such as enforcing smooth solutions is desirable, since strain tensor signals without aliasing are never abruptly changing. The approach of weighted least-squares inversion can suppress instabilities due to short gauge length acquisitions with low SNR and geometry deployment uncertainty.

The work I present in **Chapters 2** and **3** assumes the geometry of helical optical fibers wrapped along a straight cable. This assumption simplifies the multiparameter analysis where the helix wrapping angle remains constant along the cable. Figure 6.1(a) demonstrates a constant wrapping angle at 30° along a straight axis, whereas Figure 6.1(b) illustrates the same helix along a curved axis. The departure of the wrapping angle from the nominal 30° is most noticeable at the point of greatest curvature. Deployment of multicomponent DAS for geometries such as a deviated well requires additional analysis to ensure successful reconstruction of the full strain tensor.

Seismic wavefield work presents in the form of strain energy. The ability to release the transferred strain energy allows elastic media to return to its original state. Through multicomponent DAS, a new research opportunity exists in the area of structural health monitoring which can benefit from the measurement of strain energy for potential hazards and risks assessments, especially after significant events such as an earthquake. The analysis enables engineers to focus remedial efforts on sections subject to the largest accumulated strain energy. The total strain energy can be expressed as (Sadd, 2009)

$$\mathbf{E} = \frac{\mathbf{1}}{\mathbf{2}} \underline{\mathbf{e}}\, \underline{\mathbf{t}}\ , \tag{6.1}$$

where $\underline{\mathbf{e}}$ represents the strain tensor and $\underline{\mathbf{t}}$ denotes the stress tensor. To highlight the significances of such measurement for future research, I perform a regional scale earthquake simulation in Southern California (SoCal) with the model CVM-S4.26 (Lee et al., 2014) and

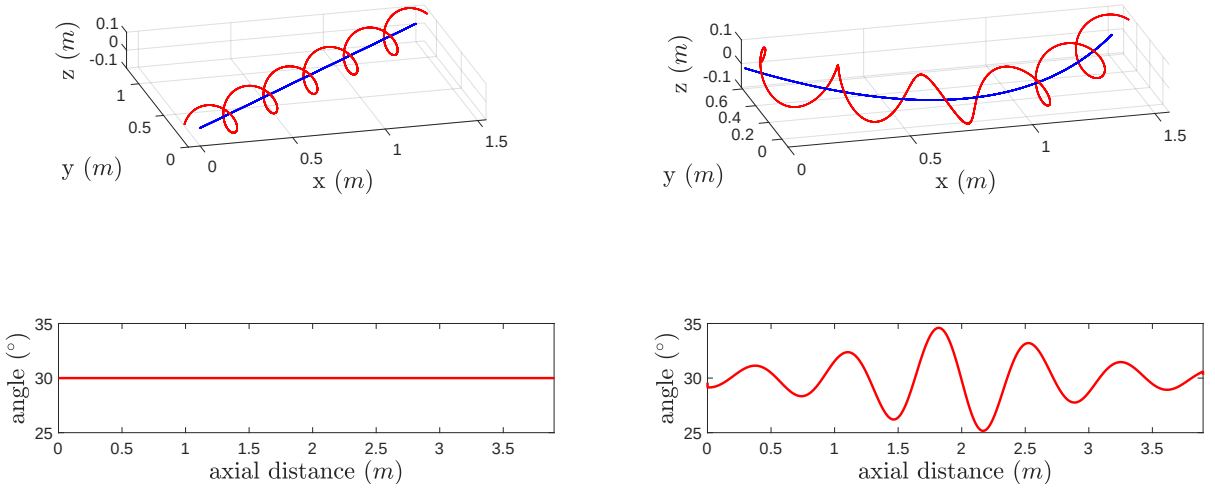

Figure 6.1: (a) The top panel shows a helical optical fiber wrapped along a straight axis, where the bottom panel shows the wrapping angle as a function of the axial distance. (b) The analogous figure for a helical optical fiber wrapped along a curved axis.

elevation map obtained from the Southern California Earthquake Center (SCEC) unified community velocity model (UCVM) software framework (Small et al., 2017). Figures 6.2(a), 6.2(b), and 6.2(c) show the respective compressional, shear, and density model. The event underlying my simulation is the 1991 magnitude 5.8 Sierra Madre earthquake. The event occurred underneath the San Gabriel Mountains that result in total damage of approximately $40 million (Hauksson, 1994). Figure 6.2(d) illustrates the earthquake location in red and the potential deployment of multicomponent DAS systems in white. Figure 6.3(a) shows a snapshot of the wavefield simulation using the SPECFEM3D Cartesian software (Komatitsch and Vilotte, 1998; Komatitsch and Tromp, 2002a,b). To determine the total strain energy, I measure the strain tensor using multicomponent DAS, and under the assumption that the surrounding stiffness tensor is known, I estimate the stress tensor in Equation 6.1 assuming linear elasticity. Figure 6.3(b) shows the total strain energy over the duration of the earthquake simulation where the bright colors indicate high strain energy.

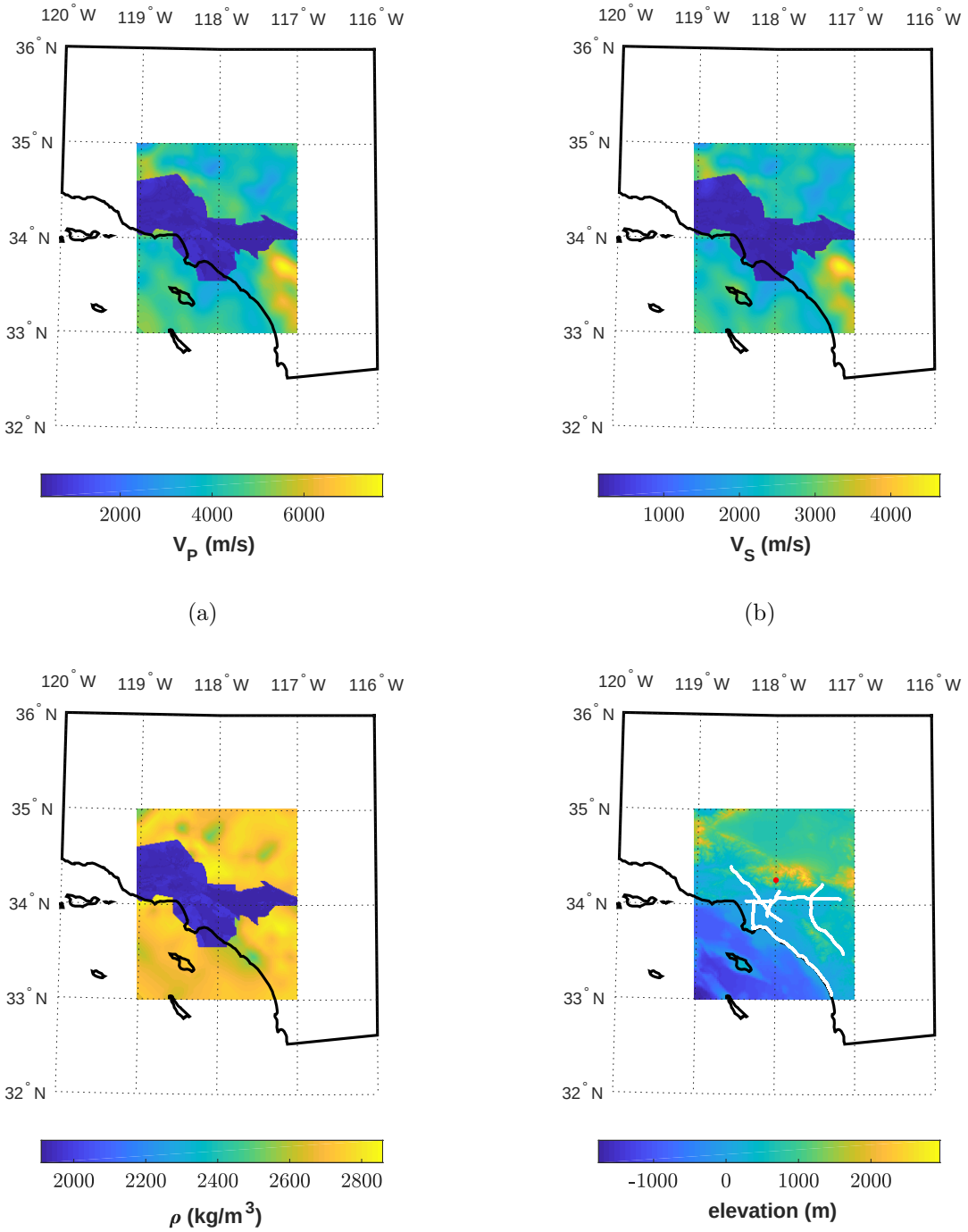

Figure 6.2: The Southern California model for the (a) P- and (b) S-wave velocities, and the (c) density from the CVM-S4.26 model (Lee et al., 2014). (d) The surface elevation together with white lines representing potential deployment of multicomponent DAS along the interstate and state highway system of Southern California. The 1991 Sierra Madre earthquake location shown in red.

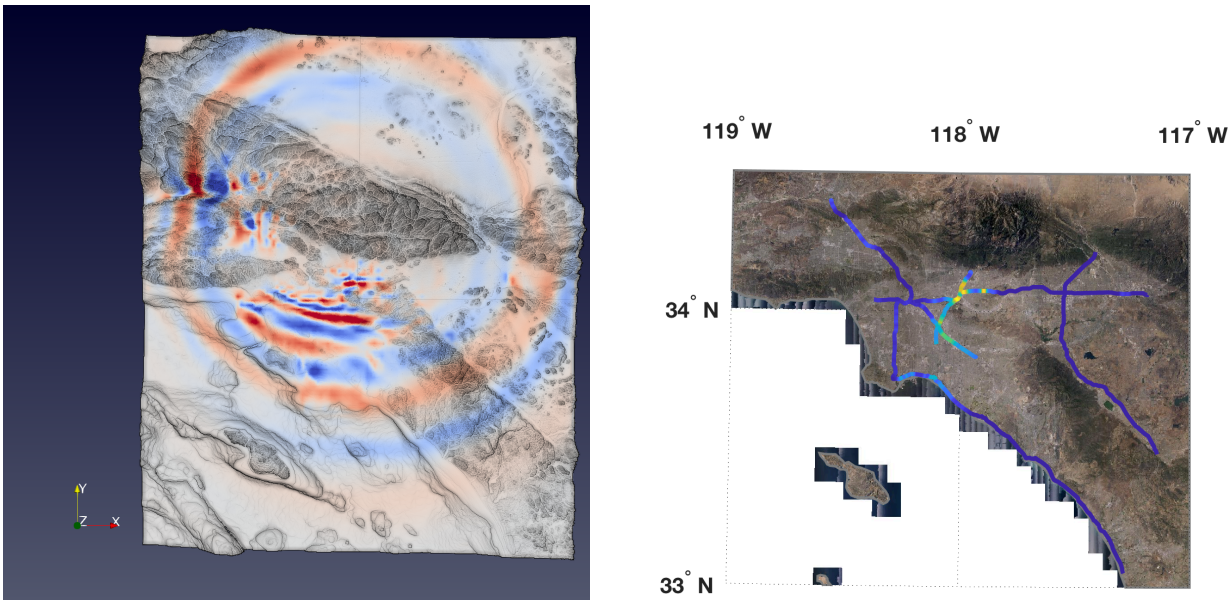

(a) (b)

Figure 6.3: (a) A simulation snapshot of the seismic wavefield due to the 1991 Sierra Madre earthquake. (b) The total strain energy (bright colors denote high intensity) obtained using multicomponent DAS overlaid on the Southern California map (U.S. Geological Survey, National Geospatial Program).

REFERENCES CITED

Agnew, D. C., 1986, Strainmeters and tiltmeters: Reviews of Geophysics, **24**, 579–624.

Aki, K., and P. G. Richards, 2002, Quantitative seismology, 2nd ed.: University Science Books.

Anderson, J. E., L. Tan, and D. Wang, 2012, Time-reversal checkpointing methods for RTM and FWI: Geophysics, **77**, S93–S103.

Artman, B., I. Podladtchikov, and B. Witten, 2010, Source location using time-reverse imaging: Geophysical Prospecting, **58**, 861–873.

Baig, A., and T. Urbancic, 2010, Microseismic moment tensors: A path to understanding frac growth: The Leading Edge, **29**, 320–324.

Bakku, S. K., 2015, Fracture characterization from seismic measurements in a borehole: PhD thesis, Massachusetts Institute of Technology.

Barak, O., F. Herkenhoff, R. Dash, P. Jaiswal, J. Giles, S. de Ridder, R. Brune, and S. Ronen, 2014, Six-component seismic land data acquired with geophones and rotation sensors: Wave-mode selectivity by application of multicomponent polarization filtering: The Leading Edge, **33**, 1224–1232.

Barak, O., K. Key, S. Constable, and S. Ronen, 2018, Recording active-seismic ground rotations using induction-coil magnetometers: Geophysics, **83**, P19–P42.

Bazargani, F., and R. Snieder, 2015, Optimal source imaging in elastic media: Geophysical Journal International, **204**, 1134–1147.

Bo, F., and W. Huazhong, 2011, Reverse time migration with source wavefield reconstruction strategy: Journal of Geophysics and Engineering, **9**, 69.

Bourgeois, A., M. Bourget, P. Lailly, M. Poulet, P. Ricarte, and R. Versteeg, 1991, Marmousi, model and data: Presented at the 1990 EAGE workshop on Practical Aspects of Seismic Data Inversion.

Carlson, D., A. Long, W. Söllner, H. Tabti, R. Tenghamn, and N. Lunde, 2007, Increased resolution and penetration from a towed dual-sensor streamer: First Break, **25**.

Castongia, E., H. F. Wang, N. Lord, D. Fratta, M. Mondanos, and A. Chalari, 2017, An experimental investigation of distributed acoustic sensing (DAS) on lake ice: Journal of Environmental and Engineering Geophysics, **22**, 167–176.

Chalenski, D., M. Tatanova, Y. Du, A. Mateeva, J. Lopez, and H. Potters, 2016, Climbing the staircase of ultralow-cost 4D monitoring of deepwater fields using DAS-VSP: 86th Annual International Meeting, SEG, Expanded Abstracts, 5441–5445.

Chambers, K., B. D. Dando, G. A. Jones, R. Velasco, and S. A. Wilson, 2014, Moment tensor migration imaging: Geophysical Prospecting, **62**, 879–896.

Clapp, R. G., 2009, Reverse time migration with random boundaries: 79th Annual International Meeting, SEG, Expanded Abstracts, 2809–2813.

Cochard, A., H. Igel, B. Schuberth, W. Suryanto, A. Velikoseltsev, U. Schreiber, J. Wassermann, F. Scherbaum, and D. Vollmer, 2006, Rotational motions in seismology: theory, observation, simulation, *in* Earthquake source asymmetry, structural media and rotation effects: Springer, 391–411.

Cox, B., P. Wills, D. Kiyashchenko, J. Mestayer, J. Lopez, S. Bourne, R. Lupton, G. Solano, N. Henderson, D. Hill, et al., 2012, Distributed acoustic sensing for geophysical measurement, monitoring and verification: CSEG Recorder, **37**, 7–13.

Crickmore, R., and D. Hill, 2014, Fibre optic cable for acoustic/seismic sensing: WO Patent App. PCT/GB2013/052, 795.

Daley, T. M., B. M. Freifeld, J. Ajo-Franklin, S. Dou, R. Pevzner, V. Shulakova, S. Kashikar, D. E. Miller, J. Goetz, J. Henninges, et al., 2013, Field testing of fiber-optic distributed acoustic sensing (DAS) for subsurface seismic monitoring: The Leading Edge, **32**, 699–706.

Davis, T. L., M. J. Terrell, R. D. Benson, R. Cardona, R. R. Kendall, and R. Winarsky, 2003, Multicomponent seismic characterization and monitoring of the CO_2 flood at Weyburn Field, Saskatchewan: The Leading Edge, **22**, 696–697.

Day, A., T. Klüver, W. Söllner, H. Tabti, and D. Carlson, 2013, Wavefield-separation methods for dual-sensor towed-streamer data: Geophysics, **78**, WA55–WA70.

Dean, T., T. Cuny, and A. H. Hartog, 2017, The effect of gauge length on axially incident p-waves measured using fibre optic distributed vibration sensing: Geophysical Prospecting, **65**, 184–193.

den Boer, J., J. Koelman, J. Pearce, A. Franzen, P. LUMENS, and D. Joinson, 2012, Fiber optic cable with increased directional sensitivity. (WO Patent App. PCT/US2012/042,919).

den Boer, J., A. Mateeva, J. Pearce, J. Mestayer, W. Birch, J. Lopez, K. Hornman, and B. Kuvshinov, 2013, Detecting broadside acoustic signals with a fiber optical Distributed Acoustic Sensing (DAS) assembly. (WO Patent App. PCT/US2012/069,464).

Dou, S., J. Ajo-Franklin, T. Daley, M. Robertson, T. Wood, B. Freifeld, R. Pevzner, J. Correa, K. Tertyshnikov, M. Urosevic, and B. Gurevich, 2016, Surface orbital vibrator (SOV) and fiber-optic DAS: Field demonstration of economical, continuous-land seismic time-lapse monitoring from the Australian CO2CRC Otway site: 86th Annual International Meeting, SEG, Expanded Abstracts, 5552–5556.

Duan, Y., 2016, Elastic wavefield migration and tomography: PhD thesis, Colorado School of Mines.

Dussaud, E., W. W. Symes, P. Williamson, L. Lemaistre, P. Singer, B. Denel, and A. Cherrett, 2008, Computational strategies for reverse-time migration: 78th Annual International Meeting, SEG, Expanded Abstracts, 2267–2271.

Farhadiroushan, M., D. Finfer, D. Strusevich, S. Shatalin, and T. Parker, 2015, Non-isotropic acoustic cable: WO Patent App. PCT/GB2014/052, 679.

Farhadiroushan, M., T. Parker, and S. Shatalin, 2016, Method and apparatus for optical sensing: WO Patent App. PCT/GB2016/050, 625.

Fomel, S., P. Sava, I. Vlad, Y. Liu, and V. Bashkardin, 2013, Madagascar: open-source software project for multidimensional data analysis and reproducible computational experiments: Journal of Open Research Software, **1**.

Fukahata, Y., Y. Yagi, and L. Rivera, 2013, Theoretical relationship between back-projection imaging and classical linear inverse solutions: Geophysical Journal International, **196**, 552–559.

Gangi, A. F., 1970, A derivation of the seismic representation theorem using seismic reciprocity: Journal of Geophysical Research, **75**, 2088–2095.

Gharti, H. N., V. Oye, D. Kühn, P. Zha, et al., 2011, Simultaneous microearthquake location and moment-tensor estimation using time-reversal imaging: 81st Annual International Meeting, SEG, Expanded Abstracts, 1632–1637.

González, Á., 2010, Measurement of areas on a sphere using Fibonacci and latitude–longitude lattices: Mathematical Geosciences, **42**, 49.

Hartog, A., 2000, Distributed fiber-optic sensors: principles and applications, *in* Optical Fiber Sensor Technology: Springer, 241–301.

Hartog, A., J. Martin, D. Donno, and B. Papp, 2014, Fiber optic distributed vibration sensing with directional sensitivity: WO Patent App. PCT/US2014/042, 226.

Hauksson, E., 1994, The 1991 Sierra Madre earthquake sequence in southern California: Seismological and tectonic analysis: Bulletin of the Seismological Society of America, **84**, 1058–1074.

Hornman, J., 2017, Field trial of seismic recording using distributed acoustic sensing with broadside sensitive fibre-optic cables: Geophysical Prospecting, **65**, 35–46.

Hornman, J., A. Mateeva, J. Potters, and J. Lopez, 2015, New concepts for lowering the cost of frequent seismic reservoir monitoring onshore: 85th Annual International Meeting, SEG, Expanded Abstracts, 5518–5522.

Igel, H., M. Bernauer, J. Wassermann, and K. Schreiber, 2015, Rotational seismology: Theory, instrumentation, observations, applications: Encyclopedia of complexity and systems science: Springer Verlag Berlin/Heidelberg, 1–26.

Jarillo Michel, O., and I. Tsvankin, 2014, Gradient calculation for waveform inversion of microseismic data in VTI media: Journal of Seismic Exploration, **23**, 201–207.

———, 2015, Estimation of microseismic source parameters by 2D anisotropic waveform inversion: Journal of Seismic Exploration, **24**, no. 5, 379–400.

———, 2017, Waveform inversion for microseismic velocity analysis and event location in VTI media: Geophysics, **82**, WA95–WA103.

Jia, X., and L. Yang, 2017, A memory-efficient staining algorithm in 3D seismic modelling and imaging: Journal of Applied Geophysics, **143**, 62–73.

Jiang, T., G. Zhan, T. Hance, S. Sugianto, S. Soulas, and E. Kjos, 2016, Valhall dual-well 3D DAS VSP field trial and imaging for active wells: 86th Annual International Meeting, SEG, Expanded Abstracts, 5582–5586.

Jreij, S., 2018, The feasibility of using distributed acoustic sensors in surface seismic application: Master's thesis, Colorado School of Mines.

Jreij, S., W. Trainor-Guitton, and D. Miller, 2017, Field data comparison of 3D horizontal distributed acoustic sensing and geophones: 87th Annual International Meeting, SEG, Expanded Abstracts, 1–6.

Karaman, O. S., R. L. Kutlik, E. L. Kluth, et al., 1996, A field trial to test fiber optic sensors for downhole temperature and pressure measurements, West Coalinga Field, California: Presented at the SPE Western Regional Meeting, Society of Petroleum Engineers.

Kawakatsu, H., and J.-P. Montagner, 2008, Time-reversal seismic-source imaging and moment-tensor inversion: Geophysical Journal International, **175**, 686–688.

Kim, Y., Q. Liu, and J. Tromp, 2011, Adjoint centroid-moment tensor inversions: Geophysical Journal International, **186**, 264–278.

Komatitsch, D., and J. Tromp, 2002a, Spectral-element simulations of global seismic wave propagationI. Validation: Geophysical Journal International, **149**, 390–412.

———, 2002b, Spectral-element simulations of global seismic wave propagationII. Three-dimensional models, oceans, rotation and self-gravitation: Geophysical Journal International, **150**, 303–318.

Komatitsch, D., and J.-P. Vilotte, 1998, The spectral element method: an efficient tool to simulate the seismic response of 2D and 3D geological structures: Bulletin of the seismological society of America, **88**, 368–392.

Kragh, E., E. Muyzert, J. Robertsson, D. Miller, and A. Hartog, 2014, Seismic acquisition system including a distributed sensor having an optical fiber: US Patent 8, 924, 158.

Kuvshinov, B., 2016, Interaction of helically wound fibre-optic cables with plane seismic waves: Geophysical Prospecting, **64**, 671–688.

Langston, C. A., 2007, Spatial gradient analysis for linear seismic arrays: Bulletin of the Seismological Society of America, **97**, 265–280.

Langston, C. A., P. Bodin, C. Powell, M. Withers, S. Horton, and W. Mooney, 2006, Explosion source strong ground motions in the Mississippi embayment: Bulletin of the Seismological Society of America, **96**, 1038–1054.

Lee, E.-J., P. Chen, T. H. Jordan, P. B. Maechling, M. A. Denolle, and G. C. Beroza, 2014, Full-3-D tomography for crustal structure in Southern California based on the scattering-integral and the adjoint-wavefield methods: Journal of Geophysical Research: Solid Earth, **119**, 6421–6451.

Li, L., I. Abakumov, H. Chen, X. Wang, D. Gajewski, et al., 2017, Comparison and generalization of correlation-based seismic source imaging methods: 87th Annual International Meeting, SEG, Expanded Abstracts, 2913–2917.

Li, Y., H. Wu, W. Wong, B. Hewett, Z. Liu, A. Mateeva, and J. Lopez, 2015, Velocity Analysis and Update with 3D DAS-VSP to Improve Borehole/Surface Seismic Images: 85th Annual International Meeting, SEG, Expanded Abstracts, 5285–5289.

Lim Chen Ning, I., and P. Sava, 2016, Multicomponent distributed acoustic sensing: 86th Annual International Meeting, SEG, Expanded Abstracts, 5597–5602.

———, 2017, High-resolution multicomponent distributed acoustic sensing: 87th Annual International Meeting, SEG, Expanded Abstracts, 941–946.

———, 2018a, High-resolution multi-component distributed acoustic sensing: Geophysical Prospecting, **66**, 1111–1122.

———, 2018b, Multicomponent distributed acoustic sensing: Concept and theory: Geophysics, **83**, P1–P8.

———, 2018c, Multicomponent imaging with distributed acoustic sensing: 88th Annual International Meeting, SEG, Expanded Abstracts, 4683–4687.

Lin, Y., and A. P. Pisano, 1988, The differential geometry of the general helix as applied to mechanical springs: Journal of Applied Mechanics, **55**, 831–836.

Lindsey, N. J., E. R. Martin, D. S. Dreger, B. Freifeld, S. Cole, S. R. James, B. L. Biondi, and J. B. Ajo-Franklin, 2017, Fiber-Optic Network Observations of Earthquake Wavefields: Geophysical Research Letters, **44**, 11–792.

Liu, S., X. Li, W. Wang, and T. Zhu, 2015, Source wavefield reconstruction using a linear combination of the boundary wavefield in reverse time migration: Geophysics, **80**, S203–S212.

Lumens, P., A. Franzen, K. Hornman, S. G. Karam, G. Hemink, B. Kuvshinov, J. La Follett, B. Wyker, and P. Zwartjes, 2013, Cable development for distributed geophysical sensing with a field trial in surface seismic: Fifth European Workshop on Optical Fibre Sensors, International Society for Optics and Photonics, 879435–879435.

Lumens, P. G. E., 2014, Fibre-optic sensing for application in oil and gas wells: PhD thesis, Technische Universiteit Eindhoven.

Madsen, K. N., M. Thompson, T. Parker, and D. Finfer, 2013, A VSP field trial using distributed acoustic sensing in a producing well in the north sea: First Break, **31**, 51–56.

Martin, G. S., R. Wiley, and K. J. Marfurt, 2006, Marmousi2: An elastic upgrade for marmousi: The Leading Edge, **25**, 156–166.

Masson, Y., P. Cupillard, Y. Capdeville, and B. Romanowicz, 2013, On the numerical implementation of time-reversal mirrors for tomographic imaging: Geophysical Journal International, **196**, 1580–1599.

Mateeva, A., J. Lopez, J. Mestayer, P. Wills, B. Cox, D. Kiyashchenko, Z. Yang, W. Berlang, R. Detomo, and S. Grandi, 2013, Distributed acoustic sensing for reservoir monitoring with VSP: The Leading Edge, **32**, 1278–1283.

Mateeva, A., J. Mestayer, B. Cox, D. Kiyashchenko, P. Wills, J. Lopez, S. Grandi, K. Hornman, P. Lumens, A. Franzen, et al., 2012, Advances in distributed acoustic sensing (DAS) for VSP: 82nd Annual International Meeting, SEG, Expanded Abstracts, 1–5.

Maxwell, S. C., J. Rutledge, R. Jones, and M. Fehler, 2010, Petroleum reservoir characterization using downhole microseismic monitoring: Geophysics, **75**, 75A129–75A137.

Mestayer, J., B. Cox, P. Wills, D. Kiyashchenko, J. Lopez, M. Costello, S. Bourne, G. Ugueto, R. Lupton, G. Solano, et al., 2011, Field trials of distributed acoustic sensing for geophysical monitoring: 81st Annual International Meeting, SEG, Expanded Abstracts, 4253–4257.

Moldoveanu, N., L. Combee, M. Egan, G. Hampson, L. Sydora, and W. Abriel, 2007, Over/under towed-streamer acquisition: A method to extend seismic bandwidth to both higher and lower frequencies: The Leading Edge, **26**, 41–58.

Montagner, J.-P., C. Larmat, Y. Capdeville, M. Fink, H. Phung, B. Romanowicz, E. Clévédé, and H. Kawakatsu, 2012, Time-reversal method and cross-correlation techniques by normal mode theory: a three-point problem: Geophysical Journal International, **191**, 637–652.

Moore, J. P., and M. D. Rogge, 2012, Shape sensing using multi-core fiber optic cable and parametric curve solutions: Optics express, **20**, 2967–2973.

Morse, P. M., and H. Feshbach, 1953, Methods of theoretical physics: McGraw-Hill.

Mulder, W., 2017, Higher-order source-wavefield reconstruction for reverse-time migration from stored values in a boundary strip just one point wide: Geophysics, **83**, 1–27.

Nakahara, H., and M. M. Haney, 2015, Point spread functions for earthquake source imaging: An interpretation based on seismic interferometry: Geophysical Journal International, **202**, 54–61.

Nguyen, B. D., and G. A. McMechan, 2014, Five ways to avoid storing source wavefield snapshots in 2D elastic prestack reverse time migration: Geophysics, **80**, S1–S18.

Özbek, A., M. Vassallo, K. Özdemir, D.-J. van Manen, and K. Eggenberger, 2010, Crossline wavefield reconstruction from multicomponent streamer data: Part 2joint interpolation and 3d up/down separation by generalized matching pursuit: Geophysics, **75**, WB69–WB85.

Raknes, E. B., and W. Weibull, 2016, Efficient 3D elastic full-waveform inversion using wavefield reconstruction methods: Geophysics, **81**, R45–R55.

Ravasi, M., and A. Curtis, 2013, Elastic imaging with exact wavefield extrapolation for application to ocean-bottom 4C seismic data: Geophysics, **78**, S265–S284.

Robertsson, J. O., and A. Curtis, 2002, Wavefield separation using densely deployed three-component single-sensor groups in land surface-seismic recordings: Geophysics, **67**, 1624–1633.

Robertsson, J. O., I. Moore, M. Vassallo, K. Özdemir, D.-J. van Manen, and A. Özbek, 2008, On the use of multicomponent streamer recordings for reconstruction of pressure wavefields in the crossline direction: Geophysics, **73**, A45–A49.

Robertsson, J. O., and E. Muyzert, 1999, Wavefield separation using a volume distribution of three component recordings: Geophysical Research Letters, **26**, 2821–2824.

Rocha, D., N. Tanushev, and P. Sava, 2017, Anisotropic elastic wavefield imaging using the energy norm: Geophysics, **82**, S225–S234.

Sadd, M. H., 2009, Elasticity: theory, applications, and numerics: Academic Press.

Schmelzbach, C., S. Donner, H. Igel, D. Sollberger, T. Taufiqurrahman, F. Bernauer, M. Häusler, C. Van Renterghem, J. Wassermann, and J. Robertsson, 2018, Advances in 6C seismology: Applications of combined translational and rotational motion measurements in global and exploration seismology: Geophysics, **83**, WC53–WC69.

Schmelzbach, C., D. Sollberger, C. Van Renterghem, M. Häusler, J. Robertsson, and S. Greenhalgh, 2016, Seismic spatial wavefield gradient and rotational rate measurements as new observables in land seismic exploration: EGU General Assembly Conference Abstracts, 3787.

Shen, X., and R. G. Clapp, 2011, Random boundary condition for low-frequency wave propagation: 81st Annual International Meeting, SEG, Expanded Abstracts, 2962–2965.

———, 2015, Random boundary condition for memory-efficient waveform inversion gradient computation: Geophysics, **80**, R351–R359.

Small, P., D. Gill, P. J. Maechling, R. Taborda, S. Callaghan, T. H. Jordan, K. B. Olsen, G. P. Ely, and C. Goulet, 2017, The SCEC unified community velocity model software framework: Seismological Research Letters, **88**, 1539–1552.

Soubaras, R., and R. Dowle, 2010, Variable-depth streamer–a broadband marine solution: first break, **28**.

Soubaras, R., and Y. Lafet, 2013, Variable-depth streamer acquisition: Broadband data for imaging and inversion: Geophysics, **78**, WA27–WA39.

Stewart, R. R., J. E. Gaiser, R. J. Brown, and D. C. Lawton, 2003, Converted-wave seismic exploration: Applications: Geophysics, **68**, 40–57.

Symes, W. W., 2007, Reverse time migration with optimal checkpointing: Geophysics, **72**, SM213–SM221.

Tan, S., and L. Huang, 2014, Reducing the computer memory requirement for 3D reverse-time migration with a boundary-wavefield extrapolation method: Geophysics, **79**, S185–S194.

Tromp, J., C. Tape, and Q. Liu, 2005, Seismic tomography, adjoint methods, time reversal and banana-doughnut kernels: Geophysical Journal International, **160**, 195–216.

Tsujikawa, K., K. Tajima, and J. Zhou, 2005, Intrinsic loss of optical fibers: Optical Fiber Technology, **11**, 319–331.

Uzunoglu, N. K., 1981, Scattering from inhomogeneities inside a fiber waveguide: JOSA, **71**, 259–273.

van Borselen, R. G., J. Fokkema, and P. van den Berg, 2013, Wavefield decomposition based on acoustic reciprocity: Theory and applications to marine acquisition: Geophysics, **78**, WA41–WA54.

Vasmel, M., and J. O. Robertsson, 2016, Exact wavefield reconstruction on finite-difference grids with minimal memory requirements: Geophysics, **81**, T303–T309.

Wapenaar, C. P. A., 2014, Elastic wave field extrapolation: Redatuming of single-and multi-component seismic data: Elsevier, **2**.

Wu, H., W. F. Wong, Z. Yang, P. Wills, J. Lopez, Y. Li, B. Blonk, B. Hewett, and A. Mateeva, 2015, Dual-well 3D vertical seismic profile enabled by distributed acoustic sensing in deepwater Gulf of Mexico: Interpretation, **3**, SW11–SW25.

Yan, J., 2010, Wave-mode separation for elastic imaging in transversely isotropic media: PhD thesis, Colorado School of Mines.

Yan, J., and P. Sava, 2012, Elastic wave mode separation for tilted transverse isotropic media: Geophysical Prospecting, **60**, 29–48.

Yang, P., R. Brossier, and J. Virieux, 2016, Wavefield reconstruction by interpolating significantly decimated boundaries: Geophysics, **81**, T197–T209.

Yang, P., J. Gao, and B. Wang, 2014, RTM using effective boundary saving: A staggered grid GPU implementation: Computers & Geosciences, **68**, 64–72.

Young, W. C., and R. G. Budynas, 2002, Roark's formulas for stress and strain: McGraw-Hill, **7**.

Zhan, G., J. Kommedal, and J. Nahm, 2015, VSP field trials of distributed acoustic sensing in Trinidad and Gulf of Mexico: 85th Annual International Meeting, SEG, Expanded Abstracts, 5539–5543.

APPENDIX

PERMISSIONS FOR CHAPTERS

This appendix details the permissions to reuse papers published with various publishers in the dissertation and the permission to include the results obtained using the Eagle Ford Shale dataset.

A.1 Permission from publisher

The snippet below retrieved from `https://seg.org/Publications/Policies-and-Permissions/Open-Access-Policy` grants the permission (highlighted in yellow) to reuse published papers with *Geophysics* to be in a thesis or dissertation.

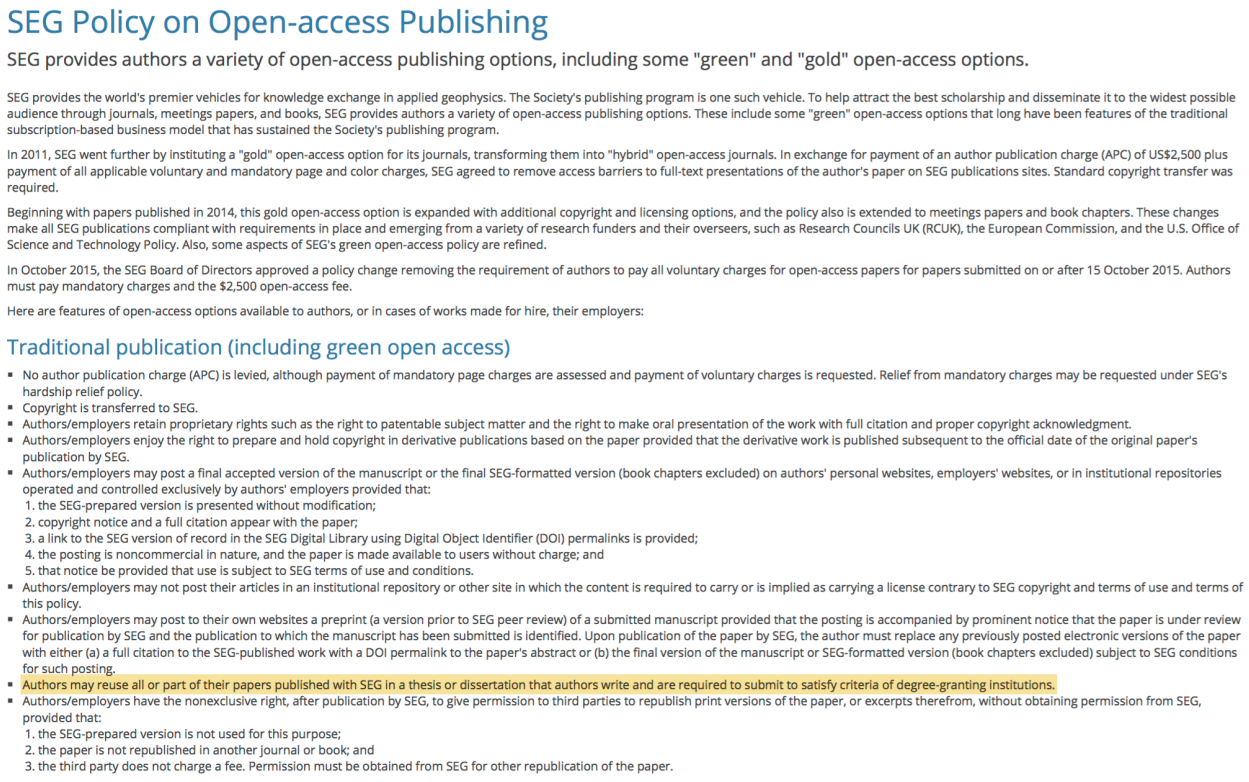

SEG Policy on Open-access Publishing

SEG provides authors a variety of open-access publishing options, including some "green" and "gold" open-access options.

SEG provides the world's premier vehicles for knowledge exchange in applied geophysics. The Society's publishing program is one such vehicle. To help attract the best scholarship and disseminate it to the widest possible audience through journals, meetings papers, and books, SEG provides authors a variety of open-access publishing options. These include some "green" open-access options that long have been features of the traditional subscription-based business model that has sustained the Society's publishing program.

In 2011, SEG went further by instituting a "gold" open-access option for its journals, transforming them into "hybrid" open-access journals. In exchange for payment of an author publication charge (APC) of US$2,500 plus payment of all applicable voluntary and mandatory page and color charges, SEG agreed to remove access barriers to full-text presentations of the author's paper on SEG publications sites. Standard copyright transfer was required.

Beginning with papers published in 2014, this gold open-access option is expanded with additional copyright and licensing options, and the policy also is extended to meetings papers and book chapters. These changes make all SEG publications compliant with requirements in place and emerging from a variety of research funders and their overseers, such as Research Councils UK (RCUK), the European Commission, and the U.S. Office of Science and Technology Policy. Also, some aspects of SEG's green open-access policy are refined.

In October 2015, the SEG Board of Directors approved a policy change removing the requirement of authors to pay all voluntary charges for open-access papers for papers submitted on or after 15 October 2015. Authors must pay mandatory charges and the $2,500 open-access fee.

Here are features of open-access options available to authors, or in cases of works made for hire, their employers:

Traditional publication (including green open access)

- No author publication charge (APC) is levied, although payment of mandatory page charges are assessed and payment of voluntary charges is requested. Relief from mandatory charges may be requested under SEG's hardship relief policy.
- Copyright is transferred to SEG.
- Authors/employers retain proprietary rights such as the right to patentable subject matter and the right to make oral presentation of the work with full citation and proper copyright acknowledgment.
- Authors/employers enjoy the right to prepare and hold copyright in derivative publications based on the paper provided that the derivative work is published subsequent to the official date of the original paper's publication by SEG.
- Authors/employers may post a final accepted version of the manuscript or the final SEG-formatted version (book chapters excluded) on authors' personal websites, employers' websites, or in institutional repositories operated and controlled exclusively by authors' employers provided that:
  1. the SEG-prepared version is presented without modification;
  2. copyright notice and a full citation appear with the paper;
  3. a link to the SEG version of record in the SEG Digital Library using Digital Object Identifier (DOI) permalinks is provided;
  4. the posting is noncommercial in nature, and the paper is made available to users without charge; and
  5. that notice be provided that use is subject to SEG terms of use and conditions.
- Authors/employers may not post their articles in an institutional repository or other site in which the content is required to carry or is implied as carrying a license contrary to SEG copyright and terms of use and terms of this policy.
- Authors/employers may post to their own websites a preprint (a version prior to SEG peer review) of a submitted manuscript provided that the posting is accompanied by prominent notice that the paper is under review for publication by SEG and the publication to which the manuscript has been submitted is identified. Upon publication of the paper by SEG, the author must replace any previously posted electronic versions of the paper with either (a) a full citation to the SEG-published work with a DOI permalink to the paper's abstract or (b) the final version of the manuscript or SEG-formatted version (book chapters excluded) subject to SEG conditions for such posting.
- Authors may reuse all or part of their papers published with SEG in a thesis or dissertation that authors write and are required to submit to satisfy criteria of degree-granting institutions.
- Authors/employers have the nonexclusive right, after publication by SEG, to give permission to third parties to republish print versions of the paper, or excerpts therefrom, without obtaining permission from SEG, provided that:
  1. the SEG-prepared version is not used for this purpose;
  2. the paper is not republished in another journal or book; and
  3. the third party does not charge a fee. Permission must be obtained from SEG for other republication of the paper.

Figure A.1: Permission from *Geophysics*.

JOHN WILEY AND SONS LICENSE TERMS AND CONDITIONS

Apr 01, 2019

This Agreement between Colorado School of Mines -- Ivan Lim Chen Ning ("You") and John Wiley and Sons ("John Wiley and Sons") consists of your license details and the terms and conditions provided by John Wiley and Sons and Copyright Clearance Center.

License Number	4560241263705
License date	Apr 01, 2019
Licensed Content Publisher	John Wiley and Sons
Licensed Content Publication	Geophysical Prospecting
Licensed Content Title	High-resolution multi-component distributed acoustic sensing
Licensed Content Author	Ivan Lim Chen Ning, Paul Sava
Licensed Content Date	May 29, 2018
Licensed Content Volume	66
Licensed Content Issue	6
Licensed Content Pages	12
Type of use	Dissertation/Thesis
Requestor type	Author of this Wiley article
Format	Print and electronic
Portion	Full article
Will you be translating?	No
Title of your thesis / dissertation	MULTICOMPONENT DISTRIBUTED ACOUSTIC SENSING: CONCEPT, THEORY, AND APPLICATIONS
Expected completion date	May 2019
Expected size (number of pages)	150
Requestor Location	Colorado School of Mines 1500 Illinois Street GOLDEN, CO 80401 United States Attn: Colorado School of Mines
Publisher Tax ID	EU826007151
Total	0.00 USD
Terms and Conditions	

TERMS AND CONDITIONS

This copyrighted material is owned by or exclusively licensed to John Wiley & Sons, Inc. or one of its group companies (each a"Wiley Company") or handled on behalf of a society with which a Wiley Company has exclusive publishing rights in relation to a particular work (collectively "WILEY"). By clicking "accept" in connection with completing this licensing transaction, you agree that the following terms and conditions apply to this transaction (along with the billing and payment terms and conditions established by the Copyright Clearance Center Inc., ("CCC's Billing and Payment terms and conditions"), at the time that you opened your RightsLink account (these are available at any time at http://myaccount.copyright.com).

Terms and Conditions

- The materials you have requested permission to reproduce or reuse (the "Wiley Materials") are protected by copyright.
- You are hereby granted a personal, non-exclusive, non-sub licensable (on a stand-alone basis), non-transferable, worldwide, limited license to reproduce the Wiley Materials for the purpose specified in the licensing process. This license, **and any CONTENT (PDF or image file) purchased as part of your order,** is for a one-time use only and limited to any maximum distribution number specified in the license. The first instance of republication or reuse granted by this license must be completed within two years of the date of the grant of this license (although copies prepared before the end date may be distributed thereafter). The Wiley Materials shall not be used in any other manner or for any other purpose, beyond what is granted in the license. Permission is granted subject to an appropriate acknowledgement given to the author, title of the material/book/journal and the publisher. You shall also duplicate the copyright notice that appears in the Wiley publication in your use of the Wiley Material. Permission is also granted on the understanding that nowhere in the text is a previously published source acknowledged for all or part of this Wiley Material. Any third party content is expressly excluded from this permission.
- With respect to the Wiley Materials, all rights are reserved. Except as expressly granted by the terms of the license, no part of the Wiley Materials may be copied, modified, adapted (except for minor reformatting required by the new Publication), translated, reproduced, transferred or distributed, in any form or by any means, and no derivative works may be made based on the Wiley Materials without the prior permission of the respective copyright owner.**For STM Signatory Publishers clearing permission under the terms of the STM Permissions Guidelines only, the terms of the license are extended to include subsequent editions and for editions in other languages, provided such editions are for the work as a whole in situ and does not involve the separate exploitation of the permitted figures or extracts,** You may not alter, remove or suppress in any manner any copyright, trademark or other notices displayed by the Wiley Materials. You may not license, rent, sell, loan, lease, pledge, offer as security, transfer or assign the Wiley Materials on a stand-alone basis, or any of the rights granted to you hereunder to any other person.
- The Wiley Materials and all of the intellectual property rights therein shall at all times remain the exclusive property of John Wiley & Sons Inc, the Wiley Companies, or their respective licensors, and your interest therein is only that of having possession of and the right to reproduce the Wiley Materials pursuant to Section 2 herein during the continuance of this Agreement. You agree that you own no right, title or interest in or to the Wiley Materials or any of the intellectual property rights therein. You shall have no rights hereunder other than the license as provided for above in Section 2. No right, license or interest to any trademark, trade name, service mark or other branding ("Marks") of WILEY or its licensors is granted hereunder, and you agree that you shall not assert any such right, license or interest with respect thereto
- NEITHER WILEY NOR ITS LICENSORS MAKES ANY WARRANTY OR REPRESENTATION OF ANY KIND TO YOU OR ANY THIRD PARTY, EXPRESS, IMPLIED OR STATUTORY, WITH RESPECT TO THE MATERIALS OR THE ACCURACY OF ANY INFORMATION CONTAINED IN THE MATERIALS, INCLUDING, WITHOUT LIMITATION, ANY IMPLIED WARRANTY OF MERCHANTABILITY, ACCURACY, SATISFACTORY QUALITY, FITNESS FOR A PARTICULAR PURPOSE, USABILITY, INTEGRATION OR NON-INFRINGEMENT AND ALL SUCH WARRANTIES ARE HEREBY EXCLUDED BY WILEY AND ITS LICENSORS AND WAIVED BY YOU.
- WILEY shall have the right to terminate this Agreement immediately upon breach of this Agreement by you.
- You shall indemnify, defend and hold harmless WILEY, its Licensors and their respective directors, officers, agents and employees, from and against any actual or threatened claims, demands, causes of action or proceedings arising from any breach of this Agreement by you.
- IN NO EVENT SHALL WILEY OR ITS LICENSORS BE LIABLE TO YOU OR ANY OTHER PARTY OR ANY OTHER PERSON OR ENTITY FOR ANY SPECIAL, CONSEQUENTIAL, INCIDENTAL, INDIRECT, EXEMPLARY OR PUNITIVE DAMAGES, HOWEVER CAUSED, ARISING OUT OF OR IN CONNECTION WITH THE DOWNLOADING, PROVISIONING, VIEWING OR USE OF THE MATERIALS REGARDLESS OF THE FORM OF ACTION, WHETHER FOR BREACH OF CONTRACT, BREACH OF WARRANTY, TORT, NEGLIGENCE, INFRINGEMENT OR OTHERWISE (INCLUDING, WITHOUT LIMITATION, DAMAGES BASED ON LOSS OF PROFITS, DATA, FILES, USE, BUSINESS OPPORTUNITY OR CLAIMS OF THIRD PARTIES), AND WHETHER OR NOT THE PARTY HAS BEEN ADVISED OF THE POSSIBILITY OF SUCH DAMAGES. THIS LIMITATION SHALL APPLY NOTWITHSTANDING ANY FAILURE OF ESSENTIAL PURPOSE OF ANY LIMITED REMEDY PROVIDED HEREIN.
- Should any provision of this Agreement be held by a court of competent jurisdiction to be illegal, invalid, or unenforceable, that provision shall be deemed amended to achieve as nearly as possible the same economic effect as the original provision, and the legality, validity and enforceability of the remaining provisions of this Agreement shall not be affected or impaired thereby.
- The failure of either party to enforce any term or condition of this Agreement shall not constitute a waiver of either party's right to enforce each and every term and condition of this Agreement. No breach under this agreement shall be deemed waived or excused by either party unless such waiver or consent is in writing signed by the party granting such waiver or consent. The waiver by or consent of a party to a breach of any provision of this Agreement shall not operate or be construed as a waiver of or consent to any other or subsequent breach by such other party.
- This Agreement may not be assigned (including by operation of law or otherwise) by you without WILEY's prior written consent.
- Any fee required for this permission shall be non-refundable after thirty (30) days from receipt by the CCC.
- These terms and conditions together with CCC's Billing and Payment terms and conditions (which are incorporated herein) form the entire agreement between you and WILEY concerning this licensing transaction and (in the absence of fraud) supersedes all prior agreements and representations of the parties, oral or written. This Agreement may not be amended except in writing signed by both parties. This Agreement shall be binding upon and inure to the benefit of the parties' successors, legal representatives, and authorized assigns.
- In the event of any conflict between your obligations established by these terms and conditions and those established by CCC's Billing and Payment terms and conditions, these terms and conditions shall prevail.
- WILEY expressly reserves all rights not specifically granted in the combination of (i) the license details provided by you and accepted in the course of this licensing transaction, (ii) these terms and conditions and (iii) CCC's Billing and Payment terms and conditions.
- This Agreement will be void if the Type of Use, Format, Circulation, or Requestor Type was misrepresented during the licensing process.
- This Agreement shall be governed by and construed in accordance with the laws of the State of New York, USA, without regards to such state's conflict of law rules. Any legal action, suit or proceeding arising out of or relating to these Terms and Conditions or the breach thereof shall be instituted in a court of competent jurisdiction in New York County in the State of New York in the United States of America and each party hereby consents and submits to the personal jurisdiction of such court, waives any objection to venue in such court and consents to service of process by registered or certified mail, return receipt requested, at the last known address of such party.

WILEY OPEN ACCESS TERMS AND CONDITIONS

Wiley Publishes Open Access Articles in fully Open Access Journals and in Subscription journals offering Online Open. Although most of the fully Open Access journals publish open access articles under the terms of the Creative Commons Attribution (CC BY) License only, the subscription journals and a few of the Open Access Journals offer a choice of Creative Commons Licenses. The license type is clearly identified on the article.

The Creative Commons Attribution License

The Creative Commons Attribution License (CC-BY) allows users to copy, distribute and transmit an article, adapt the article and make commercial use of the article. The CC-BY license permits commercial and non-

Creative Commons Attribution Non-Commercial License

The Creative Commons Attribution Non-Commercial (CC-BY-NC)License permits use, distribution and reproduction in any medium, provided the original work is properly cited and is not used for commercial purposes.(see below)

Creative Commons Attribution-Non-Commercial-NoDerivs License

The Creative Commons Attribution Non-Commercial-NoDerivs License (CC-BY-NC-ND) permits use, distribution and reproduction in any medium, provided the original work is properly cited, is not used for commercial purposes and no modifications or adaptations are made. (see below)

Use by commercial "for-profit" organizations

Use of Wiley Open Access articles for commercial, promotional, or marketing purposes requires further explicit permission from Wiley and will be subject to a fee.
Further details can be found on Wiley Online Library
http://olabout.wiley.com/WileyCDA/Section/id-410895.html

Other Terms and Conditions:

v1.10 Last updated September 2015

Questions? customercare@copyright.com or +1-855-239-3415 (toll free in the US) or +1-978-646-2777.

Figure A.2: Permission from John Wiley and Sons, publisher for *Geophysical Prospecting*.

A.2 Permission for field datasets

In this appendix, I include a copy of the emails exchanged with company representatives who grant permission to include the field datasets for publication in the dissertation. The Eagle Ford Shale dataset in Chapter 5 is from Devon Energy Corporation.

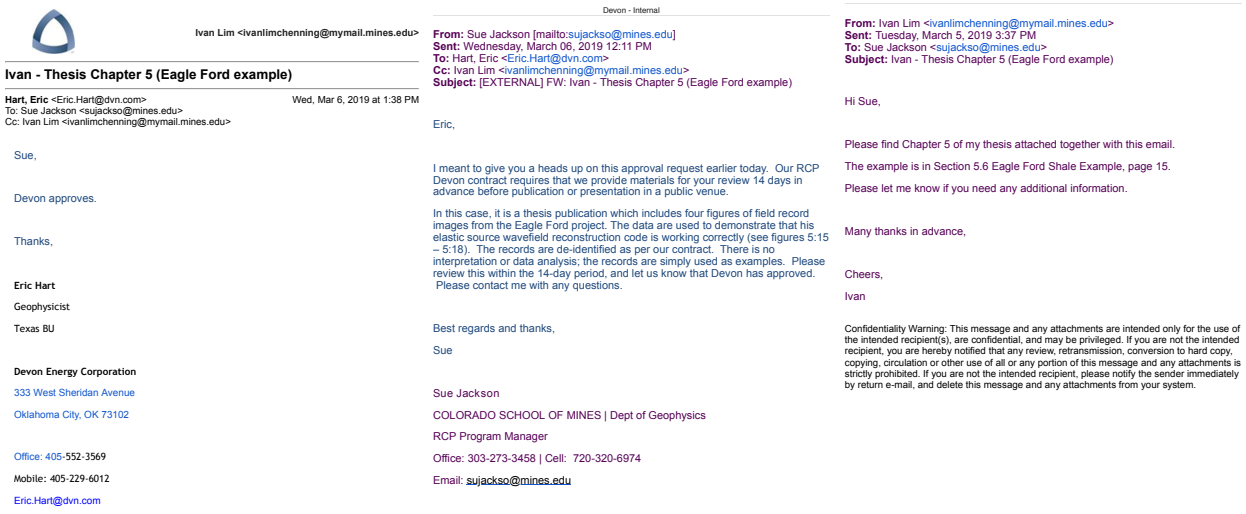

Ivan Lim <ivanlimchenning@mymail.mines.edu>

Ivan - Thesis Chapter 5 (Eagle Ford example)

Hart, Eric <Eric.Hart@dvn.com> Wed, Mar 6, 2019 at 1:38 PM
To: Sue Jackson <sujackso@mines.edu>
Cc: Ivan Lim <ivanlimchenning@mymail.mines.edu>

Sue,

Devon approves.

Thanks,

Eric Hart
Geophysicist
Texas BU

Devon Energy Corporation
333 West Sheridan Avenue
Oklahoma City, OK 73102

Office: 405-552-3569
Mobile: 405-229-6012
Eric.Hart@dvn.com

Devon - Internal

From: Sue Jackson [mailto:sujackso@mines.edu]
Sent: Wednesday, March 06, 2019 12:11 PM
To: Hart, Eric <Eric.Hart@dvn.com>
Cc: Ivan Lim <ivanlimchenning@mymail.mines.edu>
Subject: [EXTERNAL] FW: Ivan - Thesis Chapter 5 (Eagle Ford example)

Eric,

I meant to give you a heads up on this approval request earlier today. Our RCP Devon contract requires that we provide materials for your review 14 days in advance before publication or presentation in a public venue.

In this case, it is a thesis publication which includes four figures of field record images from the Eagle Ford project. The data are used to demonstrate that his elastic source wavefield reconstruction code is working correctly (see figures 5:15 – 5:18). The records are de-identified as per our contract. There is no interpretation or data analysis; the records are simply used as examples. Please review this within the 14-day period, and let us know that Devon has approved. Please contact me with any questions.

Best regards and thanks,

Sue

Sue Jackson
COLORADO SCHOOL OF MINES | Dept of Geophysics
RCP Program Manager
Office: 303-273-3458 | Cell: 720-320-6974
Email: sujackso@mines.edu

From: Ivan Lim <ivanlimchenning@mymail.mines.edu>
Sent: Tuesday, March 5, 2019 3:37 PM
To: Sue Jackson <sujackso@mines.edu>
Subject: Ivan - Thesis Chapter 5 (Eagle Ford example)

Hi Sue,

Please find Chapter 5 of my thesis attached together with this email.

The example is in Section 5.6 Eagle Ford Shale Example, page 15.

Please let me know if you need any additional information.

Many thanks in advance,

Cheers,

Ivan

Confidentiality Warning: This message and any attachments are intended only for the use of the intended recipient(s), are confidential, and may be privileged. If you are not the intended recipient, you are hereby notified that any review, retransmission, conversion to hard copy, copying, circulation or other use of all or any portion of this message and any attachments is strictly prohibited. If you are not the intended recipient, please notify the sender immediately by return e-mail, and delete this message and any attachments from your system.

Figure A.3: Permission from Devon Energy Corporation.